Southampton Oceanography Centre
UNIVERSITY OF SOUTHAMPTON AND
NATURAL ENVIRONMENT RESEARCH COUNCIL

University
of Southampton

INTERANNUAL-TO-SEASONAL VARIABILITY OF THE SUBPOLAR NORTH ATLANTIC OCEAN

PHD DISSERTATION

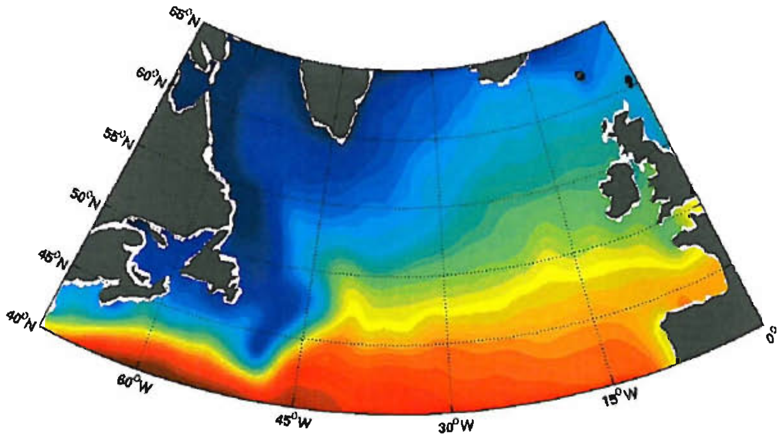

submitted by

James Harle

to the Graduate School of the Southampton Oceanography Centre in partial fulfillment of
the requirements for the degree of Doctor of Philosophy

January 2005

Southampton
Oceanography Centre
UNIVERSITY OF SOUTHAMPTON AND
NATURAL ENVIRONMENT RESEARCH COUNCIL

Graduate School of the Southampton Oceanography Centre

This PhD dissertation by

James Harle

has been produced under the supervision of the following persons

Supervisors

Prof. Raymond Pollard

Chair of Advisory Panel

Dr. Jon Bull

Members of Advisory Panel

Prof. Kelvin J. Richards and Prof. Jochem Marotzke

University of Southampton

Abstract

Faculty of Engineering, Science and Mathematics
School of Ocean & Earth Sciences

Doctor of Philosophy

INTERANNUAL-TO-SEASONAL VARIABILITY OF THE SUBPOLAR NORTH ATLANTIC OCEAN

by James Harle

In this thesis we examine the seasonal to interannual variability of the Subpolar North Atlantic Ocean over the last decade using both observations and models. The Topex/Poseidon altimeter is the primary source for the observational data, which are analysed to examine the seasonal-to-interannual surface variability of the Subpolar North Atlantic Ocean. These data are also used to infer changes in the positions of the Subpolar Front and the large-scale circulation. Model output is provided from the *Estimating the Circulation and Climate of the Ocean* model (ECCO) and has been examined, firstly, to establish the realism of the model in the light of the altimeter data and historical observations. Then, secondly, to identify any further variability in the ocean system and to document associated forcing mechanisms. The tools used to identify principal modes of variability and any coupling within the climate system are those stemming from Empirical Orthogonal Function analysis.

The analysis of the Topex/Poseidon data reveals that surface variability in the Subpolar Gyre region is primarily driven by the wind field, whereas in the Newfoundland Basin this is not the case. The study also confirmed previous hydrographic analysis that there had been significant shifts in the position of the Subpolar Front in the Iceland Basin over the last decade. Analysis of the position of the Subpolar Front in ECCO reveals much the same picture as in the altimeter data. It is demonstrated that the frontal shifts are as a result of a Sverdrup-like response of the ocean to variable wind forcing, of which the North Atlantic Oscillation (NAO) is one of the dominant modes. It is also thought that this mechanism could be responsible for the generation and subsequent eastward propagation of temperature anomalies along the pathway of the Subpolar Front.

Another common feature present in both the altimeter data and output from ECCO is the weakening of the North Atlantic Current (NAC) and more generally the Subpolar Gyre over the last decade. The decrease primarily occurs in the Labrador Sea region and appears to be linked to the low-frequency fluctuations in the baroclinic structure of the water column. Over the period of the altimeter observations and the model run the NAC decrease in strength by ~16% and ~20% respectively.

High frequency fluctuations in the Meridional Overturning Circulation (MOC) in the Subpolar North Atlantic are dominated by an Ekman response to the wind forcing and remain a significant contributor to the variability on interannual time-scales, exhibiting a significant correlation to the NAO. Two principal modes of variability are identified in the MOCs response to fluctuations in the wind forcing; An NAO and East Atlantic Oscillation-like pattern are found to be associated with an Ekman overturning cell and anomalous Ekman pumping respectively. There is also evidence of longer-term variations in the strength of the overturning, but the length of the model run is insufficient to quantify the characteristics of this.

Acknowledgements

First and foremost I would like to thank Raymond Pollard for accepting the challenge. Being blessed with the self confidence and English skills of a dormouse, I must have presented a challenge that may have seemed insurmountable at times. However, I only ever received encouragement from Raymond, for which I am truly grateful!

I am indebted to Joel Hirschi for the many useful and encouraging discussions concerning my work. Even though Joel had a full compliment of PhD students to supervise, in addition to undertaking his own research, he still managed, somehow, to find time for me. Thank you.

I must also thank Peter Challenor, Peter Killworth and Bablu Sinha for allowing me to fire numerous *trivial* questions at them. Never once appearing annoyed or disinterested; their doors were always open, a fact that I am very thankful for.

My thanks too must go to Professor Detlef Stammer for supervising me during a three month visit to Scripps Institution of Oceanography. Detlef's enthusiasm for oceanography coupled with the wealth of knowledge he possesses enthused and motivated me throughout my final year of study.

To my Parents, Brother, office mates, Oli, Cesar, and Deb and to my friends at SOC, especially Alice, Sinhué and Ana: thank you for keeping me sane and allowing me to smile from time to time. Backgammon is, indeed, a wonderful game!

Finally, my thanks and love to Amélie, with whom I have had fortune to share this most auspicious period of my life. For without her care and cajolement I would have absconded long ago.

Contents

List of Figures **vii**

List of Tables **xi**

1 Introduction **1**

2 The Subpolar North Atlantic **5**

2.1 Introduction 5

2.2 Bathymetry 6

2.3 Ocean Circulation 7

2.4 Interannual to seasonal ocean variability 15

2.5 Atmospheric variability 20

2.6 Summary 24

3 Surface eddy kinetic energy measurements of the Subpolar Gyre **27**

3.1 Introduction 27

3.2 Altimeter Data 29

3.3 Deriving eddy kinetic energy 30

3.4 Results 32

3.4.1 Interannual variability 34

3.4.2 Seasonal variability 45

3.5 Discussion of results 48

3.6 Summary 51

4 Variability as seen in two ocean general circulation models **54**

4.1 Introduction 54

4.2 The Models 55

4.2.1 The Ocean Circulation and Climate Advanced Model 55

4.2.2 ECCO model 56

4.3 Aspects of the horizontal circulation 58

4.3.1 Sea surface elevation 58

4.3.2 Changes in steric height 62

4.3.3 Horizontal transport 64
4.4 Mixed layer depths 65
4.5 Comparison with hydrography 67
4.5.1 Introduction 67
4.5.2 Data 68
4.5.3 Water mass distribution 69
4.5.4 Summary 73
4.6 Discussion of results 74
4.7 Summary 75

5 Variability of the horizontal circulation 78
5.1 Introduction 78
5.2 Frontal variability 79
5.3 Changes in the large-scale horizontal circulation 83
5.4 Lagrangian analysis 94
5.5 Propagating Features 98
5.6 Discussion of results 109
5.7 Summary 112

6 Meridional Overturning Circulation Variability 115
6.1 Introduction 115
6.2 Meridional Overturning Circulation 117
6.3 Components of the MOC 120
6.4 Maximum Covariance Analysis of the MOC 126
6.5 Vertical Advection 131
6.6 Discussion of results 135
6.7 Summary 138

7 Summary and Conclusions 141

A On the use of splines 148

B Empirical Orthogonal Functions (EOFs) 151
B.1 EOF Analysis 151
B.1.1 A Note of Caution 153
B.2 CEOF Analysis 154
B.3 Maximum Covariance Analysis 155

List of Figures

1.1 The Subpolar North Atlantic Ocean; the focal region of this study. 2

2.1 Bathymetry of the Subpolar North Atlantic 7
2.2 Pathway of the North Atlantic Current through the Newfoundland Basin. . 9
2.3 Distribution of floats passing over the Mid Atlantic Ridge. 11
2.4 The trajectory of a RAFOS profiling float in the Labrador Basin. 13
2.5 Float derived streamfunction of the Labrador and Irminger Basins. 14
2.6 The first Empirical Orthogonal Function and associated Principal Component of the Gulf Stream pathway. 16
2.7 Westward shift in the Subpolar Front in the Iceland Basin between the years 1996 and 1995. 18
2.8 Sea surface height difference between years 1996 and 1995 in the western Subpolar North Atlantic Ocean from the Topex/Poseidon satellite altimeter. 20
2.9 Mean zonal wind stress at 55°N in the Subpolar North Atlantic between 1992 and 2002. 21
2.10 The mean wind stress curl over the Subpolar North Atlantic Ocean for the period 1992-2001. Units are in Nm^{-3}. 22
2.11 The leading mode of and Empirical Orthogonal Function analysis of the sea surface height data from the Topex/Poseidon altimeter. 24

3.1 Schematic of ascending and descending satellite passes at a crossover location 32
3.2 Map of mean eddy kinetic energy (m^2s^{-2}) computed for the period 1992 to 2001. 33
3.3 Time evolution of the mean eddy kinetic energy of the Subpolar North Atlantic Ocean and winter-time NAO-index. 35
3.4 Seven regions of the Subpolar North Atlantic Ocean used to analyse the temporal evolution in eddy kinetic energy. 36
3.5 Winter-time wind stress curl maps for the period 1992-2001. 37
3.6 Time-series of the mean eddy kinetic energy and wind stress for the seven regions of the Subpolar North Atlantic Ocean illustrated in Figure 3.4. . . . 40

3.7 Annual means of eddy kinetic energy along a satellite pass through the Newfoundland Basin and the *Northwest* Corner of the NAC. 41
3.8 A series of snap-shots of monthly mean eddy kinetic energy along a satellite pass through the Newfoundland Basin and the *Northwest* Corner of the NAC. 42
3.9 Annual means of eddy kinetic energy along a satellite pass along the Mid Atlantic Ridge. 43
3.10 Normalised eddy kinetic energy time-series along 55°N in the Iceland Basin. 44
3.11 The seasonal eddy kinetic energy anomaly, expressed as a percentage of the zonally averaged annual mean eddy kinetic energy. 46
3.12 Map of mean eddy kinetic energy (m^2s^{-2}) computed for each of the four seasons (1992-2001). 47
3.13 Eddy kinetic energy profiles during August 1997 along **a**) satellite *pass a* and **b**) satellite *pass b*. 49

4.1 B-Grid configuration used in the OCCAM. 55
4.2 C-Grid configuration used in the ECCO model. 57
4.3 Sea surface height comparison between OCCAM and ECCO. 58
4.4 Evolution of sea surface height anomaly of the Subpolar Gyre region (50°N to 65°N) for **a** ECCO and **b** OCCAM. 59
4.5 Changes in heat content in the Subpolar North Atlantic Ocean. 61
4.6 Changes in sea surface height through the upper steric height component, the lower steric height component and barotropic fluctuations. 63
4.7 OCCAM horizontal streamfunction 64
4.8 ECCO model horizontal streamfunction 65
4.9 Spatial map of the mean winter-time mixed layer depths in OCCAM and a time-series of the mixed layer depth in the Labrador Sea. 66
4.10 Spatial map of the winter-time mixed layer depths in ECCO and a time-series of the mixed layer depth in the Labrador Sea. 67
4.11 WOCE AR7E repeat hydrographic line (grey) and one-time FISHES hydrographic section (black). 68
4.12 Salinity profiles along the 1997 WOCE AR7E hydrographic line for the **a** OCCAM, **b** ECCO model and **c** hydrographic data. 69
4.13 Density differences between hydrographic and model data for the various WOCE AR7E hydrographic surveys undertaken in the 1990s. 70
4.14 Density differences between hydrographic and model data for the various WOCE AR7E hydrographic surveys undertaken in the 1990s. 71
4.15 Temperature-salinity diagrams illustrating the temporal changes between 1994 and 1997 72
4.16 Density difference between the FISHES hydrographic data and output from the ECCO model. 73

5.1 Interannual variability in the pathway of the North Atlantic Current in the Newfoundland Basin 80
5.2 An EOF analysis of depth integrated speed (0-610 m) in the Newfoundland Basin 81
5.3 Shifts in the position of the Subpolar Front. 82
5.4 Annual means of the depth integrated streamfunction of the Subpolar North Atlantic 84
5.5 Spatial maps and Principal Components (PC) for the leading mode of a MCA between the curl in the wind stress and *a)* the barotropic streamfunction and *b)* the Sverdrup transport. 86
5.6 Heat transport anomaly (PW) at 45.5°N **a)** west of the MAR and **b)** east of the MAR 87
5.7 Difference in steric height between 1992 and 2001, the beginning and end of the model run. 89
5.8 Steric height change from 1992 to 2001 (referenced to 2200 m) and the absolute sea surface height change from 1992 to 2001 across the Labrador Basin. 90
5.9 Heat energy balance in the Labrador region signified by the rectangular box in Figure 5.7. 91
5.10 Time evolution of the absolute sea surface height anomaly, steric height anomaly, thermal component of the steric height anomaly and haline component of the steric height anomaly in the central Labrador Sea. 92
5.11 Time evolution of the thermal component, heat flux component and heat transport component of the sea surface height anomaly in the central Labrador Sea. 92
5.12 The difference in heat transport between 1995 and 1996 (Wm^{-2}) along each side of the box in the Labrador region defined in Figure 5.7. 93
5.13 Results from lagrangian particle tracking experiments in the Subpolar Region in 1993 and 1998 95
5.14 Quantitative lagrangian particle tracking in the Subpolar Region 96
5.15 A series of Hovmöller diagrams illustrating the propagation of temperature anomalies at various depths in the upper ocean along 49.5°N 101
5.16 A series of snap-shots of the propagation of a negative temperature anomaly along the boundary between the Subpolar and the Subtropical Gyre at 222.5 m. 102
5.17 As Figure 5.15, but all data have been low-pass filter removing frequencies greater than 0.4 yr^{-1}. 103
5.18 Lagged correlation - longitude diagrams at 49.5°N between surface temperature anomalies and temperature anomalies at 222.5 m and at 610 m. . . . 104

5.19 The first mode of a CEOF analysis of the depth integrated temperature over the top 610 *m* of the water column. 105
5.20 Propagation of frontal characteristics 106

6.1 Merdional Overturning streamfunction for the North Atlantic. Time evolution of the overturning at 50°N and latitude at which the maximum overturning occurs 118
6.2 Annual cycle of the monthly mean meridional overturning transport anomalies above 1160 *m* for 25°N and 50°N. 119
6.3 Annual mean overturning streamfunction for the barotropic or *external* mode.121
6.4 Spatial maps and Principal Components (PC) for the first two modes of the EOF analysis of the barotropic component of the MOC. 122
6.5 The annual mean baroclinic component to the overturning streamfunction. 123
6.6 Spatial maps and Principal Components (PC) for the first two modes of the EOF analysis of the baroclinic component of the MOC. 124
6.7 Ekman component to the overturning in the Subpolar North Atlantic calculated from the mean zonal wind stress over the entire model run. 125
6.8 Meridional overturning streamfunction displayed in potential density space relative to 1000 *m*. 126
6.9 Spatial maps and Principal Components (PC) for the four leading modes of a MCA between the curl in the wind stress and overturning streamfunction. 129
6.10 Advection at the base of the thermocline (as described by $\sigma_1 = 32.3kgm^{-3}$). 132
6.11 Time series of the net transport across the thermocline as described by $\sigma_1 = 32.3$ kgm^{-3} in the intergyre zone (70°W to 0°W, 40°N to 50°N. 133
6.12 Vertical advection across the thermocline and equivalent transport due to Ekman pumping, off the Grand Banks of Newfoundland (55°W to 40°W, 40°N to 50°N). 134
6.13 Vertical advection across the thermocline (black line) and transport in the **a)** Deep Western Boundary Current and **b)** North Atlantic Current (grey line) at 45°N. 135

A.1 Residual sea surface height for cycle 300, pass 146, with a 30 *km* knotted spline fitted. 149
A.2 Power spectral density plot of the raw and splined sea surface height data from cycle 300, pass 146. 149

B.1 The first mode of a CEOF analysis of a northeastward propagating anomaly; a synthetic example. 155

List of Tables

3.1 Correlation between eddy kinetic energy and both the winter-time NAO-index and monthly wind stress magintude ($|\tau|$; seasonal cycle removed) for seven regions of the Subpolar North Atlantic Ocean. 38
3.2 Amplitude and phase of the annual harmonic of eddy kinetic energy in each of the seven regions. 45

4.1 List of tracer point depths and tracer box thickness for the OCCAM. 56
4.2 List of tracer point depths and tracer box thickness' for ECCO. 57

5.1 Exports from the Labrador Sea 97

Chapter 1

Introduction

[1] Our ability to observe, and hence understand, the climate system has greatly improved with advances in technology. The recent advent of satellite remote sensing platforms and General Circulation Models (GCM) of varying complexity have complimented the more traditional technique of in-situ sampling. Pushed by socio-economic factors in an increasingly aware society, understanding the variability, controlling mechanisms and possible prediction of the climate system has become a major concern of governments and scientists alike.

[2] Significant advances in our understanding of the oceans were made during the World Ocean Circulation Experiment (WOCE; 1990-2002), a principal project of the *World Climate Research Programme*. The overall objective of WOCE was to provide a quantitative description of the circulation of the World Ocean. This was fundamental to the foreseeable development of GCMs that would be useful for predicting climate change.

[3] In determining the long-term behaviour of the ocean, WOCE implemented a series of programmes that sampled the temporal variability in the system. The inherent problem of infrequent asynoptic sampling of a dynamic ocean using traditional observing techniques was partially overcome by the recent advances in technology; Satellite remote sensing strategies were providing accurate and reliable quasi-synoptic data, with a global repeat coverage of as little as 10 days, by the early 1990s and formed an integral part in monitoring the ocean, albeit only at the surface.

[4] As we are currently unable to provide a spatially or temporally synoptic view of the

World Ocean from observations alone, the modelling fraternity have recently developed *assimilation* techniques to overcome this shortfall in quality data. Through the synthesis of observational data with ocean GCMs, one can provide an ocean state estimation quantitatively more accurate than available from observations or models alone (Lu and Stammer, 2004). However, whether analysing results from constrained or unconstrained model simulations, one must remember that solutions are only an approximation of the system being simulated. As numerical and computational constraints force the exclusion of physical processes and the parameterisation of others that are unable to be resolved, it is imperative that a validation is undertaken prior to any analysis.

[5] In the present study, we will seek to identify changes in the large-scale circulation of the Subpolar North Atlantic Ocean (Figure 1.1) through the analysis of such satellite and ocean GCM data. Emphasis is placed on shifts in the large-scale frontal systems and changes in both the basin-scale horizontal and meridional overturning circulation.

[6] The circulation of the Atlantic Ocean differs from the other oceanic basins. Warm waters are transported northward via a series of strong surface currents before being cooled in the Subpolar North Atlantic and Arctic Oceans and return southward at depth. The circulation of the North Atlantic Ocean has been extensively surveyed over the last century in order to gain an understanding of the large northward transport of heat that is thought to influence, in part, the climate over northern europe. More recently, there have been concerns that changes in the circulation of the North Atlantic could not only affect local climate, but also have possible global implications.

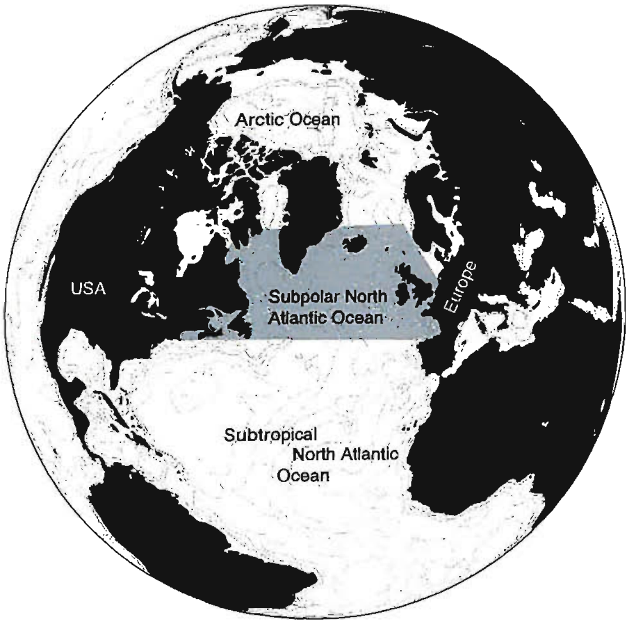

Figure 1.1: The Subpolar North Atlantic Ocean; the focal region of this study.

[7] Thermodynamic exchange between the Subtropical and Subpolar North Atlantic Ocean is an integral part of the overturning in the North Atlantic. The

North Atlantic Current forms the dynamically active boundary between these two regions and plays an important role in cross frontal exchange of water mass properties. Thus, variations in the North Atlantic Current will have an impact on the global ocean system and the climate of northern Europe. It is therefore necessary to identify changes in the circulation of the Subpolar North Atlantic Ocean and attempt to quantify the physical processes involved if we are to improve our understanding of the climate system.

[8] Throughout this study particular reference will be paid to the North Atlantic Oscillation (NAO; Hurrell (1995)), as this is one of the most robust recurrent patterns of atmospheric variability in the mid-to-high latitudes of the Northern Hemisphere. Such a pattern will induce significant changes in the climate of the ocean via fluctuations in wind and buoyancy forcing. This atmospheric phenomenon is often cited as the main cause for changes in circulation and redistribution of water masses in the region (e.g. Bersch, 2002).

[9] The thesis is structured in the following manner: Chapter 2 provides a summary of the circulation of the Subpolar North Atlantic Ocean and a brief overview of the variability previously observed in this region. In Chapter 3 data from a satellite altimeter will be used to describe the surface variability in the Subpolar North Atlantic Ocean and provide inferences on any changes in the large-scale circulation. A comparison between two Ocean General Circulation Models is presented in Chapter 4, along with their validation against observational data. The analyses in Chapters 5 and 6 will focus on the changes in the horizontal and meridional circulation in one of these Ocean General Circulation Models. Finally a summary of the study and concluding remarks are presented.

Chapter 2

The Subpolar North Atlantic

2.1 Introduction

[1] The Subpolar North Atlantic Ocean is one of only a few regions where deep convection occurs. Preconditioning of an enclosed body of water coupled with strong air-sea buoyancy fluxes are the prerequisites to the deep convection that drives the ocean overturning circulation. It is therefore important to understand the dynamics and variability of the upper Subpolar North Atlantic Ocean that may significantly influence this process. Variations in the overturning in the Subpolar North Atlantic (also to the north in the Greenland Sea) may have implications for climate over northern Europe[1] as warmer waters are transported between Subtropical and Subpolar regions as part of the overturning circulation.

[2] The advent of new sensing techniques along with the global scientific collaboration of the World Ocean Circulation Experiment (WOCE) over the last decade has greatly advanced monitoring of the world's oceans. With this improved knowledge of the ocean's state and the development of super computers the discipline of implementing global Ocean General Circulation Models has rapidly expanded providing a useful tool for diagnosis of various oceanic processes.

[3] Historically, in part due to the infrequency of measurements and a lack of understanding of the circulation, variability of the ocean has been measured on the longer time-scales of order of decades. Recently, with more advanced observational platforms, e.g. satellite

---

[1] Although the relatively mild climate over northern Europe is predominantly influenced by the seasonal heat storage of the oceans and the atmospheric circulation (Seager *et al.*, 2002)

platforms and profiling floats, it has been realised just how variable the ocean is. Significant changes have been observed over relatively short time-scales of the order of years and are potentially comparable in magnitude to longer time-scale events (e.g. Reverdin *et al.*, 1999).

[4] If we are to make future predictions about changes in the climate system we have to improve our understanding of the processes influencing ocean circulation. The recent circulation pathways of the Subpolar North Atlantic Ocean are reasonably well known through; hydrographic surveys (e.g. Pollard, 1996), drifter observations (e.g. Lavender *et al.*, 2000) and satellite data (e.g. Heywood *et al.*, 1994), but the mechanisms for the dynamical variations in the circulation are poorly understood. Changes in the circulation have been associated with the ocean's response to external fluctuations in atmospheric forcing (Stammer and Wunsch, 1999), fresh water fluxes and interactions with topography (Reverdin *et al.*, 1999). These changes can also depend on internal forcing, e.g. buoyancy forcing, dynamic instabilities (Stammer and Wunsch, 1999) and circulation pathway-pathway interaction (Thompson and Schmitz, 1989). Using data output from Ocean General Circulation Models (OGCM) an understanding of the processes and forcing mechanisms present in the ocean system can be determined. These would also provide valuable information for future hydrographic and drifter surveys.

[5] After an introduction to the bathymetry in the following section this chapter will provide a summary of the circulation of the Subpolar North Atlantic Ocean (Section 2.3) with a brief overview of the variability observed in this region (Section 2.4). Section 2.5 introduces modes of variability in the atmosphere that play an important role in determining the state of the ocean and to conclude a summary of the aims of the thesis is presented (Section 2.6).

2.2 Bathymetry

[6] The bathymetry of the Subpolar North Atlantic is depicted in Figure 2.1. Consisting of four basins; Labrador, Newfoundland, Iceland and Irminger Basins, the Subpolar North Atlantic is topographically bounded on three sides. A submarine ridge system to the north, between Greenland and Scotland, isolates the intermediate and deep Nordic Seas from the

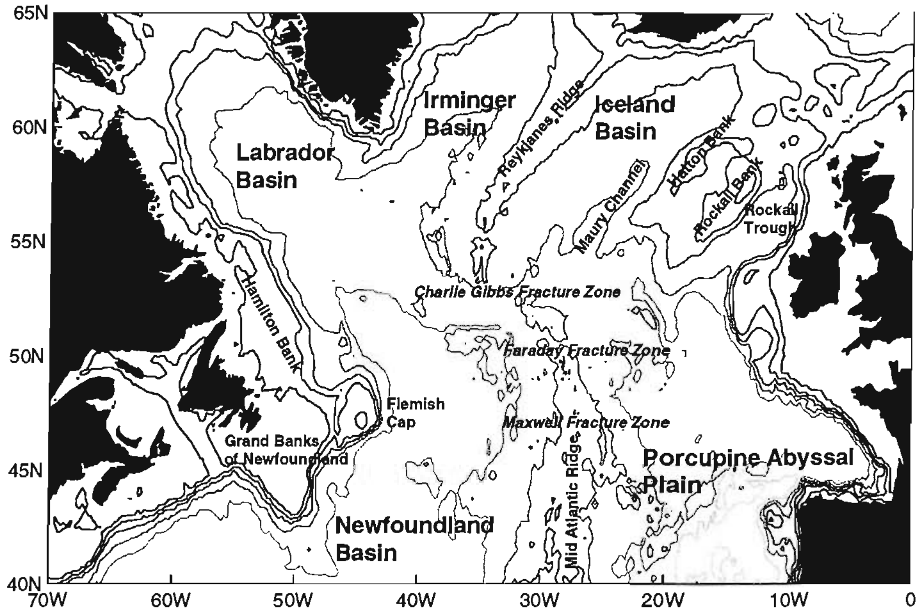

Figure 2.1: Bathymetry of the Subpolar North Atlantic. *Isobaths are contoured at every 1000 m from 5000 m (light grey) up to 1000 m (dark grey) and at 200 m (black).*

basins to the south. To the east and west the Subpolar North Atlantic is bounded by continental landmasses with an abyssal escape to the south.

[7] Separating the deep ocean of the east and west Subpolar North Atlantic is the Mid-Atlantic Ridge (MAR), starting to the south of Iceland as the Reykjanes Ridge. Along the MAR are a series of fracture zones; Charlie Gibbs Fracture Zone (CGFZ), Faraday Fracture Zone and Maxwell Fracture Zone, that are thought to topographically steer the mean flow. The steep contours of the continental slopes and the MAR guide the major currents around the Subpolar North Atlantic Ocean with various submarine banks, channels and troughs adding to the complexity of the circulation.

2.3 Ocean Circulation

[8] Climate of the Subpolar North Atlantic is strongly influenced by the Gulf Stream (GS), as a significant proportion of the meridional ocean heat transport into this region is associated with this system (Rago and Rossby, 1987). Direct velocity observations of the GS suggest that the combined baroclinic and barotropic transport is of the order of 150 *Sv* and in part determined by the dynamics of two counter-rotating gyres to the north and to

the south (Hogg, 1992). After leaving Cape Hatteras the GS meanders eastward to 65°W where it is suggested that the Stream decelerates before bifurcating into several smaller currents (Reverdin *et al.*, 2003). In addition, there is a *step-like* jump in the position of the GS core between the longitudes of 65°W and 60°W associated with the New England Seamounts (63°W, 38°N; Fratantoni, 2002). According to Frankignoul *et al.* (2001) it is the intense heat loss from the GS system that drives the storm track, which is focussed towards the European continent in the winter months.

[9] One of the currents that splits from the GS and Subtropical Gyre, between 54°W and 50°W, is the North Atlantic Current (NAC; Lazier, 1994, Reverdin *et al.*, 2003) which flows northward along the Grand Banks of Newfoundland hugging the steep topographic contours of the continental slope (Kearns and Rossby, 1998). A second current flows southward and eastward as the Azores Current towards the African coast. The NAC is an important component of the Meridional Overturning Circulation (MOC), acting as a pathway for thermodynamic exchange between the Subtropical and Subpolar Gyres. Continuing around the Flemish Cap the NAC turns sharply eastwards between 51°N and 52°N at the *Northwest Corner* (Lazier, 1994) and crosses the MAR between 50°N and 52°N into the eastern Subpolar North Atlantic as at least two jets (Krauss, 1986, Sy *et al.*, 1992, Schmitz and McCartney, 1993, Kearns and Rossby, 1998, Reverdin *et al.*, 2003). The most northerly of these jets is thought to be topographically constrained at the CGFZ (Sy *et al.*, 1992). To the south of the CGFZ the remaining jets exhibit increasing variability in strength and composition (Sy *et al.*, 1992, Reverdin *et al.*, 2003).

[10] The transport and nature of the NAC has been re-evaluated several times since Worthington (1976) presented his North Atlantic Circulation scheme. Schmitz and McCartney (1993) suggest that the total transport of the NAC is of the order of 37 Sv in the upper ocean. Of this northward transport 25 Sv is contained within a closed gyre, with an additional 36 Sv recirculating in the intermediate and lower ocean. This is in agreement with the value of 50 Sv suggested by Meinen *et al.* (2000) that recirculates as the large permanent anticyclonic *Mann Eddy* (Mann, 1967) in their analysis of WOCE hydrographic line ACM6 at 42.5°N. However, the remaining transport of 12 Sv northward to the Iceland Basin, coupled with the 13 Sv transport of intermediate waters around the Subpolar Gyre proposed by Schmitz and McCartney (1993) is less than discussed by Meinen (2001).

[11] Other estimates of upper ocean transport in the NAC are of around 44 *Sv* (Krauss *et al.*, 1987), with a branching to the east and north at 47°N 41°W, although these branches are not thought to be permanent features of the system. Lazier (1994) observed that the mean flow of the NAC between 50.5°N and 51°N is considerably stronger and more baroclinic in nature than to the north, with more of the energy coming from the mean rather than the eddying flow. Relative to 4200 *m* he calculated the transport to the east of the Flemish Cap to be of the order 40 *Sv* to 44 *Sv*. Meinen (2001) proposes 50 *Sv* around the *Northwest Corner* and to the east a decreased transport of around 30 *Sv* across the MAR, 4 *Sv* more than Sy *et al.* (1992) calculate using a 2000 *m* reference level.

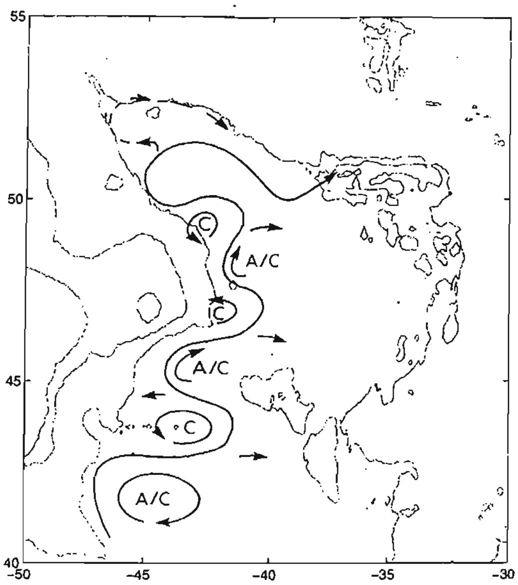

Figure 2.2: Pathway of the North Atlantic Current through the Newfoundland Basin. *Rossby's (1996) interpretation of the meandering yet temporally stationary features of the NAC and probable pathways of eastward flowing tributaries (indicated by the arrows) to the south of the main NAC core at 51°N.*

[12] Kearns and Rossby (1998) suggest that the pathway of the NAC in the Newfoundland Basin is constant and topographically controlled with stationary meanders of the order 300 *km* in wavelength (Figure 2.2). The generation of these meanders is due to the prominent features of the Southeast Newfoundland Rise, the Flemish Cap (Rossby, 1996) and the Newfoundland Seamounts (Kearns and Rossby, 1998). In a simple model study Kearns and Paldor (2000) suggest that in fact it is the stability of the NAC that allows its path to follow these bathymetric contours.

[13] Entering the Newfoundland Basin from the north, cooler waters of Subpolar origin encounter the northward flowing NAC of warmer more saline Subtropical origin forming a strong frontal system known as the Subpolar Front (SPF). The horizontal distributions of heat and salt persist in this region over both summer and winter months forming a permanent frontal boundary (Dietrich, 1969). This frontal system runs northward along the continental shelf of Newfoundland above the 3500 *m* isobath, before turning eastward

around 52°N (Lazier, 1994). Outside the Newfoundland Basin the front follows a northward trajectory into the Iceland Basin closely associated with the pathway of the most northerly of the NAC jets.

[14] Several lesser known fronts are identified by Belkin and Levitus (1996). At 45°N to 47°N lies the Mid-Atlantic Front and at 39°N the Mediterranean Water Front. They also describe the bifurcation of the SPF (also termed the *Subarctic Front* by some authors) into the Northern and Southern Subpolar Fronts close to 35°W. Water mass exchange across these fronts, transferring properties between the two gyre systems, has important implications on the dynamics of the region (Dutkiewicz *et al.*, 2001). In recent *in situ* studies floats are observed to move between fast flowing jet waters to slower surrounding waters, illustrating the potential for tracer fluxes across these frontal regions (Dutkiewicz *et al.*, 2001). This exchange is also found to occur in both the upper and intermediate ocean (Zenk, 2000).

[15] There appears to be great debate as to the nature of the NAC and its associated tributaries and fronts as it passes over the MAR. It is unclear whether the character of the NAC remains as a series of jets passing eastward across the MAR or whether it degenerates into an eastward drift with no discrete frontal boundary associated with it. Krauss (1986) disagreed with the branched structure of the NAC proposed by both Dietrich *et al.* (1975) and Worthington (1976) favouring the idea of the eastward drift. Although many authors refer to the NAC *jets*, Rossby (1996) suggests that with the NAC's strongly diffusive flow there appears to be no mechanism for generating any such zonal jets. Many authors now simply refer to the NAC as a highly variable flow, with no real fixed structure. Bower *et al.* (2002), however, note the influence of the topography as the NAC passes from the Newfoundland Basin across the MAR (Figure 2.3), acting to focussing the flow over the fracture zones.

[16] Once in the Iceland Basin the NAC turns to the north. The specific location at which this occurs varies. It is clear, however, that waters of Subtropical origin are transported northward between 30°W and 23°W into the Iceland Basin and Rockall Trough (e.g. Fratantoni, 2002, Reverdin *et al.*, 2003, Pollard *et al.*, 2004). East of the MAR waters associated with the NAC have been shown to follow several pathways. One northward at around 30°W. This bypasses the longer cyclonic route around the Iceland Basin and enters

the Irminger Sea north of 54°N (e.g. Dietrich, 1969, Pollard *et al.*, 2004). Another pathway is found to pass northeastward along the Maury Channel into the northern Iceland Basin(e.g. Heywood *et al.*, 1994, Orvik and Niiler, 2002, Reverdin *et al.*, 2003). This pathway then follows the bathymetric contours of the Basin before recirculating southward along the eastern flank of the Reykjanes Ridge and into the Irminger Basin south of 60°N (Pollard *et al.*, 1999). From surface drifter trajectories Orvik and Niiler (2002) suggest that there is in fact a small transport pathway to the south of Iceland across the Reykjanes Ridge and an additional flow across the Iceland-Faroe shelf into the Nordic Seas from this current system. The third notable pathway is through the Rockall Trough and towards the Nordic Seas (Orvik *et al.*, 2001) with a possible recirculation into the northern Iceland Basin (Pollard *et al.*, 2004). There has also been observational evidence of a pathway to the south and east along the Celtic Shelf towards France (Zenk, 2000, Fratantoni, 2002).

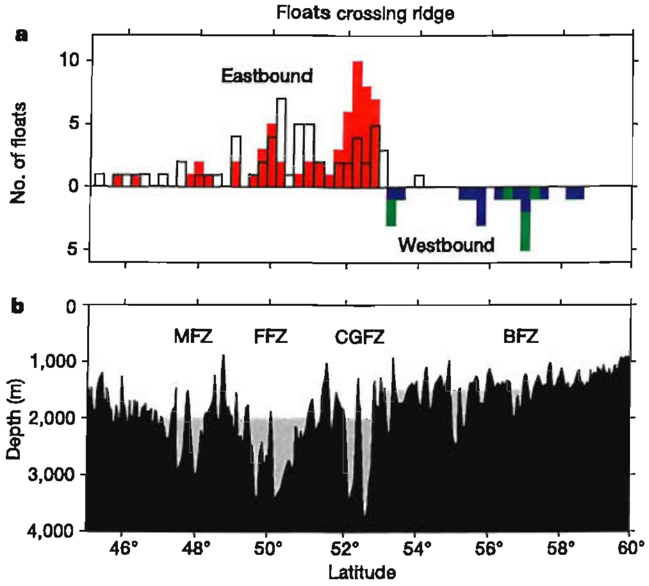

Figure 2.3: Distribution of floats passing over the Mid Atlantic Ridge. *This figure, from Bower* et al. *(2002), highlights the probable pathways that the NAC follows across the MAR. Plot a shows the distribution of floats passing over the MAR at a given latitude and plot b the topographic profile along the ridge system. The unfilled bars in the upper plot indicate the deployment latitudes of the floats. The fracture zones referenced in the lower plot are the Maxwell Fracture Zone (MFZ), the Faraday Fracture Zone (FFZ), the Charlie Gibbs Fracture Zone (CGFZ) and the Bight Fracture Zone (BFZ).*

[17] From hydrographic data Bacon (1997) determines an approximate transport of 19 Sv travelling northward across 53°N as the NAC. Orvik *et al.* (2001) suggest that waters from the Rockall Trough and the Iceland Basin feed the Norwegian Current with a total inflow to the Nordic Seas across the Svinoy section of the order 4.2 Sv in the eastern branch, originating from the Rockall Trough region, and 3.4 Sv in the western branch, originating in the Iceland Basin. The difference between the water mass properties of the

NAC and Subpolar Gyre in the Iceland Basin are still sufficient to form a frontal zone that is baroclinically unstable (Heywood *et al.*, 1994, Schott *et al.*, 1999).

[18] To the west, waters entering the Irminger Basin from the Labrador and Iceland Basins form the poleward Irminger Current on the westward flank of the Reykjanes Ridge present from 57°N (Reverdin *et al.*, 2003), the magnitude of which has been estimated to be of the order of around 9-10 Sv in the upper ocean (Krauss, 1995, Bacon, 1997). The flow on the opposing flanks of the Reykjanes Ridge are very different in nature (Reverdin *et al.*, 2003), with the transport on the westward flank associated with a frontal zone (Bersch *et al.*, 1999) and a local eddy kinetic energy maximum (Heywood *et al.*, 1994). This frontal feature along the westward flank of the Reykjanes Ridge is similar in nature to that of the Subpolar Front (Reverdin *et al.*, 2003). The poleward flowing waters of the Irminger Current follow the bathymetric contours as weakly cyclonic circulation around the Irminger Basin, centred on 61°N 36°W (Reverdin *et al.*, 2003), where it encounters the East Greenland Current (EGC), an outflow from the Nordic Seas. The EGC transports approximately 3 Sv southward along the Greenland coastal shelf as a seasonally varying surface current of Polar and Arctic Intermediate Water composition (Foldvik *et al.*, 1988). During periods of high ice melt along the coast of Greenland there is a strong frontal boundary initiated between the EGC and Irminger Current both flowing southward towards Cape Farewell. Bacon (1998) observed salinities of less than 30 in the EGC and Krauss (1995) less than 33.3 in the outer flank of the current with the Irminger Current relatively warmer and more saline at 34.9-35.0 and 4-5°C, in contrast to waters of -1.5°C in the EGC. Transport southward in the upper ocean is of the order 18 ± 3 Sv in the Irminger Basin according to inverse calculations by Bacon (1997), with a total southward flow of the order 26-27 Sv compared to 21 Sv proposed by Schmitz and McCartney (1993).

[19] At Cape Farewell the EGC turns northward into the Labrador Basin as the West Greenland Current, still flanked by the Irminger Current (now the Labrador Current). The frontal boundary between these two currents results in a region of relatively high eddy activity through the generation of baroclinic instabilities (Cuny *et al.*, 2002, Prater, 2002). At around 62°N there is another region of high eddy activity where the boundary current separates from the continental shelf. This appears to occur in response to a divergence in the bathymetric contours, with flow continuing along the 3000 m isobath

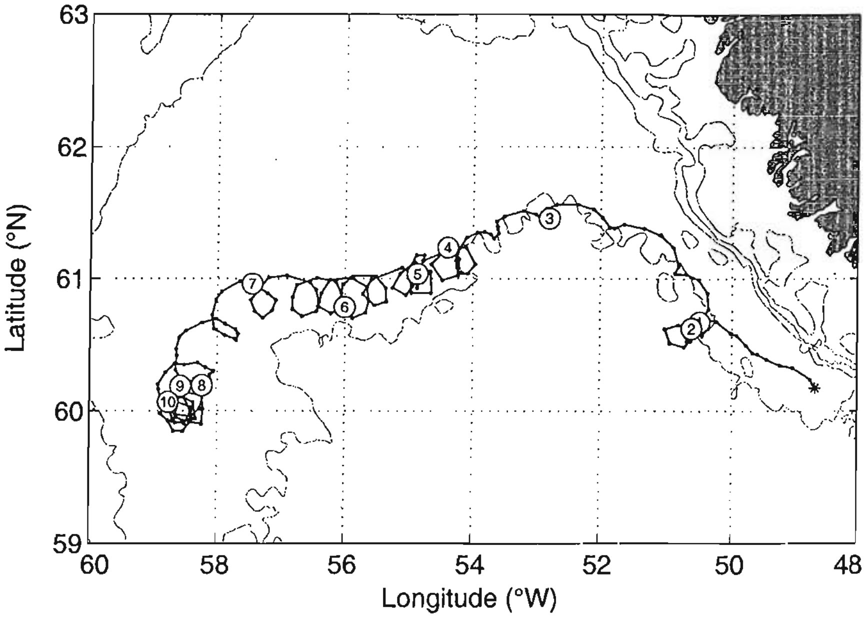

Figure 2.4: The trajectory of a RAFOS profiling float in the Labrador Basin from Prater (2002). *The float, with an equilibrium depth of 375 m, illustrates the separation of the West Greenland Current between 61°N and 62°N and its subsequent pathway into the interior Labrador Sea between the 2000 m and 3000 m isobaths. The circled numbers indicate profiles at 7-day intervals.*

into the interior of the Labrador Basin (Figure 2.4). Although the eddy kinetic energy in this region is relatively high it is still an order of magnitude smaller than that found in the Gulf Stream (Fratantoni, 2002).

[20] Cuny *et al.* (2002) observe speeds in the boundary current of 90 cms^{-1} at Cape Farewell and 95 cms^{-1} northward at Cape Desolation centred on the 2000 m isobath. At around 61°N speeds drop to 70 cms^{-1} with a further reduction thereafter, as a result of the divergence in the isobaths and instabilities generated between the boundary and interior water masses. These speeds are in close agreement with those observed by Krauss (1995), who suggests that the current slows to 40 cms^{-1} between 60°N and 62°N. Typical transit times around the Labrador Basin are of the order 147 to 185 days (Cuny *et al.*, 2002). Prater (2002) speculates that the advection of eddies and Irminger Water from the boundary current into the interior of the basin may play a role in restratification of the Labrador Sea in late spring coinciding with a peak in eddy activity. It is unlikely that these eddies are connected in any way to convection in the basin as convective eddies in the Labrador Sea are predominantly anti-cyclonic, smaller and more barotropic in nature than those generated in the Irminger Current (Lilly and Rhines, 2002).

[21] Overturning in the northern North Atlantic is most closely associated with the convective regions of the Greenland (Watson *et al.*, 1999) and Labrador Seas (Marshall *et al.*, 1998). However, from recent sub-surface float measurements in the western Subpolar North Atlantic Lavender *et al.* (2000) identified an intermediate depth cyclonic recirculation in the Irminger Sea, a site of possible deep ventilation (see Figure 2.5, grey contours in the Irminger Basin). Pickart *et al.* (2003) suggest that this site, exposed to cold winter winds from mainland Greenland is the location where overturning in the Irminger Sea is most likely to occur. Straneo *et al.* (2003) illustrate the importance of these recirculation regions of the Subpolar Gyre in the export of Labrador Sea Water to the east. Of these suggested sites of possible deep ventilation, only one site has been observed to be active in production of intermediate and deep water masses (Marshall *et al.*, 1998, also identified in Figure 2.5 by the thick black unshaded contours in the Labrador Basin). The recirculation observed near the *Northwest Corner* and the Flemish Cap (51.5°N, 46°W) is driven by the seasonally variable flow of the Labrador Current in response to the wind forcing (Lavender *et al.*, 2000).

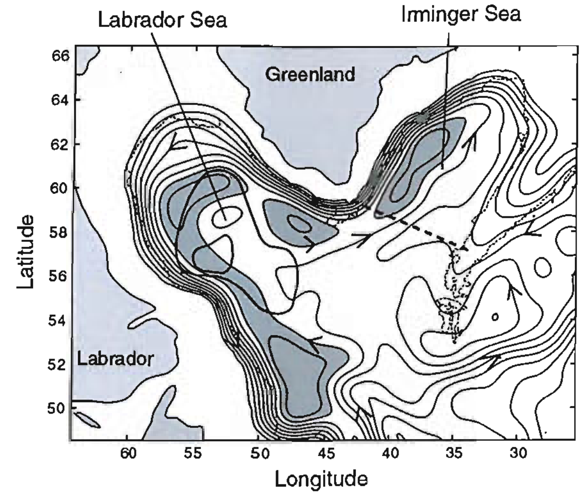

Figure 2.5: The streamfunction derived from float data from Straneo *et al.* (2003) in the Labrador and Irminger Basins. *The cyclonic recirculations, low pressure cells, are indicated by the shaded regions. The thick black contours identify the region of known deep convection.*

[22] Outflow of Labrador Sea Water is via the Labrador Current and Deep Western Boundary Current eastward between 51°N and 54°N and also in the interior northward into the Irminger Basin (Lavender *et al.*, 2000, Pickart *et al.*, 2003, Straneo *et al.*, 2003). Transit times for the passage of Labrador Sea Water from its generation region into the Iceland Basin and the Rockall Trough are estimated to be as little as 2.8 years (Lavender *et al.*, 2000, *cf.* Read and Gould (1992) and Bersch *et al.* (1999)). Ventilated waters are also found on the eastern flank of the MAR south of the CGFZ (Paillet *et al.*, 1998) and are also thought to follow the Deep Western Boundary Current south through the Newfoundland

Basin, although Lavender *et al.* (2000) found no evidence for this. Large scale recirculations at intermediate depths along the pathway of the Gulf Stream and NAC could potentially modulate the residence time of Subpolar waters heading southward (Lozier, 1997).

2.4 Interannual to seasonal ocean variability

The Gulf Stream

[23] As a dynamic link in the heat transfer between the Subtropical and Subpolar regions, any variability in the Gulf Stream may impact on the ocean climate system of the Subpolar North Atlantic. Over the last decade there have been lateral shifts in the Gulf Stream due to variability in the atmospheric forcing according to Frankignoul *et al.* (2001). They found that the axial position of the Stream had shifted by around 2° in latitude southward between 1995 and 1997 (Figure 2.6). Annual variations in the pathway within 100 km of the climatological mean have also been observed by Marotzke *et al.* (2002) and from drifter data by Reverdin *et al.* (2003), although on sub-annual timescales the flow is dominated by more variable characteristics of meanders and large scale eddies or Gulf Stream Rings (Hogg, 1992). Taylor and Stephens (1998) and more recently Frankignoul *et al.* (2001) demonstrated, using a correlation analysis, that the fluctuations in Gulf Stream were lagged to one of the principal atmospheric modes of variability the North Atlantic Oscillation (NAO, see section 2.5). Although Frankignoul *et al.* (2001) found no evidence to suggest variability in the Stream's position on seasonal time scales, Kelly *et al.* (1999) suggest that there is a seasonal cycle in the surface transport and position similar to that of the atmospheric jet stream. The position of this atmospheric jet stream is to the north in fall and the south in the spring months (Tracey and Watts, 1986).

The Newfoundland Basin

[24] Yaremchuk *et al.* (2001) use both observational data and data from model assimilation to estimate the seasonal variability in the strength of the NAC in the Newfoundland Basin. They conclude that a peak in transport occurs during April-May of 61±5 Sv with a minimum of 42±3 Sv in October-November across 40°W, between 40°N and 55°N. They also find that there is a seasonal variation in vertical transport across 1000 m of the order 2

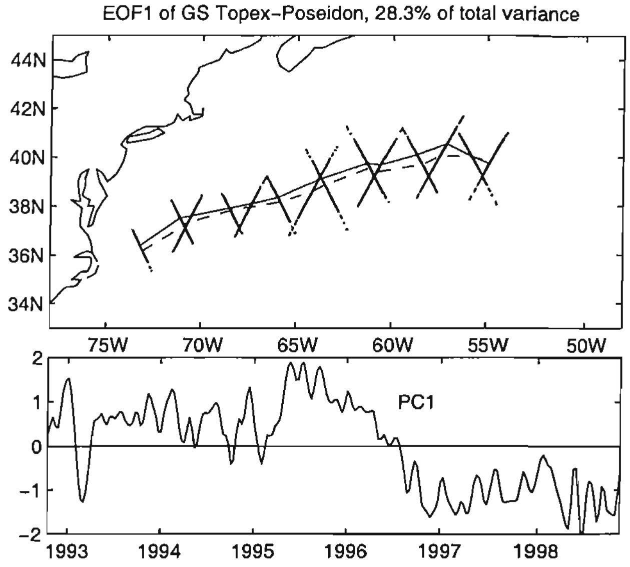

Figure 2.6: The first Empirical Orthogonal Function (EOF; *top*) and associated Principal Component (PC; *bottom*) of the Gulf Stream pathway from Frankignoul *et al.* (2001). *The PC indicates the lateral shifts in the core of the Stream, with the most northerly position observed in 1995 before moving to a more southerly position in 1997 and 1998.*

Sv. Both the horizontal advection of water masses, contributing to the seasonal buoyancy budget, and winter convection are shown to influence the circulation in this region.

[25] The pathways of the NAC east of 45°W follow a *wider variety of trajectories* across the Newfoundland Basin, whereas to the west of 45°W they appear to follow a more consistent path northward to the *Northwest* Corner (Kearns and Rossby, 1998, Kearns and Paldor, 2000, Reverdin *et al.*, 2003). Lazier (1994) points out , however, that there is a highly variable flow regime in the *Northwest* Corner and that it could exist in two different states varying on a time-scale of the order of months. The first state is a well defined, narrow and coherent flow between 48°N, 43°W and 51°N, 44°W (mid point of the *Northwest* Corner), the second a weaker and less coherent flow of multiple ill-defined pathways. The mechanism for this appears to be storm related, leading to cross frontal exchange and the horizontal displacements of the current. Lazier (1994) also notes the persistence of 100 *km* anticyclonic eddy structures east of the *Northwest* Corner.

[26] The two most northern branches of the NAC are better defined than to the south where the flow appears a little more ambiguous in both strength and position (Sy *et al.*, 1992, Belkin and Levitus, 1996, Reverdin *et al.*, 2003). The most northern of the NAC branches, the Subpolar Front, exhibits significant interannual variability in its trajectory

across the southern Subpolar North Atlantic (Belkin and Levitus, 1996). Excursions northward (southward) of 200-to-300 *km* are observed in the Newfoundland basin, while to the east of the MAR there are corresponding southward (northward) shifts of the order 200 *km*. Along 35°W the frontal position appears to remain within a 55 *km* window under the premise that the flow is topographically controlled as previously discussed. Eden and Willebrand (2001) argue that fluctuations in the atmosphere impose a cyclonic circulation anomaly centred on the Subpolar Front. The anomalous circulation advects warm saline waters across the front into the western Iceland Basin, analogous to the northward shift east of the MAR observed by Belkin and Levitus (1996). This idea is similar to that proposed by White and Heywood (1995), who suggest that latitudinal shifts of the Subpolar Front are in concert with that of the zero in the wind stress curl.

[27] From over twenty years' worth of drifter data Reverdin *et al.* (2003) identify the *climatological* locations of northern most branches of the NAC at 50°N and 52°N to the west of 32°W, but find these positions to be less well defined further to the east. The results from two hydrographic cruises (Pollard, 1996, Schott *et al.*, 1999) suggest that the 55 *km* window observed by Belkin and Levitus (1996) maybe an under estimate of the variability over the MAR. Pollard (1996) observed the northern branch of the NAC to be around 50.8°N in 1991 with a clear indication of the southern branch at 48.5°N. In August of 1997 there was an apparent excursion of the NAC to north of its climatological mean (Schott *et al.*, 1999). The depth to which the NAC extended during this period is thought to have prevented the passage of Labrador Sea Water through the CGFZ, thus altering the circulation in the Subpolar North Atlantic Ocean.

The Eastern Subpolar North Atlantic Ocean

[28] Using data from a series of hydrographic surveys across the Subpolar North Atlantic Ocean, Bersch *et al.* (1999) discovered a significant change in the baroclinic structure across the Iceland Basin over the period 1991-to-1996. They suggest that the resultant shift in the Subpolar Front westward may have been caused by either a reduction in the Ekman upwelling or the heat flux to the atmosphere. Another plausible mechanism for the observed variability could be through the advection of anomalous water mass characteristics of Subtropical origin into the region (Eden and Willebrand, 2001). Figure 2.7 illustrates the shift in the front between 1995 and 1996 through a large temperature

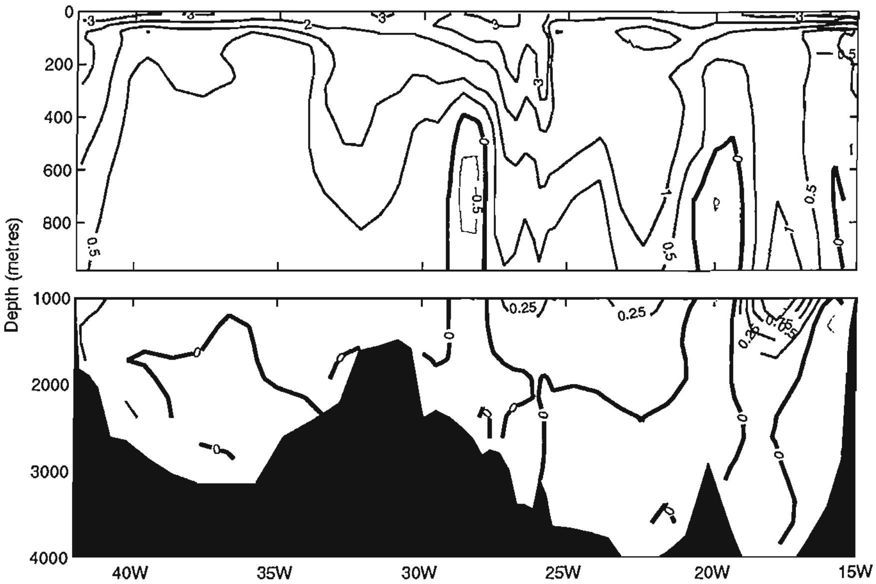

Figure 2.7: Westward shift in the Subpolar Front in the Iceland Basin between the years 1996 and 1995. *Potential temperature difference along the WOCE AR7E hydrographic line spanning from southern Ireland to the Cape Farewell on the southern tip of Greenland.*

difference in the upper and intermediate ocean between 28°W and 25°W. This westward shift in the frontal position acted to impede the spreading of Labrador Sea Water to the eastward limits of the Iceland Basin in 1996 (Bersch *et al.*, 1999).

[29] Large scale shifts in the frontal zone have also been inferred through the use of satellite altimetry (Heywood *et al.*, 1994, White and Heywood, 1995). White and Heywood (1995) suggested that variability on both seasonal and interannual time scales can be associated with the atmospheric forcing. They find that there is a seasonal strengthening of NAC across the MAR during the winter months and evidence of lateral shifts in the current in response to changes in the wind stress curl.

[30] In 1991 Pollard (1996) observed two branches of the NAC turning northward across 54°N between 24°W and 23°W and between 22.2°W and 21°W. In 1996 Pollard *et al.* (2004) identified two clearly defined branches of the NAC, again crossing 54°N into the Iceland Basin, but on this occasion further to the west. In contrast to 1991 the more northerly of the two branches turned north at 30°W and the southern branch at 25°W. There are also suggestions of the possible transport of NAC waters northward along the eastern flank of Reykjanes Ridge east of the CGFZ (Krauss, 1996, Schott *et al.*, 1999).

Accompanying this broad range of trajectories the strength of the flow into the Iceland Basin appears to be influenced on interannual time scales by the NAO (Flatau *et al.*, 2003, Reverdin *et al.*, 2003).

[31] Orvik *et al.* (2001) suggest from a 2 year time-series that variability of the Atlantic inflow to the Nordic Seas also exhibits a *strong* connection to the NAO. It should be noted, however, that the two years in question both have peaks in the NAO during the winter months coinciding with peaks in transport, therefore may just exhibit a strong correlation to the seasonal cycle.

The Western Subpolar North Atlantic Ocean

[32] It is believed that the long term variability of convection in the Labrador Sea is somewhat dictated by variations in the atmospheric forcing. Pickart *et al.* (2002) stress, however, that there is no simple relationship between ocean and atmosphere. The Labrador Sea has sufficient convective memory that even during a mild winter of weaker winds significant convection can still occur (Straneo *et al.*, 2003). In February 1997 there was one such event. The relatively high heat flux from the Labrador Sea during the early 1990s had preconditioned the water column sufficiently such that convective activity was triggered with minimal forcing (Pickart *et al.*, 2002). In addition to the interannual signal there has also been a notable freshening of the Labrador Sea over the latter half of the last century (Dickson *et al.*, 2002), which may impact on the circulation in the Subpolar Gyre region as a whole.

[33] Over the past decade there has also been a significant change in the sea surface height, of the order of 5 to 6 *cm*, in the western Subpolar North Atlantic between the years prior to the winter of 1995/6 and those after (Reverdin *et al.*, 1999, Figure 2.8). The winters of 1995/6 and 1996/7 exhibited relatively weaker winds over the Labrador Basin and an associated reduced heat flux. This lead to a heat gain in the upper ocean and an increased steric contribution to the sea surface height. Reverdin *et al.* (1999) estimated the steric height change to be around the order of 4 *cm* attributing the additional heat gain with anomalous advection of warmer waters into the region.

[34] Coupled with the changes in sea surface height has been a transition over the last

decade in the nature of eddies in the Labrador Sea (Lilly *et al.*, 2003). The latter half of the last decade has seen the persistence of long lived boundary current eddies in the Labrador Sea. This longevity is thought to be a feature of the weaker heat fluxes and shallower convection of the mid to late 1990s. Prior to this there was an abundance of smaller convective eddies. These eddies also exhibit a strong seasonality, which is associated with the strength of the boundary current system. Peak eddy kinetic energy values associated with this boundary current are observed in early spring (Heywood *et al.*, 1994, Prater, 2002). In the West Greenland Current the seasonal differences in the transport are suggested to be due to the break down of the coastal front and hence baroclinic transport (Myers *et al.*, 1989). On the opposite side of the basin along the Labrador coast Hansen and Larsen (1999) calculate seasonal differences in the transport of the Labrador Current to be of the order of 10 to 17 Sv, peaking in fall to winter.

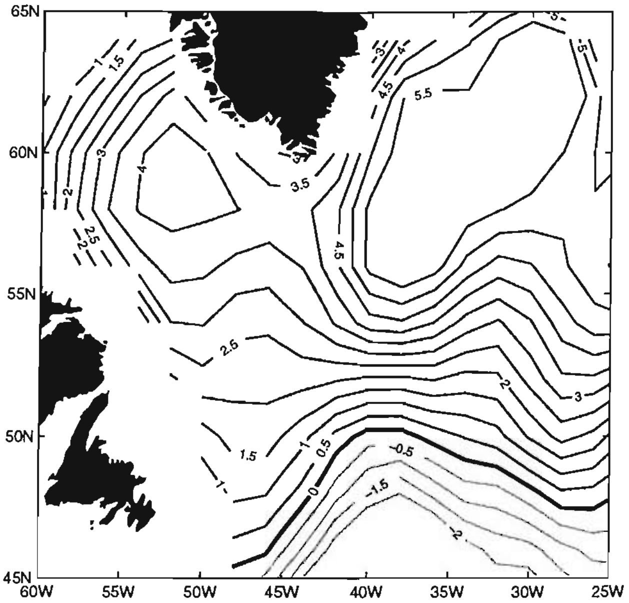

Figure 2.8: Sea surface height difference between years 1996 and 1995 in the western Subpolar North Atlantic Ocean from the Topex/Poseidon satellite altimeter. *Sea surface height difference is contoured every half a centimetre, black contours are positive and grey negative, with the thick contour as zero.*

2.5 Atmospheric variability

[35] As the winds blow over the world's ocean there is a transfer of momentum between the air and the sea. The atmosphere imparts a force per unit area:

$$\tau = \tau_x \hat{\imath} + \tau_y \hat{\jmath} \tag{2.1}$$

the zonal and meridional wind stress, on the ocean's surface. Figure 2.9 shows the eastward wind stress at 55°N over the Subpolar North Atlantic Ocean between 1992 and 2002. This

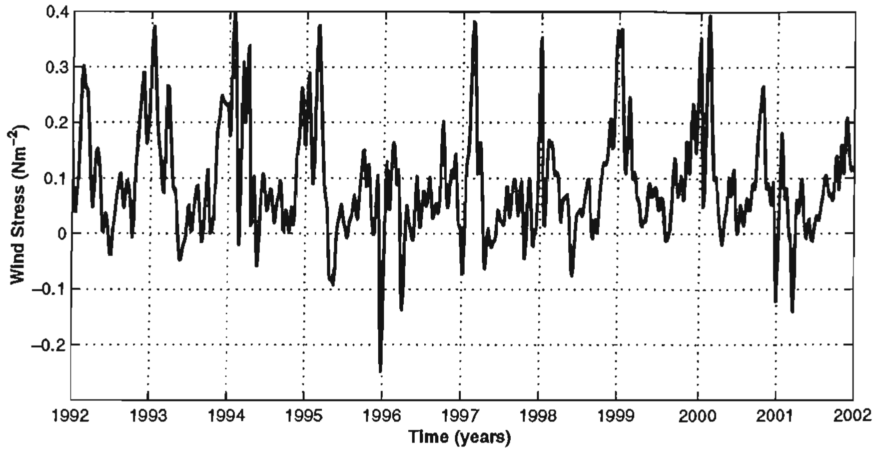

Figure 2.9: Mean zonal wind stress at 55°N in the Subpolar North Atlantic between 1992 and 2002.

stress exerted on the surface of the ocean is an important driving force of current systems. Thus, variations in the wind field are closely linked to the variability we see in the oceans.

[36] The transfer of momentum from the atmosphere to the ocean gives rise to what is termed Ekman transport, a transport in the oceanic boundary layer. As the wind blowing over the ocean is non-uniform, so to is the transport in this oceanic boundary layer. Variations in Ekman transport lead to a convergence of mass in some regions and a divergence in others. This is compensated in the vertical with mass being replaced or expelled at a rate equal to the divergence or convergence in the oceanic boundary layer. This vertical motion or Ekman Pumping velocity (w_E) drives ocean currents and can be expressed in terms of the curl in the wind stress ($\nabla \times \tau$):

$$w_E = (f\rho)^{-1}(\frac{\partial \tau_y}{\partial x} - \frac{\partial \tau_x}{\partial y}) = \frac{\nabla \times \tau}{f\rho} \tag{2.2}$$

where f is the coriolis parameter and ρ some reference density. A map of the mean wind stress curl over the Subpolar North Atlantic is shown in Figure 2.10.

[37] One of the leading modes of atmospheric variability in the Subpolar North Atlantic Ocean is the North Atlantic Oscillation (NAO) and describes the variable pressure gradient between the Azores High and the Icelandic Low. It is the leading mode of variability in the North Atlantic throughout most of the year, accounting for around one third of the hemispheric variance in the dominant winter months (Hurrell, 1996). Several indices have been constructed to describe the variable nature of this atmospheric mode (e.g. Rogers,

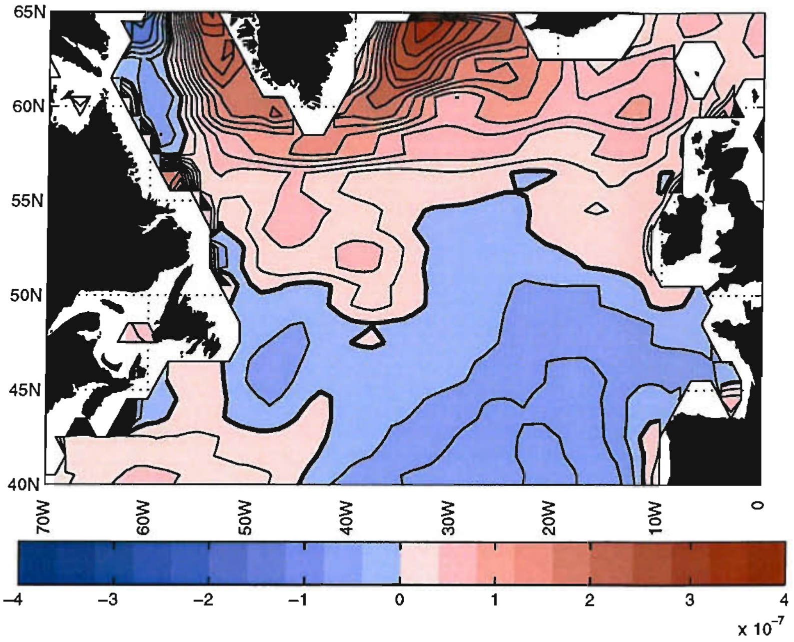

Figure 2.10: The mean wind stress curl over the Subpolar North Atlantic Ocean for the period 1992-2001. Units are in Nm^{-3}.

1984, Hurrell, 1995, Jones *et al.*, 1997). These indices are constructed as measures of the difference in *standardised* Sea Level Pressure (SLP) at two locations near the centres of action. *Standarised* means that the time series have had their means removed and have been divided by their standard deviation to create a new time series (*Stephenson pers.comm.*). If this process were not performed the low pressure measurement over Iceland would dominate the indices.

[38] Station Based Indices (SBI)[2] are unable to capture the full extent of the respective pressure systems as the NAOs centres of action vary both spatially and temporally. During the summer months the choice of station location will change the characteristics of the NAO index, although this not so evident in the more robust winter months. SBI measurements are also subject to local atmospheric variability not directly associated with the NAO and hence will contain a certain degree of noise.

[39] An alternative to SBIs is Empirical Orthogonal Function (EOF) analysis (see Appendix B for a summary). The Principal Component (PC) times series of the leading

---

[2] Indices constructed from measurements of two ground based stations near the centres of action of the NAO. Typically the northern station is in Iceland and the southern station is either in the Azores or Lisbon.

EOF of sea level pressure (SLP) is used as a dimensionless index of the NAO. The EOF approach allows a better representation of the NAO and its spatial pattern, although it only covers periods when adequate SLP products have been available. As the time series we are considering in this study is relative short this type of index would be preferable to SBIs. However, although this technique captures the spatial and temporal variability of the NAO with more accuracy than the SBIs, the analysis is still dependent on the extent of the region analysed. In addition, as the index is a *standardised* measure of variability it will also change as the record length increases. It is therefore noted that there is no unique and universally accepted way to describe the NAO (Hurrell, 2003).

[40] In an NAO positive phase, NAO^+, there is a pronounced high pressure system over the Azores region and a deepening of the low near Iceland and Greenland. Associated with the increased pressure gradient are strong westerly storm events focussed over northern Europe (Hurrell, 1995), bringing with them relatively warmer maritime air during winter and spring months. In the opposite extreme of an NAO negative phase, NAO^-, the two pressure cells reduce in magnitude, weakening the pressure gradient and focusing weaker westerly winds over southern Europe. In this phase of the oscillation, northern Europe and the east coast of the United States of America experience relatively colder drier winters, while southern Europe and Greenland experience milder climatic conditions. The wind stress, freshwater flux and heat flux anomalies are inherently linked to the NAO. Variations in the atmospheric forcing due to the NAO will ultimately feed into the ocean system. Figure 2.11 illustrates the close link between the NAO and sea surface height anomaly (SSHa) of the Subpolar North Atlantic Ocean. The spatial pattern of an EOF analysis of SSHa, associated with the NAO, reveals a dipole with centres of action in the Subpolar Gyre and to the south in the Subtropical Gyre. The winter-time NAO-index agrees well with the first Principal Component of the EOF analysis. During NAO^- periods there is a positive SSHa to the north of the zero line and negative to the south. This effectively reduces the sea surface height gradient across the boundary between the two gyre systems. Conversely the gradient increases during an NAO^+ phase. These variations in sea surface height are connected to the changes in large-scale circulation and subsequent transport of heat around the ocean (Eden and Willebrand, 2001, Esselborn and Eden, 2001). Inter-annual fluctuations between the extrema of the NAO-index have also been suggested to

influence the strength and position of the NAC (Bersch, 2002, Flatau *et al.*, 2003). Similar examples of the NAO signature in oceanic fields can be found in the pattern of sea surface temperature anomalies (Rodwell *et al.*, 1999) and in the extent of winter time convection (Pickart *et al.*, 2002).

[41] In addition to the NAO other modes, of atmospheric variability have previously been described (e.g. Barnston and Livezey, 1987). Modes such as the Eastern Atlantic mode, although explaining significantly less of the variability (up to 8.9% Barnston and Livezey (1987)) during the NAO dominated winter months, may still hold importance locally or at other periods in the year.

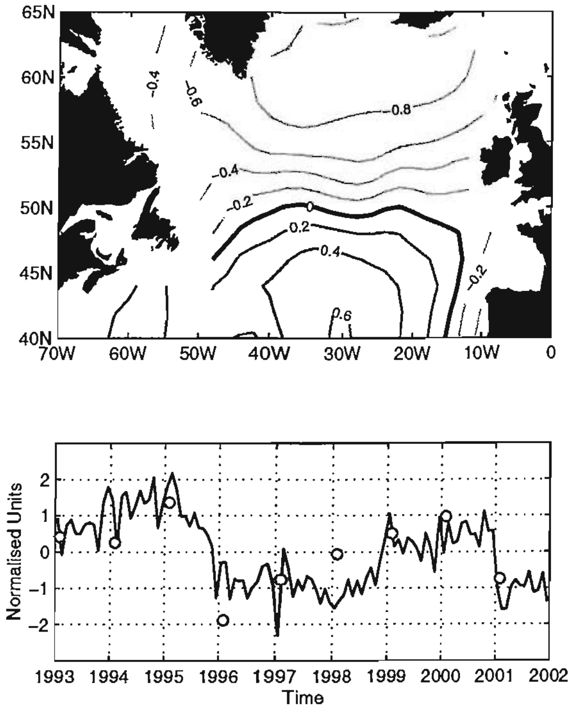

Figure 2.11: The leading mode of and Empirical Orthogonal Function analysis of the sea surface height data from the Topex/Poseidon altimeter. *The spatial pattern is presented as a correlation map, contoured with an interval of 0.2. The % variance explained by the leading mode is 31%. The grey circles indicate the winter time NAO station based index from Jones (2003).*

2.6 Summary

[42] In this chapter an overview of the Subpolar North Atlantic circulation has been presented along with observational evidence for mesoscale to basin-scale variability on seasonal to interannual time-scales.

[43] Through the use of observational and model data we aim to provide further description of the variability of the Subpolar North Atlantic and gain a more extensive understanding of the mechanisms involved. In particular we investigate the variability of the strength and position of the Subpolar Front as an indicator for changes in the large-scale circulation in

this region. Moreover, using an Ocean General Circulation Model (OGCM) we examine the mechanisms involved in the variability of both the horizontal and overturing circulation. Data from the satellite altimeter Topex/Poseidon and the Estimating the Circulation and Climate of the Ocean (ECCO) OGCM are used to carry out the investigation.

[44] A summary of the key questions:

- How has the position of the Subpolar Front and the large-scale circulation changed over the last decade?
- Is the ECCO OGCM realistic in its representation of the Subpolar North Atlantic Ocean?
- What are the mechanisms controlling the large scale variability in the horizontal and overturning circulation?

Chapter 3

Surface eddy kinetic energy measurements of the Subpolar Gyre

3.1 Introduction

[1] While it is known that there is a strong relationship between the phase of the North Atlantic Oscillation (NAO) and the presence of a tripole pattern in sea surface temperatures in the North Atlantic Ocean (e.g. Cayan, 1992), there is comparably little understanding of any NAO induced changes in circulation in this region. Assuming that the measurement of transient eddy kinetic energy (EKE) is a good proxy for the position of the frontal regions (Heywood *et al.*, 1994, Beckmann *et al.*, 1994) we can examine the interannual variability in the surface circulation in the Subpolar North Atlantic Ocean using satellite altimeter data.

[2] The surface circulation in the Subpolar North Atlantic Ocean has already been described in detail in Chapter 2, but we reiterate the key points. The large scale circulation primarily consists of the northward flowing North Atlantic Current (NAC), the cyclonic Subpolar Gyre (SPG) and the southward flowing East Greenland Current (EGC). The NAC departs from the Gulf Stream and Subtropical Gyre between 54°W and 50°W (Lazier, 1994, Reverdin *et al.*, 2003). It then flows northward along the Grand Banks of Newfoundland hugging the steep topographic contours of the continental slope. Continuing around the Flemish Cap, the NAC turns sharply eastwards between 51°N and 52°N (Lazier, 1994) and crosses the Mid Atlantic Ridge (MAR) between 50°N and 52°N into

the eastern North Atlantic as at least two branches (Krauss, 1986, Sy *et al.*, 1992, Kearns and Rossby, 1998, Reverdin *et al.*, 2003). The most northerly of these branches is thought to be topographically constrained at the Charlie Gibbs Fracture Zone (CGFZ) (Sy *et al.*, 1992). To the south of the CGFZ the remaining branches exhibit increased variability in strength and composition (Sy *et al.*, 1992, Reverdin *et al.*, 2003).

[3] The more northerly of these branches feeds the circulation around the Iceland Basin and across the Reykjanes Ridge into the Irminger Basin, while the other passes through the Rockall Trough into the Nordic Seas (White and Heywood, 1995, Holliday *et al.*, 2000, Orvik and Niiler, 2002). The modified NAC water passing from the Iceland to the Irminger Basin is transported via the Irminger Current along the west flank of the Reykjanes Ridge. It subsequently turns westward towards the shelf of east Greenland where it joins with the EGC south of the Denmark Strait (Krauss, 1995). This current system passes around Cape Farewell and travels northward as the West Greenland Current before, in part, separating from the coast into the central Labrador Sea. Closing the SPG circulation is the Labrador Current, which continues around the Labrador Basin turning southeastward towards the Grand Banks of Newfoundland, where it encounters the northward flowing NAC. The differing properties of the water masses in the SPG and the NAC give rise to a frontal zone, the Subpolar Front (SPF), a site of mesoscale eddy activity (Heywood *et al.*, 1994, Schott *et al.*, 1999).

[4] Trends in the surface EKE are associated with the over lying surface wind forcing, dynamic instabilities, interactions with topography and buoyancy forcing (Müller and Frankignoul, 1981, Schmitz and Holland, 1982, Stammer and Wunsch, 1999). As the dominant EKE signal is formed by dynamic instabilities associated with the large scale flow and frontal regions we can use satellite altimeter measurements to examine changes in the circulation pathways of the Subpolar North Atlantic Ocean through the location of the SPF. In turn, the magnitude of the signal will provide information about the strength of current. Heywood *et al.* (1994) observed that there had been changes in the latitudinal position of the NAC in the region of the CGFZ using GEOSAT and ERS altimeter measurements. They suggest that in 1987 the northern core of the NAC was constrained by the CGFZ at 52°N, but in 1988 and 1992/3 the high EKE region associated with the SPF was observed further to the south at 49°N and 50°N. White and Heywood (1995) also suggest a *zonal* translation in the Iceland Basin of the northward flowing NAC

in response to a *meridional* shift in the position of the zero in the wind stress curl during these years.

[5] There have also been several studies examining the changes in the large scale circulation pathways in the Subpolar North Atlantic Ocean, in particular shifts of the SPF, using hydrographic data over the last decade (e.g. Bersch *et al.*, 1999). There was an anomalous low in the phase of the NAO during the winter of 1995/6, which will have altered the atmospheric forcing in the region (Eden and Willebrand, 2001). In subsequent years this phase reverts to a high state as it had done so in years prior to 1995. Associated with the change in atmospheric state has been an altered shape and strength of the SPG (Bersch *et al.*, 1999, Curry and McCartney, 2001, Bersch, 2002). Here we use the quasi-synoptic measurement of residual sea surface height from satellite altimeters to examine the interannual and seasonal surface variability of the Subpolar North Atlantic Ocean and hence infer any changes in the large scale circulation pathways that may have occurred over the last decade.

[6] In the remainder of this chapter we will briefly review the data used (section 3.2) and the method employed to derive EKE of the Subpolar North Atlantic Ocean (section 3.3). We will then examine the basin scale distribution of EKE and interannual and seasonal variability of the features described (sections 3.4 and 3.5). Finally we will consider our findings in the light of previous studies (section 3.6) and summarise (section 3.7).

3.2 Altimeter Data

[7] Sea Surface Height (SSH) measurements from the satellite altimeter Topex/Poseidon (T/P) are used in this study. The primary goal of the T/P satellite mission is to study global ocean circulation through the use of precise altimeter measurements (JVT-Topex, 1992). Launched in August 1992 the T/P mission is an ongoing joint venture between the National Aeronautics and Space Administration (NASA) and the Centre National d'Etudes Spatials (CNES). The Topex dual frequency radar altimeter is the primary altimeter in use. There is also an experimental single frequency solid state radar altimeter (Poseidon) operating for relatively short periods in conjunction with Topex. The altimeter has a repeat track time of approximately 10 days.

[8] The data are acquired from the *Global Altimeter Processing Scheme* (GAPS) database at Southampton Oceanography Centre, UK (Snaith, 2000). The GAPS provides a consistent altimeter data set through a series of quality control procedures. The end products, including mean and residual sea surface height, are collocated onto a reference grid using a bilinear interpolation method with a correction employed for any relative changes in the geoid height between the resampled location and the reference point.

[9] The product used in this study has had a series of atmospheric and altimetric corrections applied. In addition, the tidal signal has been removed from the data using a tidal correction model. All data covering regions shallower than 1000 m have been rejected as the tidal model used is unable to remove all the required signal. Since we are only concerned with eddy activity and therefore perturbations in the SSH, no knowledge of the marine geoid is required. The SSH anomalies used are calculated relative to a three year mean (see Snaith, 2000, for more details).

3.3 Deriving eddy kinetic energy

[10] The horizontal kinetic energy, per unit mass, can be broken into two parts. The first, mean kinetic energy, is derived from the mean flow over the period of the study. The second, the EKE, is derived from the eddying flow, the flow at a particular point in time minus the mean flow. As the marine geoid is not known accurately enough only anomalous measurements to some mean are made and the transient variability inferred. The measure of EKE is preferred to that of the *root mean square* of the residual SSH as it is a measure of the sea surface slope variability over eddy length scales as opposed to a point variation in SSH.

$$EKE = \frac{1}{2}(u'^2 + v'^2) \tag{3.1}$$

where u' is the eddy zonal flow and v' is the eddy meridional flow. We will use the measure of EKE to infer changes in the strength and position of the large scale circulation and to examine any trends in mesoscale activity over the study period. In the Subpolar North Atlantic Ocean typical background eddy length scales are of the order 10 km associated with the Rossby radii of mid-to-high latitudes and are not fully resolved by the altimeter. However, the eddy length scales associated with the baroclinic instabilities generated by the NAC are typically an order of magnitude larger allowing the SPF to be adequately resolved.

[11] Initially the data from individual satellite passes were filtered using a cubic spline technique with a 30 *km* interval so to reduce noise in the data. A series of splines, with a sequence of *knots* of uniform spacing and *weightings*, were used allowing greater control over the data that are being manipulated (see Appendix A.1 for more details). To derive residual current measurements or values of EKE from the residual SSH we require the slope of the surface. As the data are now represented by a series of polynomial functions their derivatives can be simply calculated. We derive the eddy flow from the residual SSH measurements via the geostrophic approximation. The geostrophic equation:

$$fv = \frac{1}{\rho}\frac{\partial \mathcal{P}}{\partial x} \tag{3.2}$$

where f is the coriolis parameter, v the geostrophic velocity, ρ the density and P the pressure, combined with the hydrostatic relation:

$$\frac{\partial \mathcal{P}}{\partial z} = -\rho g \tag{3.3}$$

where g is gravity, at the surface gives the geostrophic balance:

$$v = \frac{g}{f}\frac{\partial h}{\partial x} \tag{3.4}$$

and a measure of the eddy flow, where h is a perturbation in SSH.

[12] Using this technique we only resolve the residual geostrophic velocity measurement that is perpendicular to the satellite track. In this case the eddy field is assumed isotropic, thereby increasing the resolution of the data available. The zonal and meridional contributions to the EKE can be resolved via a geometric interpretation at crossover locations between ascending and descending satellite passes (Morrow *et al.*, 1994):

$$\mathbf{V}_{a'} = -u\cos\phi\hat{\imath} + v\sin\phi\hat{\jmath} \qquad \mathbf{V}_{d'} = -u\cos\phi\hat{\imath} - v\sin\phi\hat{\jmath} \tag{3.5}$$

$$u = \frac{\mathbf{V}_{a'} + \mathbf{V}_{a'}}{2\cos\phi} \qquad v = \frac{\mathbf{V}_{a'} - \mathbf{V}_{a'}}{2\sin\phi} \tag{3.6}$$

where $V_{a'}$ and $V_{b'}$ are the residual velocities perpendicular to the ascending and descending satellite tracks respectively; u and v are the zonal and meridional velocities and ϕ is the angle between a particular satellite track and the meridian (see Figure 3.1). This reveals a strong an-isotropic core to the NAC, but outside of this region the EKE becomes increasingly isotropic. As the resolution of crossover locations is relatively coarse and the

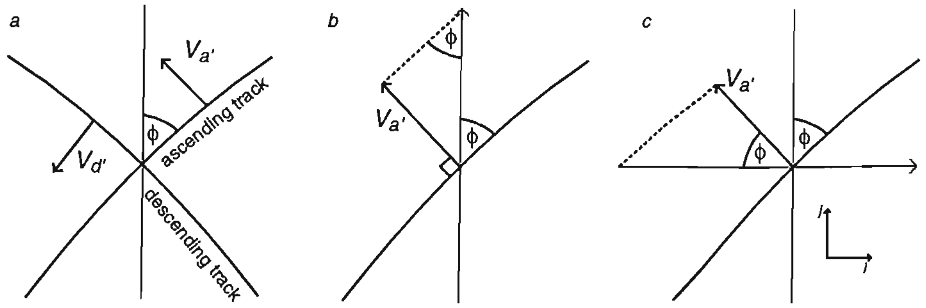

Figure 3.1: *a) Schematic of ascending and descending satellite passes at a crossover location. ϕ is the angle which the pass makes with the meridian at the crossover location and $\mathbf{V}_{a'}$ and $\mathbf{V}_{d'}$ are the residual velocities perpendicular to the respective ascending and descending passes. Velocity vectors are displaced from the crossover point for ease of reference. (b) and (c) illustrate the meridional and zonal component of $\mathbf{V}_{a'}$.*

geometric errors with increasing latitude are large, we will assume isotropy for the purpose of this study. Even with this assumption we are still including an an-isotropic component of EKE in gridding data from both ascending and descending tracks onto a 1°×1°grid. Finally, data were binned into monthly bins and any missing data of less than 1 month were linearly interpolated. In addition any location that was not continuous in time was discarded so as not to bias the time series in any way e.g. when comparing spatial averages in time.

3.4 Results

[13] As we would expect there are two distinct regions of eddy activity in the Subpolar North Atlantic Ocean. The first is associated with the major current system of the NAC and to a lesser extent with boundary current flows. The second, of lesser magnitude, is associated with local wind forcing. The mean EKE over the study period is presented in Figure 3.2, with the boundary between these two regions represented by the 0.02 m^2s^{-2} contour. Peak values of EKE, of the order 0.1 m^2s^{-2}, are observed in NAC, which are of comparable order of magnitude with values derived from drifter data (Frankignoul *et al.*, 2001). This relatively large signal decays eastward, past the MAR, into the eastern Subpolar North Atlantic Ocean. In general the contours of EKE are aligned with those of the bathymetry. The contrast between the relatively high EKE region of

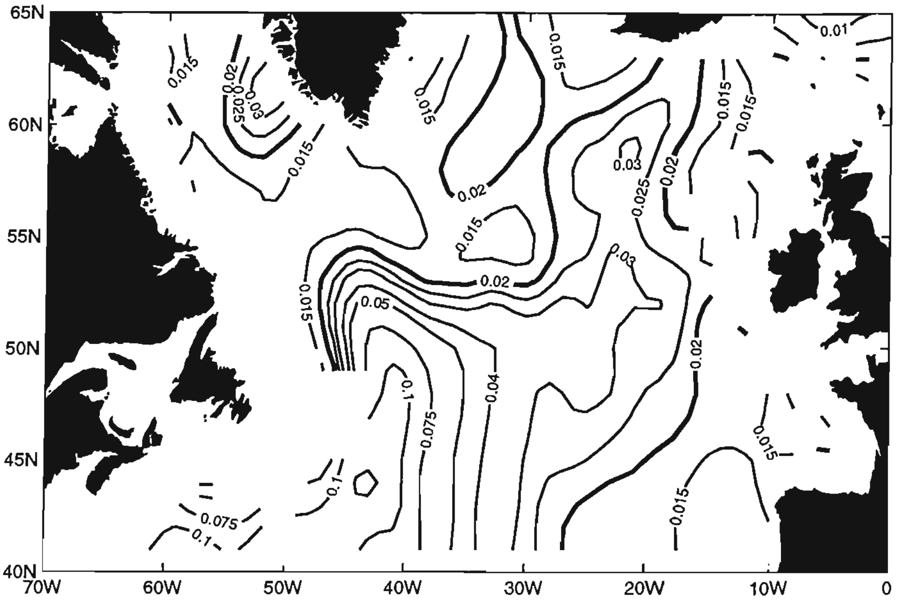

Figure 3.2: Map of mean eddy kinetic energy (m^2s^{-2}) computed for the period 1992 to 2001. *Eddy kinetic energy is contoured at irregular intervals with the thick black line (0.02 m^2s^{-2}) representing the typical boundary between background wind generated variability and that generated by the dynamic flow field. Light grey contours are those of the bathymetry.*

the NAC and the low EKE regions in the Subpolar Gyre gives a clear indication of the position of the SPF in the western Subpolar North Atlantic Ocean. The northern extent of the front tracks eastward from 53°N, 45°W into the Iceland Basin with a climatological mean position at the MAR close to the CGFZ at 52°N, 35°W. At around 25°W the region of relatively high mesoscale variability separates into two main branches. White and Heywood (1995) suggest that these branches characterise the northern and southern pathways of the NAC, one on the westward flank of the Hatton Bank the other following the topographic contours of the Rockall Trough towards the Nordic Seas. In the Irminger Basin there is also a region of elevated EKE on the western flank of the Reykjanes Ridge of the order of 0.03 m^2s^{-2}. The mechanism for this variability may be attributed to mixing between the relatively warm saline waters from the decaying NAC and the cooler fresher waters of the Irminger Basin. An increase in eddy activity along the western flank of the Reykjanes Ridge could also be attributed to the generation of barotropic instabilities in the Irminger Current, due to the presence of varying topography. Another notable area of enhanced variability is in the region where the West Greenland Current separates from the coastal shelf of Greenland into the central Labrador Basin. Prater (2002) suggest that eddies are generated close to the region where the 3000 m isobath diverges from the continental shelf. In contrast to these regions of elevated eddy activity, areas of relatively low EKE are observed in regions of elevated topography, e.g. plateaus and coastal shelves, and over the abyssal seas of the Subpolar Gyre.

3.4.1 Interannual variability

[14] The evolution of the EKE signal shown in Figure 3.3a reveals a high degree of variability on several time scales. The most notable being that of the annual cycle. On removing the annual cycle from the time series, there is still a large degree of high frequency variability, although there also appears to be degree of interannual variability. Figure 3.3b displays both the winter time EKE and NAO-index and clearly indicates the interannual variations in the eddy field and its correlation to the most dominant atmospheric mode of variability.

[15] The pronounced drop in the NAO-index over the winters of 1995/6 and 1997/8 coincide with the lowest observed EKE values over the Subpolar North Atlantic Ocean during the 1990s. Again, in the winter of 2000/1, a basin-wide reduction in the mesoscale activity is also observed corresponding to another drop in the NAO-index. Although the two time series exhibit a significant correlation, the result must be treated with caution as the number of degrees of freedom is small. Years that have a similar NAO-index values do not necessarily have similar levels of eddy activity. For example, although the NAO-index for the winters 1993/4, 1994/5 and 1998/9 are comparable, the mean EKE for the region during the winter of 1998/9 is greater than that of the other two winters. There are also notable differences between the winter of 1998/9 and 1999/2000. This may be, in part, as a result of the definition *winter-time*. If we included early spring in our definition of winter, the winters of 1994/5 and 1998/9 would in hindsight be of a comparable magnitude. To further identify changes in the eddy activity, correlation to the local wind forcing and the NAO and other physical mechanisms, a regional analysis of the Subpolar North Atlantic is undertaken. Seven regions in the Subpolar North Atlantic are defined, generally by basin, with the addition of two other regions of particular interest (Figure 3.4). The wind field data used in this analysis are the *reanalysis wind products* from the National Centers for

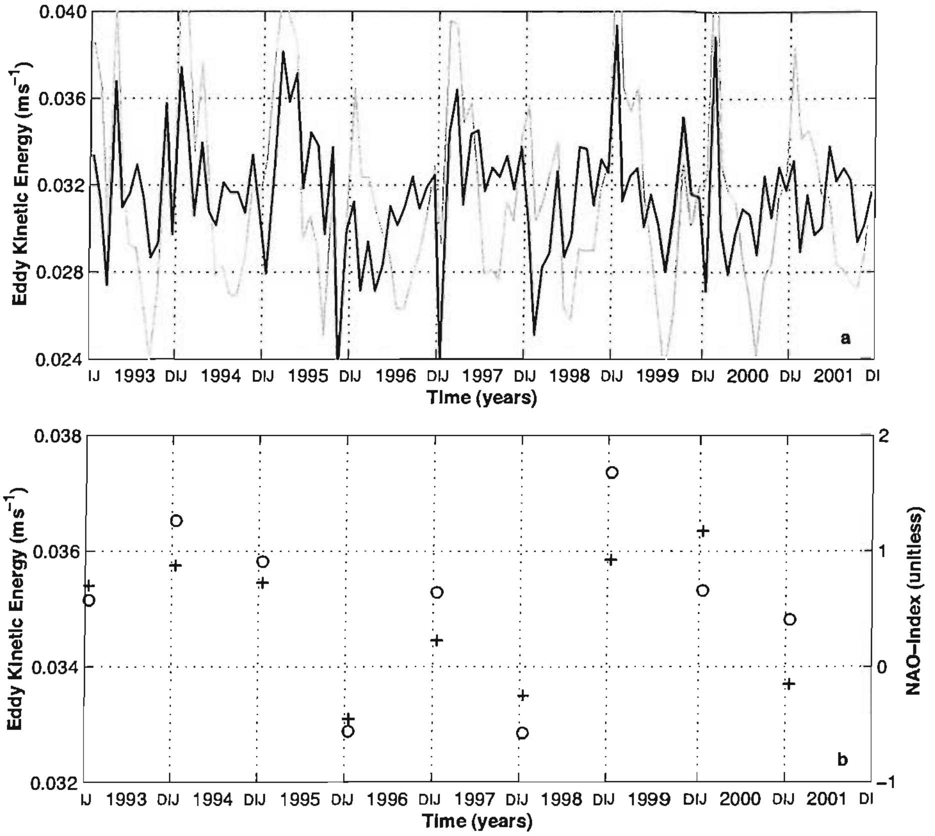

Figure 3.3: Time evolution of the mean eddy kinetic energy of the Subpolar North Atlantic Ocean (40°N to 65°N): *a) The first time-series indicated by the grey line includes the seasonal cycle; the second time series indicated by the black line has had the seasonal cycle removed. b) Comparison between the winter-time (JFM) eddy kinetic energy (circles) and the NCEP winter-time (JFM) NAO-index (crosses). The J and D on the x-axes signify the beginning and end of the year (January and December).*

Environmental Prediction (NCEP).

[16] Figure 3.6a displays the evolution of the eddy kinetic energy signal, with and without the seasonal cycle, for each of the seven regions identified in Figure 3.4. This illustrates the local changes in the eddy field that may otherwise be overlooked in a basin scale analysis. Overlaid on each sub-figure are the winter time means of both eddy kinetic energy and the NAO-index. What is immediately apparent, is that the eddy signal in regions within the Subpolar Gyre is weaker than to the south and is dominated by the seasonal cycle. Figure 3.6b shows the equivalent of Figure 3.6a, but for the NCEP monthly wind stress magnitude,

$$|\tau| = (\tau_x^2 + \tau_y^2)^{\frac{1}{2}},$$

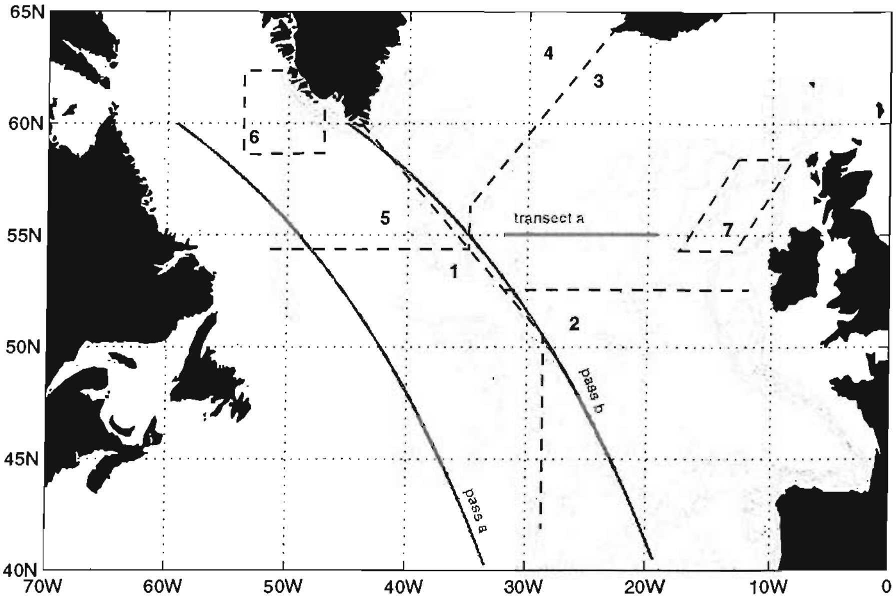

Figure 3.4: Seven regions of the Subpolar North Atlantic Ocean used to analyse the temporal evolution in eddy kinetic energy: *1) Newfoundland Basin, 2) Western European Basin, 3) Iceland Basin, 4) Irminger Basin, 5) Labrador Basin, 6) West Greenland Current Separation region and 7) Rockall Trough. Satellite passes a and b are the location of two satellite passes also used in this study. Transect a indicates the line taken to examine the variability in the Iceland Basin later in this section.*

for the period of the study. Again, each sub-figure shows the evolution of the wind field in a region of the North Atlantic sector, with and without the seasonal cycle. In this instance we remove the seasonal cycle by subtracting the individual monthly climatological anomalies from the time series, i.e. the January mean anomaly from each January in the study period *etc.* Over the following pages the presentation of the regional results is with reference to Figures 3.6a and b, unless otherwise stated. Reference will also be made to maps of the wind stress curl (Figure 3.5) and to regional correlations between the eddy activity and both the local wind stress and winter time NAO-index that are given in Table 3.1.

Region 1, Newfoundland Basin

[17] Over the study period there is ~ 16% decrease in the mean eddy kinetic energy found in the Newfoundland Basin. Baroclinic instabilities associated with the NAC are the predominant source of eddy activity in this region. Thus, the reduction in eddy kinetic energy indicates that the strength of the NAC has decreased during this period. Curry and McCartney (2001) suggest that fluctuations in the NAO would modulate the strength

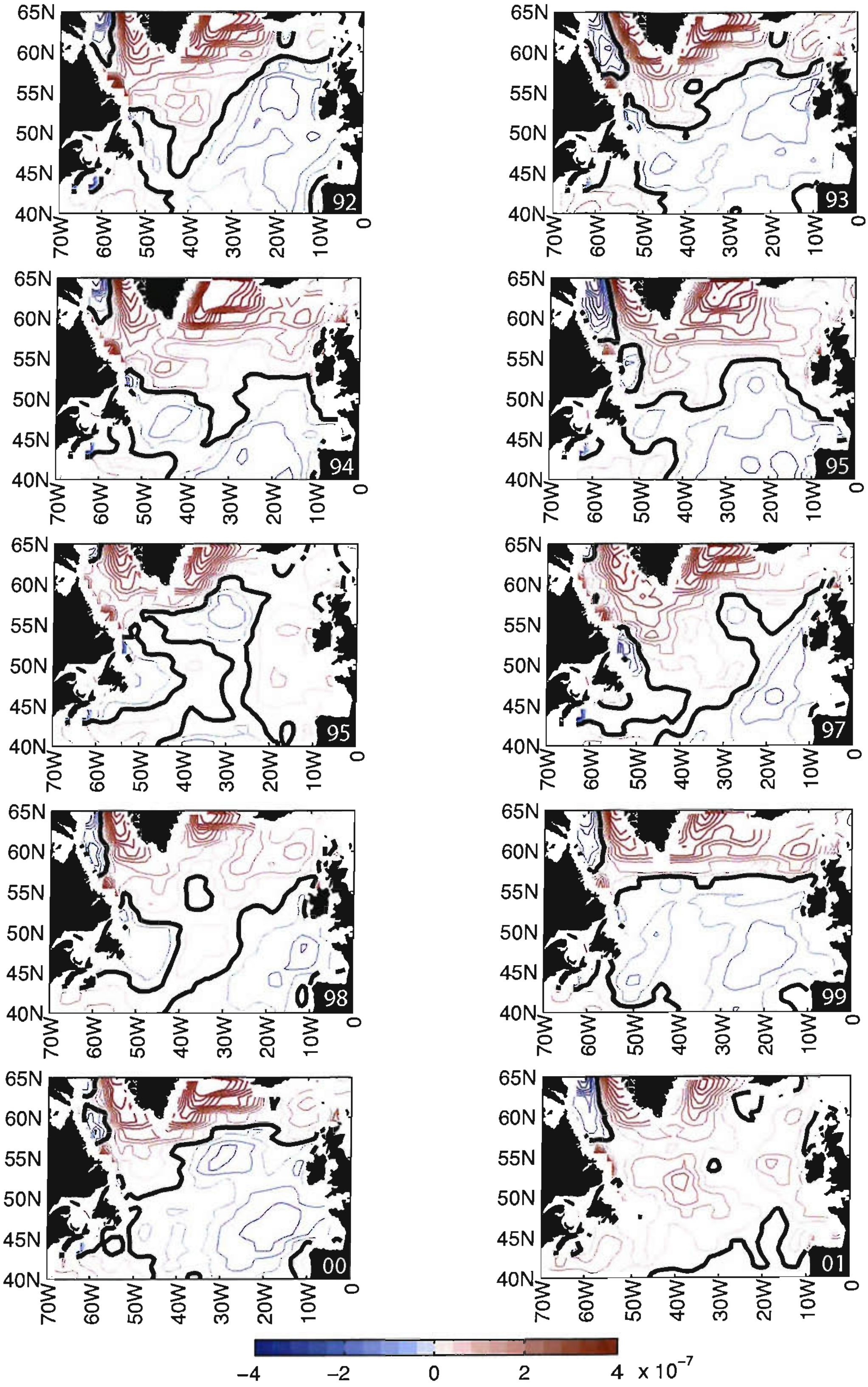

Figure 3.5: Winter-time wind stress curl maps for the period 1992-2001. *Units are in* Nm^{-3}. *The zero line in the wind stress curl is indicated by the thick black line.*

Region	NAO (95%=0.60)	$\lvert\tau\rvert$ (95%=0.19)
1) NEWFOUNDLAND	×	×
2) WESTERN EUROPEAN	×	×
3) ICELAND	0.83	0.33 (1-2)
4) IRMINGER	0.61	×
5) LABRADOR	0.75	0.28 (1-2)
6) WEST GREENLAND CURRENT SEP.	×	0.37 (2-3)
7) ROCKALL TROUGH	×	0.25 (13)

Table 3.1: Correlation between eddy kinetic energy and both the winter-time NAO-index and monthly wind stress (seasonal cycle removed) for each of the seven regions of the Subpolar North Atlantic illustrated in Figure 3.4. *The × indicates that there was no significant correlation (at 95%) between the two data sets. The values in parenthesis are an indication of the lag (in months) between the wind stress and the eddy kinetic energy.*

of the North Atlantic gyre circulation. They find that during periods of NAO$^+$ forcing the circulation in the North Atlantic Ocean intensifies and conversely for NAO$^-$ periods weakens. There was a sustained period of NAO$^+$ forcing during the late 1980s and early 1990s, which according to Curry and McCartney, would have strengthened the NAC. From the mid to late 1990s there was no such sustained forcing of any particular phase, but overall the phase was negative to neutral. This would imply a weakening of the NAC. Although this mechanism is qualitatively consistent with our time-series of eddy kinetic energy, we find no significant correlation between the winter-time eddy activity and that of the winter-time NAO-index. There is also no significant correlation with the wind stress suggesting that the strength of the NAC, to first order, varies on greater than annual time-scales.

Region 2, Western European Basin

[18] There is no significant correlation between the eddy activity and the winter-time NAO-index in the Western European Basin over the full length of the study. However, prior to the winter of 2000/1, we do find a significant correlation, of r=0.88, between the two time-series. During the winter of 2000/1 the eddy kinetic energy in this region is anomalously high. This increase may be, in part, due to a more southerly position in the zero of the wind stress curl during this period. The Sverdrup response of the ocean to the position of the zero in the wind stress curl in 2000/1 would be for the NAC to follow a more southerly trajectory across the MAR into the eastern North Atlantic. As

the observed pathway of the NAC in the eastern North Atlantic Ocean passes close to the boundary between region 2, the Western European Basin, and region 3, the Iceland Basin any displacement of the NAC southward will result in an increase of eddy activity in the Western European Basin. Further evidence for a southward shift in the NAC is presented later in this section.

Regions 3 & 7, Iceland Basin and Rockall Trough

[19] The region of the Iceland Basin is the focus of the winter-time storm track and as a result is one of the most significantly correlated regions to the local wind stress and the winter-time NAO-index. However, in the Rockall Trough region there is no significant correlation with the NAO-index. In an extended study of this region, Holliday *et al.* (2000) concluded that water mass modifications through local atmospheric interactions were not directly related to the NAO. It is unclear why this is the case as the Rockall Trough falls within the margins of the Iceland Basin.

Region 4, Irminger Basin

[20] There is no significant correlation between the eddy kinetic energy in the Irminger Basin and the overlying wind field, but there is, however, a weakly significant correlation to the winter-time NAO index. Eddy kinetic energy is generally weaker in the early 1990s compared to the period between 1997 and 2000 in this region. This may be associated with branches of the NAC turning northward along the Reykjanes Ridge in to the Irminger Sea before reaching the Iceland Basin, as suggested by previous hydrographic studies (Krauss, 1996, Schott *et al.*, 1999).

Regions 5 & 6, Labrador Basin and West Greenland Current Separation Region

[21] The eddy variability present in the West Greenland Current Separation region, region 6, appears to be different in nature to that of the surrounding Labrador Sea, region 5. The Labrador Sea is significantly correlated to the winter-time NAO-index, with a characteristic dip in EKE in the mid 1990s and again in 2001, whereas in the region of the West Greenland Separation there are significant departures from the mean in the winters of 1997/8 and again in 1998/9 with little correspondence to the NAO-index. EKE values in the West Greenland Current Separation region are also higher than those in the Labrador Sea. However, there is no significant difference between the magnitude of the local wind

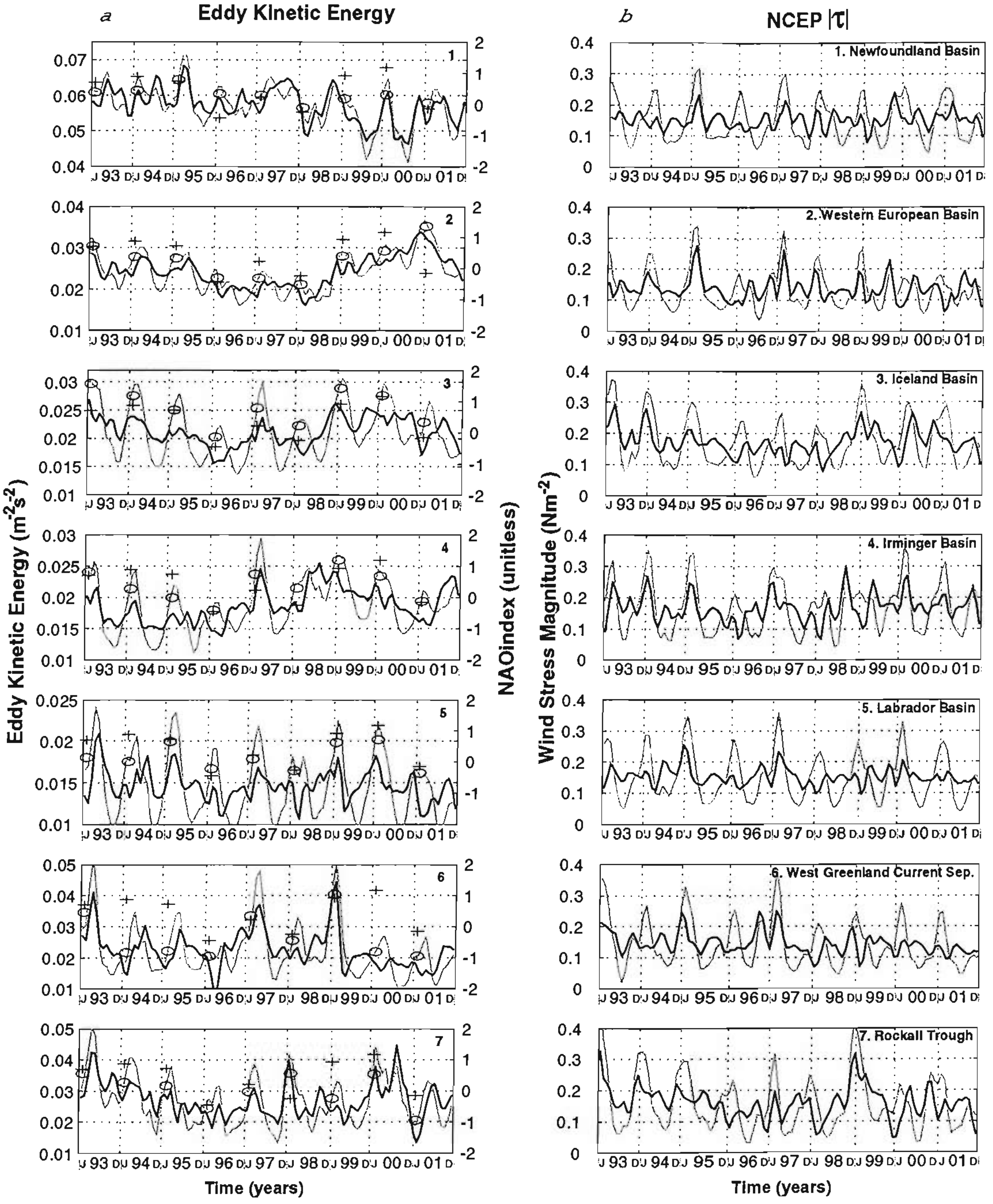

Figure 3.6: Time-series of *a)* the mean eddy kinetic energy and *b)* the wind stress magnitude for the seven regions of the Subpolar North Atlantic Ocean illustrated in Figure 3.4. *For each subplot, the first time-series indicated by the grey line includes the seasonal cycle and the second time-series indicated by the black line has had the seasonal cycle removed. The circles indicate the winter-time (JFM) eddy kinetic energy and the crosses the winter-time (JFM) NCEP NAO-index.*

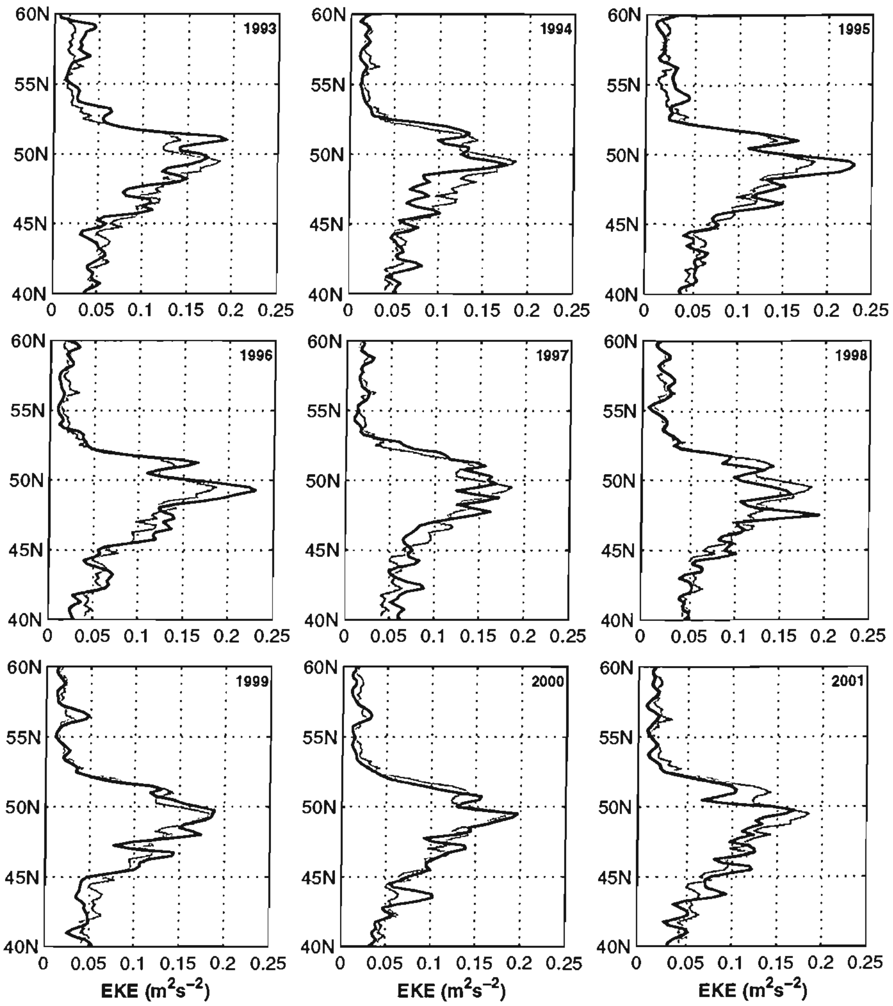

Figure 3.7: **Annual means of eddy kinetic energy along satellite** *pass a* (*see Figure 3.4*). *The black line is the annual average for the year indicated and the grey line is the climatological mean profile.*

forcing in each region (see Figure 3.6). This would suggest that the generation mechanism in each region is not the same. Both regions are, however, significantly correlated to the local wind stress, although the lag is somewhat greater in the West Greenland Current Separation region. What is more, the EKE signal in the Irminger Basin, region 4, is significantly correlated to that of the West Greenland Current Separation region, r=0.65, with a lag of 1 month. This suggest that there is a dynamic link between these two regions via the boundary current that follows the coastal shelf of Greenland.

Position of the North Atlantic Current

[22] To examine any changes in the position of the NAC and Subpolar Front we take two individual satellite passes and a transect at three locations in the Subpolar North Atlantic

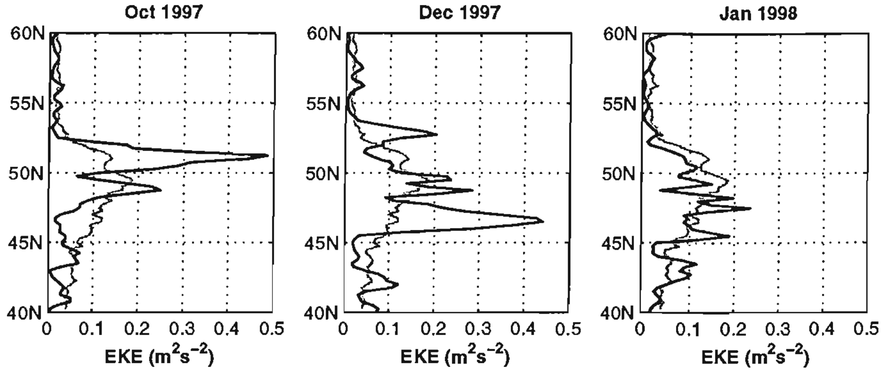

Figure 3.8: A series of snap-shots of monthly mean eddy kinetic energy along satellite *pass a* (*see Figure 3.4*). *The black line is the monthly average for the month and year indicated and the grey line is the climatological mean profile.*

(see Figure 3.4). *Pass a* provides a section across the *Northwest* Corner of the NAC, *pass b* a section across along the MAR and *transect a* a section across the Subpolar Front in the Iceland Basin. We have chosen to use individual satellite passes as the resolution of the gridded data may be too coarse to adequately resolve some features.

[23] Figure 3.7 shows the annual means of eddy kinetic energy along *pass a* through the *Northwest* Corner. Peaks in eddy activity in the climatological mean are observed at latitudes of 49°N and 51°N, similar to the locations of peak flow found from hydrographic surveys (Lazier, 1994). There is a clear front at ~ 52°N, separating the NAC from the Labrador Sea. To the south the eddy kinetic energy gradient is more shallow, encompassing the many tributaries of the eastward flowing NAC (Sy *et al.*, 1992, Belkin and Levitus, 1996, Reverdin *et al.*, 2003).

[24] Eddy energy appears to be focussed in a more northerly position in 1993 and 1994, suggesting a more defined character to the NAC, more so in 1994 where the southern gradient is also relatively sharp. In 1995 and 1996 we observed elevated peaks in mesoscale activity centred on 49°N, before the loss of definition and a southward shift in the maximum during 1997 and 1998. The years of 1999 and 2000 are characteristically similar to that of the climatological mean, whereas in 2001 the northward extent of the eddy kinetic energy front has somewhat diminished, with elevated mesoscale activity to the south. In general, the EKE front appears to be relatively invariant in its location at the *Northwest* Corner, unlike previous shifts in the pathway of the Gulf Stream (*cf.* Figure 2.6).

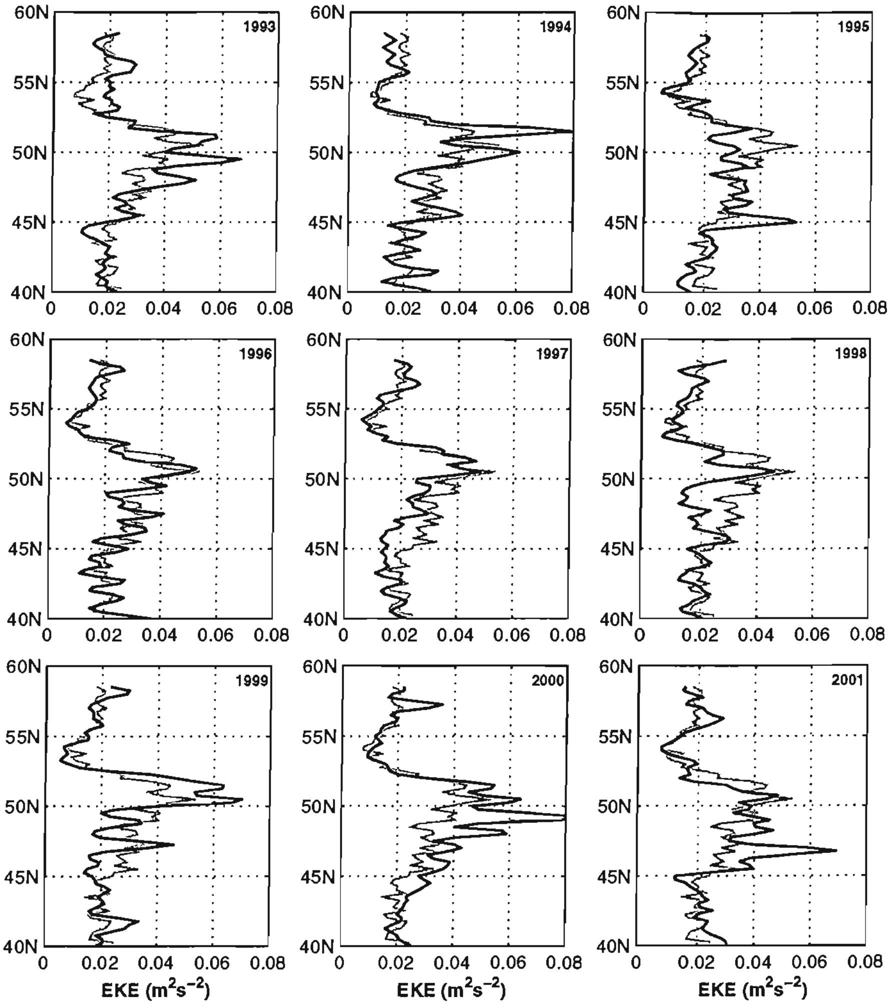

Figure 3.9: Annual means of eddy kinetic energy along satellite *pass b* (*see Figure 3.4*). *The black line is the annual average for the year indicated and the grey line is the climatological mean profile.*

[25] Although the annual averages do not vary much from the mean profile, if we examine a snap-shot of monthly means the high variability of the *Northwest* Corner, previously observed by Lazier (1994), becomes apparent (Figure 3.8). In the order of 5 months the eddy kinetic energy, hence NAC, has undergone a transition from two clearly defined peaks at 51°N and 48.5°N, to a relatively ill-defined series of smaller peaks spanning 45°N to 50°N.

[26] To the east of *pass a* a second satellite pass, *pass b*, is used to examine the latitude at which the NAC passes the MAR into the eastern North Atlantic Ocean (Figure 3.9). Unsurprisingly the mean eddy kinetic energy profile exhibits a cluster of peaks between 49°N and 52°N, over the Charlie Gibbs and Faraday Fracture Zones. Again, there is a

relatively sharp front to the north of the peak eddy kinetic energy and a shallower gradient to the south. There are no notable interannual excursions of the NAC to the north of this front, although there are periods where the NAC is more focussed and clearly defined, 1994 and 1997-1999. In 2001 the NAC is located to the south of the climatological mean position, with an elevated peak in energy at 46°N, associated with the Maxwell Fracture Zone. This would result in a larger fraction of the NAC entering region 2, the Western European Basin, explaining the anomalously high eddy activity in this region in 2001, as previously noted from Figure 3.6.

[27] The third section in this analysis, *transect a*, is taken across the Iceland Basin to identify any zonal shifts in the NAC and Subpolar Front, similar to those suggested by Bersch *et al.* (1999) from hydrographic data (Figure 3.10). As the magnitude of the eddy kinetic energy associated with the NAC is relatively weak in this region and the interannual variations in the wind generated mesoscale activity explain an increasing proportion of the signal, data are normalised at each Δt by their standard deviation. This step is performed to identify the maximum or *core* of the NACs northern branch.

[28] In the Iceland Basin we see a more coherent large-scale change than to the west. In a transect across 55°N we observed peak EKE associated with the NAC west of the Rockall Trough predominantly located between 22°W and 24°W between 1993 and 1996. From 1997 through to 1999 there is a migration of the SPF westward centred on 26°W, with less energy observed to the east of 23°W than in previous years. The peak eddy kinetic energy during this period appears relatively less well defined spanning a greater range of longitude. In 2000/1 the frontal region relaxes back towards 22°W.

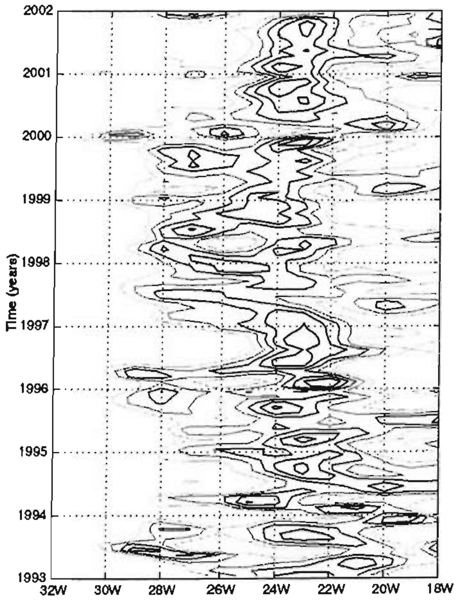

Figure 3.10: Normalised eddy kinetic energy time-series along 55°N in the Iceland Basin (see text for details). *Regions of peak eddy kinetic energy are contoured in black. Contours of lighter shades correspond to decreasing levels of eddy kinetic energy.*

3.4.2 Seasonal variability

[29] The local wind field has a direct impact on the eddy activity in the Subpolar Gyre region and is illustrated by the significant correlation between both time series. Table 3.2 gives an indication of the fraction of variability attributed to the annual cycle in each of the regions outlined in Figure 3.4. It is clear to see that where the NAC is most greatly defined, in the Newfoundland and Western European Basins, there is a relatively poor seasonal signal compared to those regions to the north. This re-enforces the idea that the contribution of the wind generated eddy activity is minimal in the locality of the NAC. This idea is further illustrated in Figure 3.11. The degree of seasonality in the eddy field is expressed as a percentage difference from the mean at various latitudes. The difference between winter/spring and summer/autumn increases with latitude, jumping markedly between 50°N and 55°N, the extent to which the NAC passes zonally from the north of the Flemish Cap in to the Iceland Basin. We also find that peak levels in eddy activity at 60°N occur later in the year than most other places. This is reflected in the phase of the annual harmonic of the West Greenland Current Separation Region, Table 3.2, with eddy kinetic energy values peaking in March.

[30] Figure 3.12 shows the mean eddy kinetic energy for each of the seasons. During the winter and spring months there is an extension of the eddy energy south eastward over the Western European Basin. To the north, eddy kinetic energy values increase in both the Iceland and Irminger Basins, extending the relatively high region of eddy activity over the

Region	**Amplitude** (%)	**Phase** (months)
1) NEWFOUNDLAND	8	1.50
2) WESTERN EUROPEAN	15	1.41
3) ICELAND	26	1.64
4) IRMINGER	23	1.52
5) LABRADOR	33	1.69
6) WEST GREENLAND CURRENT SEP.	37	2.24
7) ROCKALL TROUGH	28	2.44

Table 3.2: Amplitude and phase of the annual harmonic of eddy kinetic energy in each of the seven regions. *The amplitude of the annual harmonic is expressed as a percentage of the mean eddy kinetic energy for the associated region and the phase the number of months from the start of the calendar year.*

western half of the Subpolar Gyre. Eddy activity in the Subpolar Gyre is weakest during the summer months.

[31] A notable feature in the seasonal EKE maps is the apparent propagation of the elevated EKE signal in the West Greenland Current Separation region into the central Labrador Basin from winter to spring. There is also evidence of this feature in Figure 3.11 as the spring months have a higher percentage anomaly at around 60°N than those of winter and also in the phase of the annual harmonic in Table 3.2. The mechanism for the elevated mesoscale activity in this region is unclear. It is significantly correlated to the wind stress and has the greatest seasonal amplitude, but the values of EKE are greater than those in the surrounding regions.

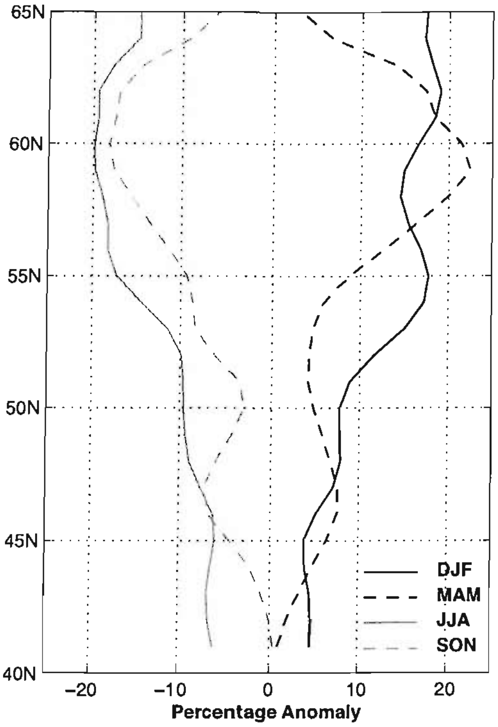

Figure 3.11: The seasonal eddy kinetic energy anomaly, expressed as a percentage of the zonally averaged (70°W to 0° annual mean eddy kinetic energy. *Winter (DJF) is the black solid line, spring (MAM) the black dashed line, summer (JJA) the grey solid line and autumn (SON) the grey dashed line.*

[32] In a similar analysis to examining the interannual changes in the position of the NAC we also examined seasonal changes in the position of the NAC, although the figures are not reproduced here. In general the position of the NAC is relatively unchanged from season to season. At the *Northwest* Corner the NAC does not significantly differ in strength or position from the climatological mean. Further to the east, along the MAR, the NAC is strongest during the winter months and also more defined at 52°N than any of the other seasons.

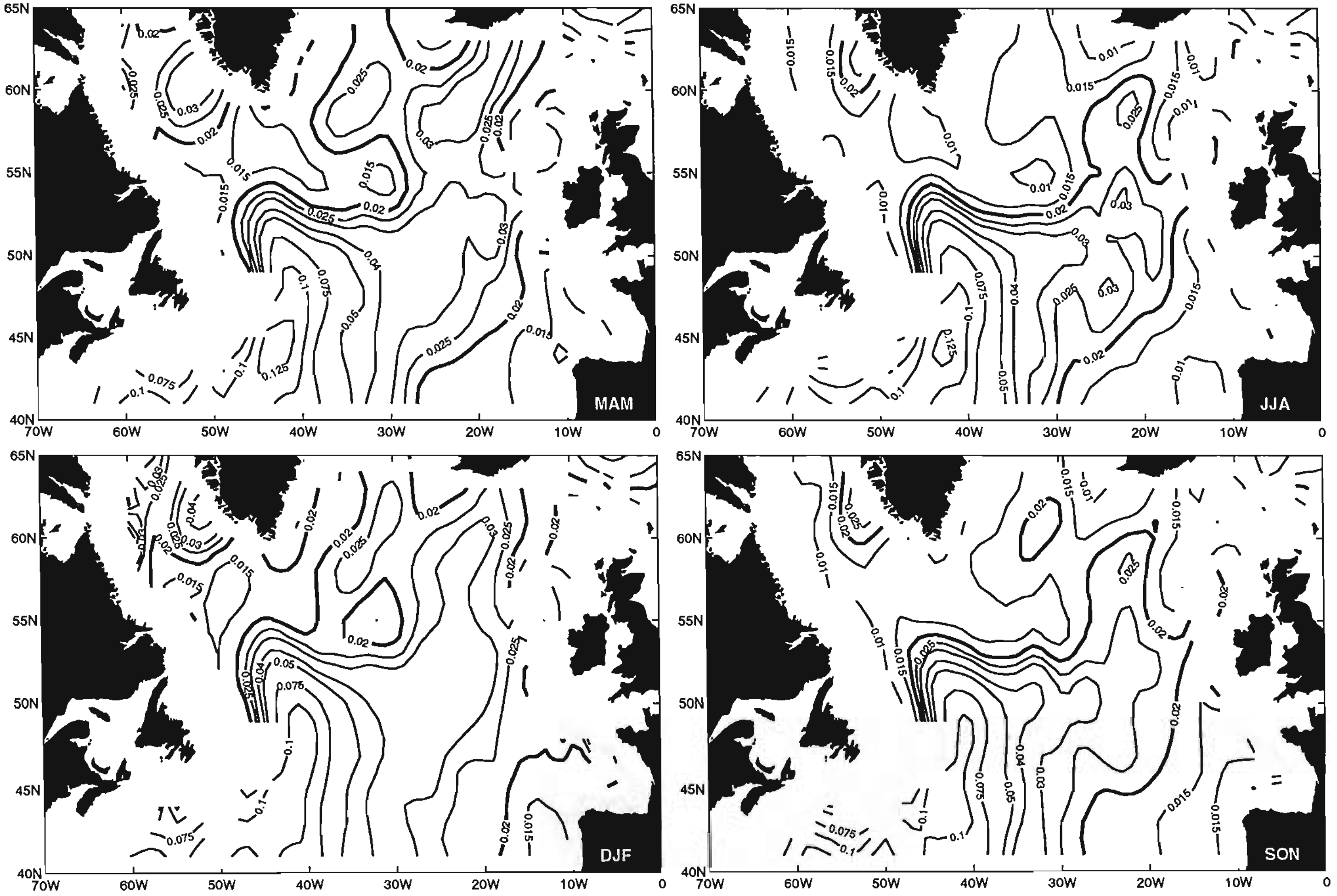

Figure 3.12: Map of mean eddy kinetic energy (m^2s^{-2}) computed for each of the four seasons (1992-2001). *Eddy kinetic energy is contoured at irregular intervals with a thicker line contoured at 0.02 m^2s^{-2}. Light grey contours are those of the bathymetry. Seasons rotate clockwise from winter (DJF) through to autumn (SON).*

3.5 Discussion of results

[33] It has been suggested that the decrease in NAC transport can be seen as a response to fluctuations in the NAO-index(Curry and McCartney, 2001). In a positive phase of the NAO the baroclinic pressure difference between the Subtropical and Subpolar gyres increases along with the transport in the Gulf Stream and NAC. An elevated heat flux from the ocean to the atmosphere, associated with the positive phase, will reduce the steric height in the Subpolar Gyre region and thus increase the pressure gradient across the gyre boundary. This change in the pressure gradient will act to increase the strength of the gyre circulation. In addition variations in the curl of the wind stress will also alter the transport in the NAC. The curl in the Subpolar region is generally weaker in a negative phase of the NAO, therefore reducing the northward Sverdrup transport. Additionally, the transport of the NAC may be influenced by deep and intermediate water production in the Labrador Sea. For example, during NAO^+ winters larger heat fluxes in the Labrador Sea will alter the density gradient along the Subpolar Front and increase the baroclinic transport associated with the northern branches of the NAC.

[34] Heywood *et al.* (1994) suggest that there had been distinct changes in the position of the northern branch of the NAC observed in the region of the MAR. They observe that in 1987 the northern branch appeared to be *tied* to the CGFZ at 52°N, while in 1988 and 1992/3 it appears in a more southerly position of 49°N to 50°N, respectively. In a follow up paper White and Heywood (1995), using T/P data, suggest that the northern extent of the NAC is located up to 52°N in 1992/3 retreating southward to 50°N in 1993/4.

[35] The differences between these two studies in the location of the NAC in 1992/3 may be associated with the sample time period chosen for the analysis. Heywood *et al.* (1994) used data from May 1992 to April 1993, whereas White and Heywood (1995) used the period October 1992 through to September 1993. We also find a strong peak in the northern branch of the NAC at 52°N during the period that White and Heywood (1995) sampled. However, for the period October 1993 to September 1994 we find no such southward shift of the NAC at the MAR. In fact the magnitude and position of the northern branch remains relatively unchanged with a southern peak in EKE moving northward from 49°N to 50°N during this period. In general we find that there is evidence of peaks in EKE spanning the latitudes of the Charlie Gibbs and Faraday Fracture Zones and occasionally

the Maxwell Fracture Zone, in agreement with previous surveys (Sy *et al.*, 1992, Bower *et al.*, 2002).

[36] The periods that the northern NAC appears to be most well defined at the MAR are observed in 1994, 1997 and 1999 (Figure 3.9). This result corresponds well to that of Schott *et al.* (1999) who observed an excursion of the NAC northward of its climatological mean in August 1997. Figure 3.13 shows the EKE profiles from the period of the Schott *et al.*'s hydrographic survey. The first profile of the *Northwest* Corner, illustrates an elevated peak in EKE north of the mean with the second profile, at the MAR, revealing a strong and well defined peak in EKE close to the mean location of the Subpolar Front. A year after the most extreme NAO$^-$ winter of the 1990s, 1995/6, we observe that relatively high values of EKE are confined predominantly to the region between 50°and 52°N during the period 1997 to 1999.

[37] There is little evidence to support the latitudinal dependence of the NAC on the NAO at the MAR or to the west. If the NAO was to be a proxy for variations in the branches of the NAC we would also expect to observe a contraction of the Subpolar Gyre in 2001. However, the most prominent peak in EKE during this period is located around 46°N at the MAR (Figure 3.9), the most southerly over the study period. This is also revealed in the elevated EKE observed in Western European Basin during this period (region 2; Figure. 3.6). The cause appears to be an elevated region of positive wind stress curl over the Iceland Basin, region 3, and further to the south over most of the Western European Basin, region 2.

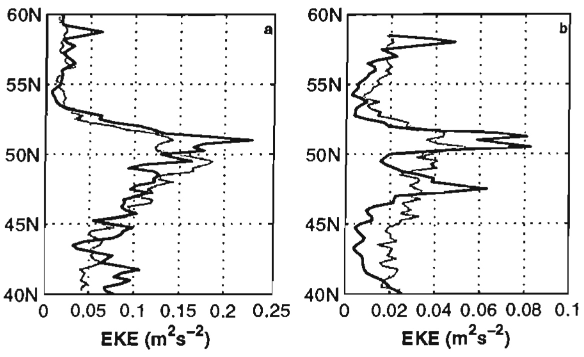

Figure 3.13: Eddy kinetic energy profiles during August 1997 along *a)* satellite *pass a* and *b)* satellite *pass b (black lines)*. *The climatological mean profile for each satellite pass is indicated by the grey line.*

[38] To the west of the MAR there is evidence of quasi-stationary features present along the path of the NAC (Kearns and Rossby, 1998, Kearns and Paldor, 2000, Reverdin *et al.*, 2003). Reverdin *et al.* (2003) also note that of the drifters that cross 44°N those east of

45°W experience a wider variety of trajectories. This is illustrated by the variable spatial nature of the EKE signature observed to the west of the MAR (Figures 3.7 and 3.8). The NAC crosses satellite *pass a* between 45°N and 52°N. North of 48°N there is evidence of two distinct branches at 49°N and 51°N with the eddy activity becoming increasingly variable to the south.

[39] In the Iceland Basin Bersch (2002) suggests that the Subpolar Front had shifted by $O(200\ km)$ westward during 1996/7, thereafter relaxing eastward towards its position prior to the NAO^- event of 1995/6. Evidence from this study confirms this westward shift in the front. Peak EKE values associated with the front are found to the west of the climatological mean in the Iceland Basin, persisting through to the beginning of 2000 before shifting eastward in 2001. White and Heywood (1995) suggest that the position of the Subpolar Front is governed by the position of the zero in the wind stress curl. The more northerly the position of the *zero* in the wind stress curl, the more westerly and northerly the Subpolar Front is in the Iceland Basin and along the MAR respectively. This would indeed explain the southward shift observed in 2001, but it is not so clear from our results whether the shifts in the Iceland Basin can be solely linked to the variations in the position of the zero of the wind stress curl.

[40] In West Greenland Current Separation region Prater (2002) observes relatively high eddy activity during the years 1993 and 1994 and relatively low activity during 1996 corresponding to highs and lows in the NAO-index. However, the eddy activity in 1995, NAO^+, is relatively low and in 1997, a NAO neutral year, there are relatively high levels of variability. With our extended time series we observe little correlation between the NAO-index and eddy activity off the western coastal shelf of Greenland. The NAO^- winter of 2000/1 exhibits low variability, which is similar to the NAO^+ winter of 1999/2000. White and Heywood (1995) interpreted the seasonality in the EKE signal in this region to be predominantly caused by the local wind-stress. The values of maximum EKE in this region are greater than those generated by local wind forcing in the surrounding Labrador Sea. A more likely mechanism is that variations in the eddy activity in the West Greenland Current Separation region are generated via instabilities in the seasonally varying boundary current (Fratantoni, 2002, Prater, 2002, Eden and Boning, 2002). A significant correlation between the EKE in the Irminger Basin and the West Greenland Separation region also suggests a possible dynamic link, via the boundary current, between

the two regions.

[41] Outside of the NAC the mesoscale activity is more seasonally varying, eddies being driven primarily by the wind. The Labrador and Iceland Basins are the most significantly correlated to the local wind-stress in the Subpolar region, which closely reflects the nature of the NAO. In contrast to estimates by White and Heywood (1995) that the annual amplitude of the EKE is 80% of the annual average in the Labrador and Rockall Trough regions, we observe the values to be only around 30% of the annual average.

3.6 Summary

[42] From our extended time series we have confirmed the significant shift of the Subpolar Front westward in the Iceland Basin in 1997 (Bersch *et al.*, 1999) and found that this shift persists through to and including 1999, before retreating eastward in 2000 and 2001. There is comparatively very little change in the position of the Subpolar Front in the western and central Subpolar North Atlantic Ocean, with the branches of the NAC apparently being constrained by topography at the MAR. However, we do observe a southerly shift in the position of the NAC during 2001. Although there is little change in the position of the NAC along the MAR, there are instances of a strengthening or focussing of the flow in the northern branch, particularly notable in 1994 and 1999. On seasonal time scales, the position and strength of the NAC in the western Subpolar North Atlantic is invariant. Further to the east we find no evidence to suggest seasonal variations in the position of the NAC, although we find that the strength is a maximum in winter.

[43] Over the time-series we suggest that there has been a reduction in the strength of the NAC associated with the decrease in EKE observed. There is also an excursion of the NAC southward across the MAR into the eastern Subpolar North Atlantic Ocean in 2001 in response to a more southerly position of zero in the wind-stress curl.

[44] The variations in the winter-time NAO-index are significantly correlated to eddy activity in the Subpolar North Atlantic Ocean north of 52°N. There is a notable dip in eddy kinetic energy during the NAO$^-$ winters of 1995/6 and again in 2000/1, associated with the reduced wind forcing. However, we find little correlation between eddy activity and the NAO in the topographically confined region of the Rockall Trough and in the West

Greenland Current Separation region. Generally, the ocean's response to the wind forcing is lagged by the order 1-2 months in the Subpolar Gyre and between 2 and 3 months in the Rockall Trough and West Greenland Separation region. However, the eddy activity associated with the West Greenland Current Separation region is thought to be primarily forced by seasonal fluctuations in the boundary current.

[45] With the increased coverage that will be gained through the recent launches of the ENVISAT and JASON satellite missions studies of this nature can become increasingly comprehensive. Improved measurements of the marine geoid coupled with combined altimetric products such as those outlined by Ducet *et al.* (2000) will allow better monitoring of the ocean circulation and its variability in the future.

Chapter 4

Variability as seen in two ocean general circulation models

4.1 Introduction

[1] A comparison of two global ocean circulation models will be presented in this chapter. The Ocean Circulation and Climate Advanced Model (OCCAM), eddy permitting, and the Estimating the Circulation and Climate of the Ocean (ECCO) model, coarse resolution, will be compared to observational data to evaluate how well each is performing in the Subpolar North Atlantic Ocean.

[2] Each model is validated against the WOCE repeat hydrographic section AR7E to examine the skill in reproducing the tracer distributions of the real ocean. A further independent data set from the FISHES hydrographic survey in May 2001 will be briefly compared with ECCO. A summary of the changes in the sea surface elevation observed in each of the models, with respect to altimeter measurements, is also presented. As the Labrador Sea is an important site for deep convection and hence the Meridional Overturning Circulation, the mixed layer depths in each model will also be evaluated. Differences in the large-scale circulation are also examined.

[3] In the forthcoming chapters ECCO will be exclusively employed to examine certain mechanisms for the variability observed like those described in Chapter 3. The inclusion of output from the eddy resolving model is purely as a bench mark from which to emphasize the choice of model for the remainder of the study.

4.2 The Models

4.2.1 The Ocean Circulation and Climate Advanced Model (OCCAM)

[4] Based on the Bryan-Cox-Semtner ocean general circulation model (Bryan, 1969, Semtner, 1974, Cox, 1984), OCCAM runs with a free surface and barotropic equations, allowing the surface layer thickness and salinity of the model to vary with advection, diffusion, evaporation and precipitation (Webb *et al.*, 1998).

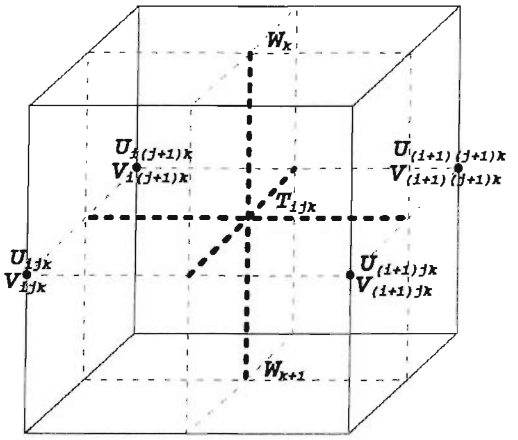

Figure 4.1: B-Grid configuration used in the OCCAM. *Velocity components are offset from the tracer locations by 0.5° longitude and latitude. The vertical velocity components are located at the boundary between grid boxes at the same longitude and latitude as the tracer coordinates.*

[5] The Levitus 82 (Levitus, 1982) global averaged data sets were used to initiate the first main model run from rest. During the initial four-year spin up period of the model, the advanced Levitus 94 (Levitus and Boyer, 1994, Levitus *et al.*, 1994) data sets became available and the model was subsequently relaxed towards these values. The total spin up phase lasted 8 years, although Webb *et al.* (1998) thought that this may be an insufficient period to obtain a realistic steady state eddy field. At the end of the spin up phase relaxation to Levitus potential temperature and salinity values over the water column was terminated.

[6] OCCAM is implemented on two Arakawa-B grids (Figure 4.1) of 0.25° resolution. The first is the *normal* grid and covers the Pacific, Indian and southern Atlantic Oceans. The second is the *rotated* grid covering the North Atlantic and Arctic Oceans. There are 36 levels in the vertical with greater resolution in the upper ocean (Table 4.1). The model depths used in OCCAM were derived from the US Navy DBDB5 data set.

[7] The specific model run used in this analysis is forced by ECMWF re-analysis winds for the period 1992 through to the end of 2000. The initial state of the model was taken as

Level	Tracer point depth (m)	Tracer box depth (m)	Level	Tracer point depth (m)	Tracer box depth (m)
1	9.87	20.00	19	1326.01	183.09
2	30.43	21.20	20	1515.91	196.29
3	52.35	22.75	21	1718.17	207.81
4	76.05	24.77	22	1931.09	217.60
5	102.04	27.37	23	2152.96	225.75
6	130.97	30.70	24	2382.21	232.40
7	163.67	34.94	25	2617.43	237.74
8	201.13	40.28	26	2857.42	241.99
9	244.55	46.92	27	3101.18	245.33
10	295.34	55.05	28	3347.89	247.93
11	355.07	64.84	29	3596.89	249.95
12	425.44	76.35	30	3847.67	251.51
13	508.18	89.53	31	4099.82	252.71
14	604.87	104.18	32	4353.01	253.63
15	716.83	119.95	33	4607.02	254.33
16	844.91	136.30	34	4861.63	254.87
17	989.42	152.66	35	5116.72	255.28
18	1150.09	168.43	36	5372.17	255.59

Table 4.1: List of tracer point depths and tracer box thickness for the OCCAM.

that of year 8 from the climatological run. A surface restoring to monthly averaged Levitus sea surface temperture and salinity climatology was also applied through the modification of the surface fluxes of heat and fresh water.

4.2.2 Estimating the Circulation and Climate of the Ocean (ECCO) model

[8] ECCO (Estimating the Circulation and Climate of the Ocean) is a consortium formed by a group of scientists at the Jet Propulsion Laboratory, the Massachusetts Institute of Technology (MIT) and the Scripps Institution of Oceanography. One of the goals of the ECCO group and of the World Ocean Circulation Experiment (WOCE) has been to estimate the global ocean state since the early 1990s through to the present day and beyond. ECCO is addressing this by attempting to constrain the MIT ocean circulation model (Marshall *et al.*, 1997) by assimilating a diverse range of ocean observations including

hydrographic, drifter and satellite measurements (Lu *et al.*, 2002).

[9] ECCO is configured globally with 1°x1° horizontal grid resolution over the latitudinal range of ± 80°. The topography implemented in ECCO comprises of the Smith and Sandwell (1997) (± 72°) and ETOPO5 (poleward of 72°) topographic data sets. Channels and sensitive topographic regions were manually edited to maintain realistic through flows. The vertical resolution of the model varies with depth, with a thickness of 10 m at the surface increasing to 500 m over 23 levels (Table 4.2). The tracer and velocity components of the model are distributed onto a staggered C-grid configuration (Arakawa and Lamb, 1977, Figure 4.2).

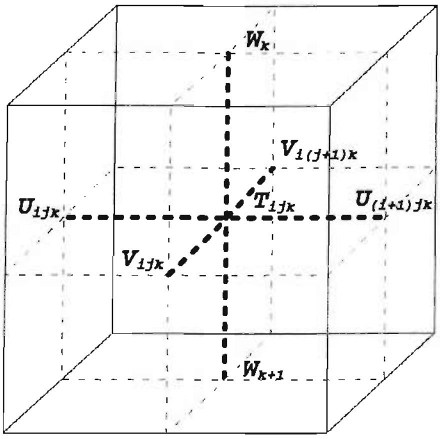

Figure 4.2: C-Grid configuration used in the ECCO model. *U and V velocity components are staggered by 0.5° of longitude and latitude, respectively, either side of the tracer location. The vertical velocity components are located at the boundary between grid boxes at the same longitude and latitude as the tracer coordinates.*

Level	Tracer point depth (m)	Tracer box depth (m)	Level	Tracer point depth (m)	Tracer box depth (m)
1	5.0	10	13	847.5	275
2	15.0	10	14	1160.0	350
3	27.5	15	15	1542.5	415
4	45.0	20	16	1975.0	450
5	65.0	20	17	2450.0	500
6	87.5	25	18	2950.0	500
7	117.5	35	19	3450.0	500
8	160.5	50	20	3950.0	500
9	222.5	75	21	4450.0	500
10	310.0	100	22	4950.0	500
11	435.0	150	23	5450.0	500
12	610	200			

Table 4.2: List of tracer point depths and tracer box thickness' for ECCO.

[10] ECCO was initialised from a previous 2° 50 year run and subsequently run for the period 1992 through to the end of 2001. National Center for Environmental Prediction (NCEP) and National Center for Atmospheric Research (NCAR) flux and wind stress products are used as prior forcing fields. In improving the state estimation these forcing fields are modified in the subsequent iterations of the model run.

4.3 Aspects of the horizontal circulation

4.3.1 Sea surface elevation

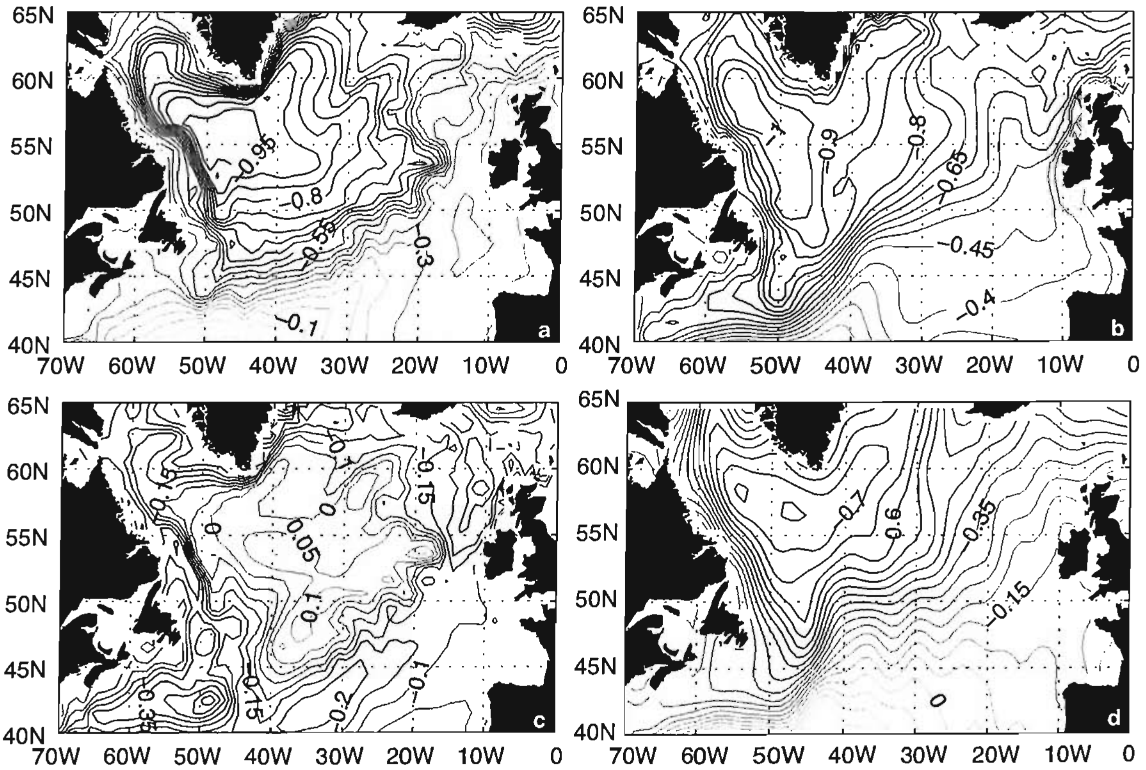

Figure 4.3: Sea surface height comparison between OCCAM and ECCO. *Mean sea surface height for the period 1993 to 2000 for a OCCAM, b ECCO. The difference between the model sea surface height fields (ECCO-OCCAM) is shown in c). Also shown is the absolute sea surface height from the GRACE (Gravity Recovery and Climate Experiment) mission, obtained at www.csr.utexas.edu/grace/gravity/ d). Contour intervals are given every 0.05 m.*

[11] The mean sea surface elevation in each model gives a reflection of geostrophic circulation. Generally, the two models have a similar sea surface topography with a minimum

in the Labrador Basin and relatively high gradient running from the Grand Banks of Newfoundland into the Iceland Basin associated with the NAC and Subpolar Front (Figures 4.3a and b). In level coordinate models it has been found that the trajectory of the NAC has a tendency to follow a more southerly pathway than observed (Willebrand *et al.*, 2001). ECCO, however, appears to represent the pathway a little more realistically. Figure 4.3c illustrates the difference between the two models. The positive anomaly in the central Subpolar North Atlantic Ocean indicates a more northward trajectory of the NAC in the western Subpolar North Atlantic Ocean present in ECCO. The sea surface height derived from satellite observations, shown in Figure 4.3d, clearly shows this type of feature in reality. The pathway of the NAC turns northward at around 40°N, 50°W, before following a more eastward pathway into the Iceland Basin at 50°N, 40°W, a little more northward than in ECCO.

[12] As we have previously seen from observations, there have been significant interannual variations in sea surface height in the Subpolar North Atlantic Ocean over the last decade (Figure 2.8). Here we illustrate how well each model is performing in relation to those observations. Figure 4.4 shows the evolution of the Sea Surface Height anomaly (SSHa) for the Subpolar Gyre region, defined between 50°N to 65°N and from 70°W to 0, for both models and the Topex/Poseidon satellite altimeter. The difference between the two models is quite apparent, the amplitude of the annual cycle is much larger in the OCCAM than in ECCO. As ECCO assimilates satellite altimeter data from both the Topex/Poseidon (T/P) and European Research Satellite missions, the comparison to the T/P SSHa is favorable, although not

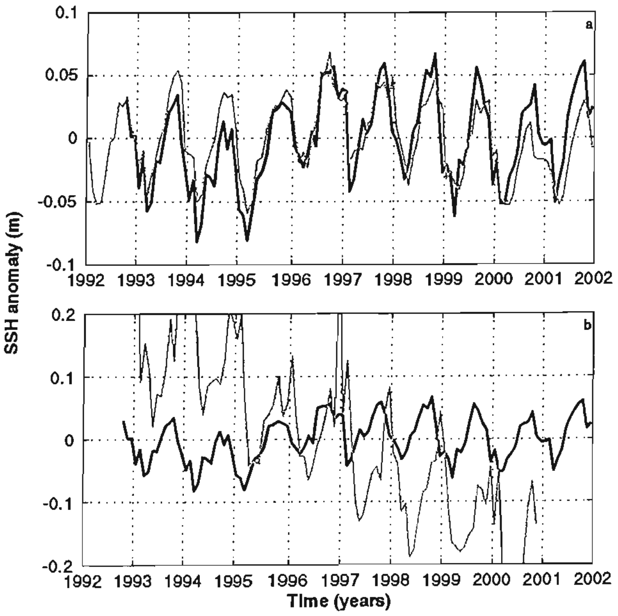

Figure 4.4: Evolution of sea surface height anomaly of the Subpolar Gyre region (50°N to 65°N) for *a)* ECCO and *b)* OCCAM, indicated by the grey line. *The black line in each subplot is that of the sea surface height anomaly from the Topex/Poseidon altimeter.*

identical. There is an increasing difference between the ECCO model solution and that of the observations. Between 1993 and 2002 the sea surface elevation in ECCO decreases by some 2 *cm*, whereas in the observations there is an increase of around 2 *cm*. The divergence of the two time-series occurs predominantly in the latter half of the model run. OCCAM on the other hand exhibits very little character of the observational data in addition to a notable trend in the sea surface elevation over the model run. In both ECCO and the T/P data there is an increase in the mean sea surface height of the Subpolar North Atlantic Ocean after the NAO$^-$ winter of 1995/6 as described by Reverdin *et al.* (1999). This increase is thought to be due to a combination of elevated oceanic heat transport and reduced ocean-to-atmosphere heat flux into the region, thus increasing the heat storage (Reverdin *et al.*, 1999, Esselborn and Eden, 2001).

[13] To investigate the changes in the sea surface height in ECCO, we can examine the heat transport into and out of the Subpolar North Atlantic Ocean (Figure 4.5a). Given the total heat transport:

$$ht_{net} = ht_{south} - ht_{east} - ht_{north} + ht_{west} - hf \qquad (4.1)$$

where ht is the heat transport by the ocean across each boundary of the Subpolar region and hf is the heat flux from the ocean to the atmosphere, we find differences between the total heat transport into and out of the Subpolar North Atlantic Ocean over the model run. The oceanic heat transport is simply calculated using the product of velocity, v, and potential temperature, T, integrated over the boundaries of an enclosed domain:

$$ht_{ocean} = \rho C_p \int_{-H}^{\eta} \int_{0}^{L} v(x,z)T(x,z)\,dz\,dx \qquad (4.2)$$

where C_p is the heat capacity of seawater and ρ is the density. The ocean-to-atmosphere heat flux is given as one of the model output variables. During periods where the NAO is in a negative phase, the mid 1990s and 2001, there is anomalously high oceanic heat transport and an anomalously low ocean-to-atmosphere heat flux. It is also noted that the total oceanic heat transport is similar to that of the Meridional Overturning strength at Subpolar latitudes (see Chapter 6).

[14] Integrating the oceanic heat transport and the heat flux to the atmosphere over time gives a measure of the total heat energy gained or lost by the Subpolar North Atlantic

Ocean over the model run (Figure 4.5 b). There is a marked jump in the oceanic heat gain between 1995 and 1996 corresponding to an increase of 0.8 GJm^{-2} over the Subpolar North Atlantic. This value agrees well with that from Esselborn and Eden (2001), who conducted a series of model experiments forced with idealised NAO-like forcing fields. Coupled with this oceanic heat gain by the upper ocean is an increase in the sea surface height of the Subpolar Gyre, which is evident in Figure 4.4, and has been previously documented using observational evidence by Reverdin *et al.* (1999). Similarly the conditions in 2001, an NAO$^-$ period, also result in a oceanic heat gain of approximately 0.4 GJm^{-2}.

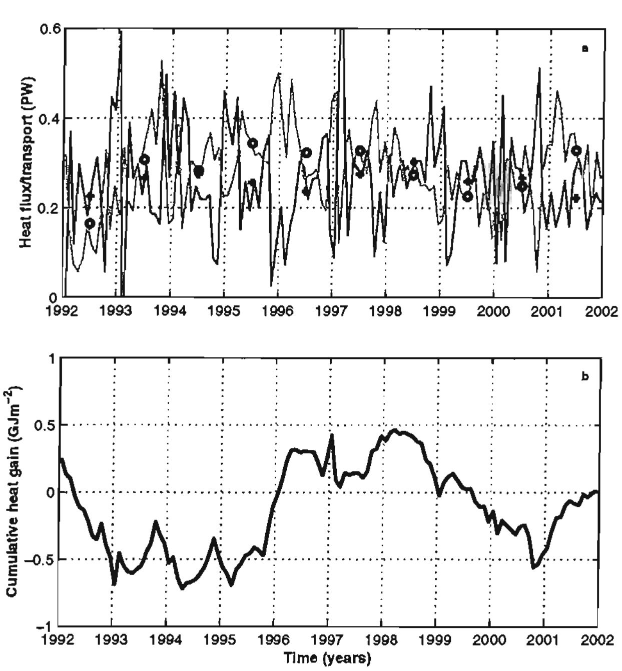

Figure 4.5: Changes in heat content in the Subpolar North Atlantic Ocean. *a) Heat transport into the Subpolar region by the ocean (light grey line). Heat flux to the atmosphere from the Subpolar region (dark grey line). Annual averages are also shown; heat transport (o) and heat flux (+). b) Cumulative heat gain over the model run .The seasonal cycle has been removed from the time-series.*

[15] By making the assumption that the expansion and contraction of the water column is purely a function of temperature, as the contribution from salinity and bottom pressure is minimal (Gill and Niiler, 1973), we can estimate the adjustment in the sea surface elevation associated with the observed heat gain.

[16] From the equation of state we can write the following:

$$\Delta h = \alpha H \Delta T \tag{4.3}$$

where H is the depth of the water column over which the expansion Δh occurs due to a change in temperature ΔT. The thermal expansion coefficient of seawater, α, is taken to be $1\times10^{-4}C^{-1}$. A linear relationship between *heat energy* and temperature is given by:

$$\Delta Q = mC_p\Delta T \tag{4.4}$$

where ΔQ is the heat energy gained (lost) by the mass of seawater, m, with an increase (decrease) in temperature, ΔT. The specific heat capacity of seawater $C_p \approx 4000JKg^{-1}C^{-1}$. In combining Equations 4.3 and 4.4, where $m = \rho H$ (ΔQ is units of GJm^{-2}), we arrive at an expression for the change in sea surface height in terms of energy gain or loss:

$$\Delta h = \alpha \frac{\Delta Q}{\rho C_p}. \tag{4.5}$$

This equates to approximately a 1 cm rise in sea level elevation of the Subpolar Gyre between 1993 and 2002 in the ECCO, which is close to that suggested by the observational data. The oceanic heat gain between 1995 and 1996 results in a rise in an average sea level rise of around 2 cm. The contribution to the sea level rise by the ocean heat transport corresponds to approximately 0.5 GJm^{-2}, whereas the atmospheric contribution is around 0.25 GJm^{-2}. In the following years the heat gained between 1995 and 1996 continues to be maintained as the heat transport and heat flux are of comparable value.

[17] In summary we find that ECCO achieves a more realistic sea surface height field than OCCAM. There is a notable change in the sea surface height in 1996 in ECCO, which can be explained largely by the heat gain in the Subpolar region. This heat gain results from an increase in the oceanic heat transport into the Subpolar region and a decrease in the heat flux to atmosphere. There is also a smaller heat gain in 2001 in response to the NAO$^-$ winter of 2000/1.

4.3.2 Changes in steric height

[18] The time varying component of sea surface height may be decomposed into three terms; upper and lower steric height and barotropic fluctuations (Stammer *et al.*, 1996):

$$\eta' = \underbrace{\eta'_{upper} + \eta'_{lower}}_{\text{baroclinic terms}} + \overbrace{\frac{1}{g\rho_0}P'_{bt}}^{\text{barotropic term}} . \tag{4.6}$$

While η'_{upper} and η'_{lower} are calculated from the model density field, the barotropic term is derived from the residual of η' once the first two terms have been subtracted. By examining these terms individually any inherent drift in the model may be identified. The upper layer steric anomaly is given by:

$$\eta'_{upper} = \frac{1}{\rho_0} \int_{-h}^{0} \rho'(z) dz \tag{4.7}$$

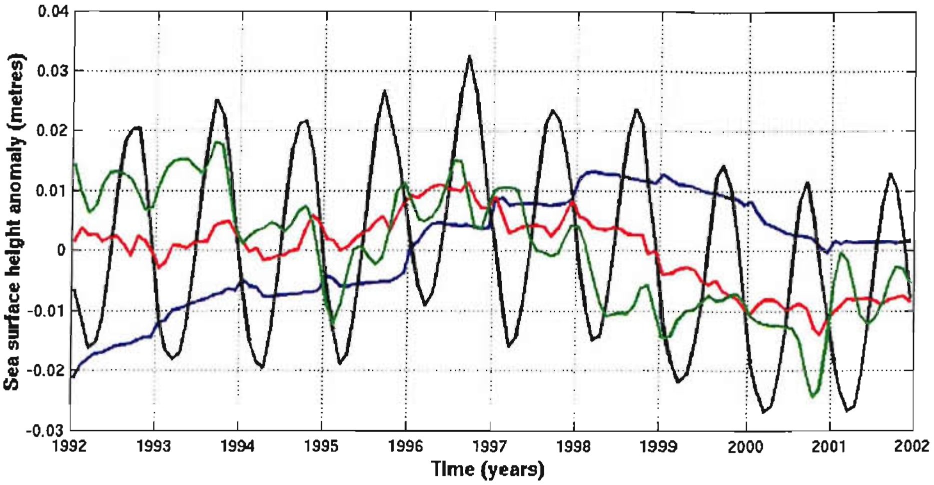

Figure 4.6: Changes in sea surface height through the upper steric height component (red), the lower steric height component (blue) and barotropic fluctuations (green). *Also shown is the actual sea surface height (black). The annual cycle has been removed from the upper steric height component.*

where h is the inferred base of the seasonal thermocline. In this instance h is taken to be the depth at which 5% of the seasonal harmonic amplitude in density is exceeded. The lower layer steric anomaly is given by:

$$\eta'_{lower} = \frac{1}{\rho_0} \int_{-H}^{-h} \rho'(z) dz \tag{4.8}$$

where H is the depth of the water column. As this term constitutes the bulk of the ocean it can give valuable insight into any drift in the model, whereas the upper layer steric anomaly is primarily forced by the seasonally varying atmospheric heat flux. The contribution of each term to the sea surface height is illustrated in Figure 4.6. There appear to be systematic drifts in all three components. In addition we observe the characteristic increase in steric height in the upper ocean during the mid 1990s associated with a switch in phase of the NAO as mentioned in the previous Section.

[19] Variations in the lower steric component of the sea surface height are associated with fluctuations in Ekman pumping and advection by barotropic currents (Stammer *et al.*, 1996). The trend observed in Figure 4.6 in the lower steric height does not appear to be linked to trends in the wind forcing and therefore must be in part a function of anomalous advection of density anomalies into the region. The upper steric height change, on the other hand, is dominated by the annual cycle $O(4\ cm)$. However, once the annual cycle

is removed a longer term trend emerges of approximately half the magnitude of the lower steric component. This change in the upper steric component occurs over the last three years of the model run. The trends in these components also have very different spatial patterns and will be elaborated on in the following chapter.

4.3.3 Horizontal transport

[20] The horizontal or *barotropic* streamfunction is defined as

$$\Psi_{bt}(x,y) = \int_0^L \int_{-H}^{\eta} v(x,y,z)dxdz \tag{4.9}$$

where v is the velocity, H is the depth of the ocean, η the sea surface height and L is the width of the Basin. Figures 4.7a and 4.8a illustrate the mean horizontal streamfunctions for OCCAM and ECCO, respectively. The temporal evolution of the streamfunction is determined by performing an EOF analysis on each data set, which *includes* the time-mean (Figures 4.7b and 4.8b). This allows a measure of the total field whereas a single point time series will be biased towards the local variability.

[21] Both models have a well-developed Subpolar Gyre, although the overall horizontal circulation patterns differ in their appearance and strength. The maximum transport in OCCAM is of the $O(35\ Sv)$, whereas in ECCO is significantly weaker, $O(23\ Sv)$. There is a decrease in the strength of the Subpolar Gyre over the course of each model run, more so in ECCO. However, it is unclear whether this drift is climatic or simply an artifact of the

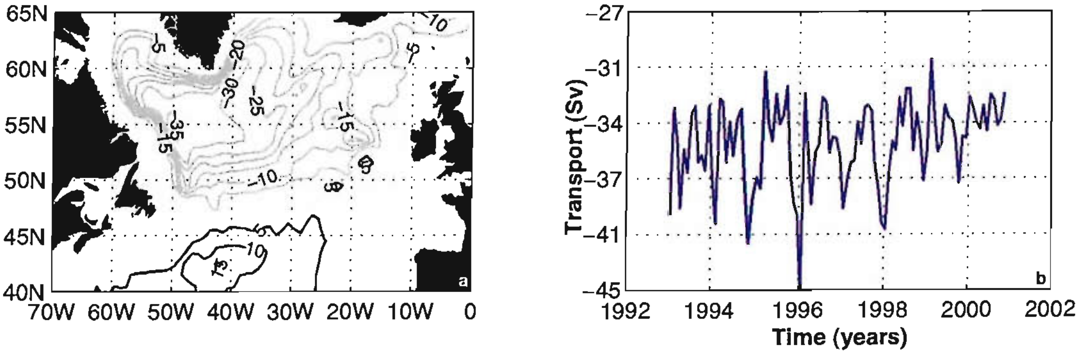

Figure 4.7: *a) OCCAM horizontal streamfunction contoured every 5 Sv, grey contours indicate a cyclonic circulation and black an anti-cyclonic circulation. b) The first Principal Component of the horizontal streamfunction representing the time evolution of the transport strength around the Subpolar North Atlantic Ocean.*

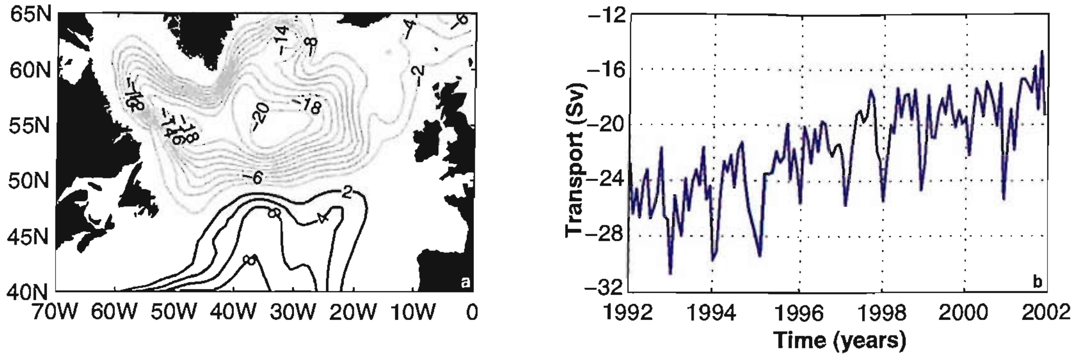

Figure 4.8: *a) ECCO model horizontal streamfunction contoured every 2 Sv, grey contours indicate a cyclonic circulation and black an anti-cyclonic circulation. b) The first Principal Component of the horizontal streamfunction representing the time evolution of the transport strength around the Subpolar North Atlantic Ocean.*

model. Over the same period there appears to be no associated trend in the strength of the wind stress curl over the Subpolar region, which would have led to a reduction in the northward Sverdrup transport and spin down of the gyre. This feature of the circulation will be examined in further detail in the following chapter.

4.4 Mixed layer depths

[22] Reproducing realistic mixed layer depths in the model is important in the role of the overturning circulation. It has been demonstrated by Spall and Pickart (2001) that most of the sinking in the ocean occurs in regions where the mixed layer is in the vicinity of topography. It is thought that there are only a hand full of locations where the conditions are favorable for deep convection to occur; the Labrador and Irminger Seas are two such sites in the Subpolar region (Pickart *et al.*, 2003).

[23] Each winter the stratification in the Labrador Sea is eroded by the large ocean-to-atmosphere heat flux over the region. Convective overturning has been observed to produce deep winter mixed layers to depths of 2000 m in the early 1990s (Marshall *et al.*, 1998). In the winter of 1994/5 Lilly *et al.* (1999) observed localised mixed layer depths of around 1750 m from hydrographic measurements. In the following winter of 1995/6 there was insufficient heat loss from the ocean to bring about deep convection and a mixed layer to depths of previous winters. The *memory* of the Labrador Sea allowed limited,

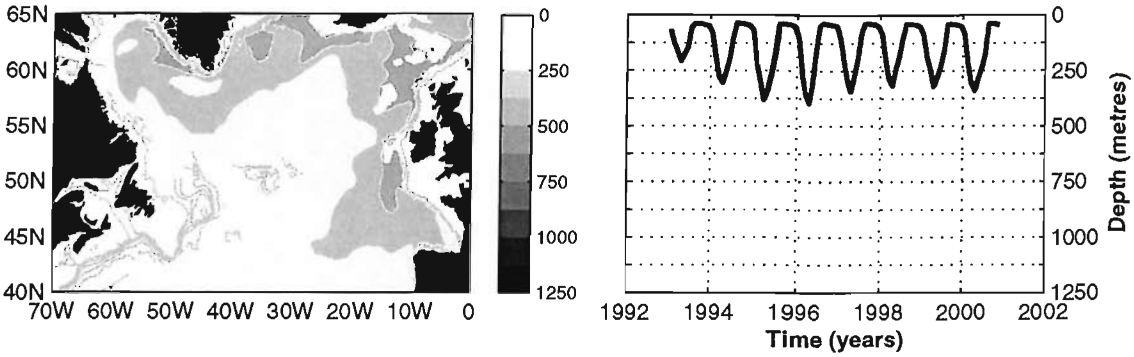

Figure 4.9: Spatial map of the mean winter-time mixed layer depths in OCCAM (*left*) and a time-series of the mixed layer depth in the Labrador Sea (*right*). *Mixed layer depths were calculated using the criterion of a density change corresponding to a change in temperature of 0.8° C (Kara* et al.*, 2000).*

but relatively high forcing in the winter of 1996/7, to produce mixed layer depths of up to 1500 *m* and initialise convection (Pickart *et al.*, 2002). However, in the proceeding winter Lavender *et al.* (2000) suggest that winter mixed layers were not as deep; Marshall *et al.* (1998) estimated mixed layer depths of no more than 600 *m* during this winter.

[24] Figure 4.9a illustrates the typical mixed layer depths in March for OCCAM. The time evolution of the mixed layer depth in the Labrador Sea, shown in Figure 4.9b, highlights the relatively shallow mixed layer depths observed over the model run. This shortcoming is primarily due to the exclusion of mixed layer physics from the model. The lack of convective overturning will impact on the nature of the intermediate water masses in the Subpolar Gyre, which may have implications for the circulation characteristics observed.

[25] Mixed layer depths reproduced in ECCO, that includes *kpp* mixed layer physics (Large *et al.*, 1994), appear to reflect the magnitude of current observations. Deepest mixed layer depths are present in the Labrador Sea and also in part in the Irminger Sea, with a shallowing to the south and east (Figure 4.10a). A time-series of the mixed layer depths in the Labrador Basin reveals strong interannual variability (Figure 4.10b), although it appears that the model system does not possess the memory illustrated by the observational data in 1997. Maximum vertical velocities observed in ECCO are between 55.5°N and 57.5°W and 56.5°N and 58.5°W, southwest of the maximum mixed layer depths and along the topographic slope off the coast of Greenland consistent with the sinking mechanism

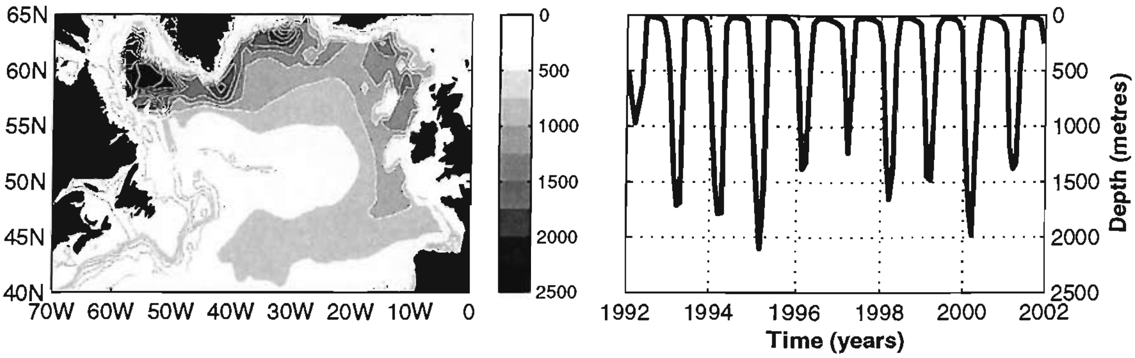

Figure 4.10: Spatial map of the winter-time mixed layer depths in ECCO (*left*) and a time-series of the mixed layer depth in the Labrador Sea (*right*). *Note the scale is double that of the one used in Figure 4.9.*

proposed by Spall and Pickart (2001).

[26] In general, Marshall *et al.* (1998) speculate that a higher heat flux to the atmosphere will occur during a NAO^+ and a lower heat flux in a NAO^-. This appears to hold true in ECCO. During the winters of 1995/6, 1996/7 and 2000/1 the shallowest mixed layers are observed corresponding to a low NAO-index and reduced convective overturning of the water column. However, in the first year of the model run the mixed layer depth is uncharacteristically shallow.

4.5 Comparison with hydrography

4.5.1 Introduction

[27] In this section we will examine the realism of each model by comparing the output with that taken from recent hydrographic surveys. Although the ECCO model assimilates all WOCE hydrographic data in providing an ocean state estimation, we will be using data for the repeat hydrographic line WOCE AR7E. There is very little independent *repeat* hydrographic data to compare with the ECCO model in this region as it assimilates nearly all data available. To this end, the comparison will be a measure of how well the assimilation process is working.

[28] The WOCE AR7E transect is a key section as it illustrates the recent shifts in the

Subpolar Front over the last decade (Bersch, 2002). The ability of each model will be assessed in reproducing water mass characteristics of Subtropical and Subpolar origin and on the temporal variability observed in the frontal location. In addition *independent* hydrographic data from the FISHES hydrographic survey that was carried out in 2001 is used to compare the ECCO model only as there is no output from the OCCAM for this period.

4.5.2 Data

[29] Hydrographic data are taken from the WOCE AR7E repeat survey line across the Iceland and Irminger Basins. The WOCE, a global oceanographic experiment spanning the last decade, was the basis for several of these repeat hydrographic surveys in the Subpolar North Atlantic Ocean. The WOCE AR7E line stretches from southern Ireland to Cape Farewell at the southern tip of Greenland (Figure 4.11) and was repeated on 9 occasions between 1990 and 1992 and 1994 and 1997. The resolution of the hydrographic data is of the order 40 *km* in the horizontal and every 2 *m* in the vertical. To allow comparisons to be made with the two model data sets the hydrographic data were linearly interpolated onto the tracer depths of each model. Data from each model were extracted using the hydrographic longitude and latitude coordinates by linearly interpolating the four closest tracer values onto the station location.

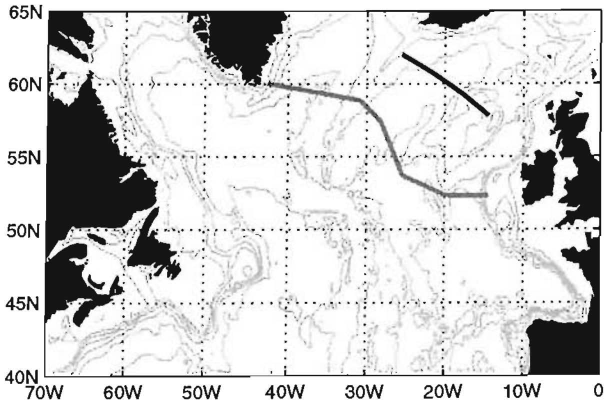

Figure 4.11: WOCE AR7E repeat hydrographic line (grey) and one-time FISHES hydrographic section (black).

[30] The FISHES survey took place in May 2001 sampling a series of hydrographic lines in the northern Iceland Basin. Here we take the most southerly hydrographic line, illustrated in Figure 4.11, to evaluate the ECCO model against.

4.5.3 Water mass distribution

WOCE AR7E hydrographic data

[31] Previous analyses of these data have been done by Bersch *et al.* (1999) and Bersch (2002). They found that there was a *redistribution* of water masses in the Subpolar North Atlantic Ocean in response to the *drastic* drop in the NAO-index. Bersch (2002) suggests that there was an immediate retreat of the Subpolar Front westward in the Iceland Basin after this drop, with a 2 year lagged response of the Subpolar Front in the Irminger Basin. It is suggested that the shifts in the Subpolar Front resulted from the reduced eastward spreading of waters of Labrador Sea origin and the increased northward spreading of warm saline waters reaching to depths of 1200 *m*.

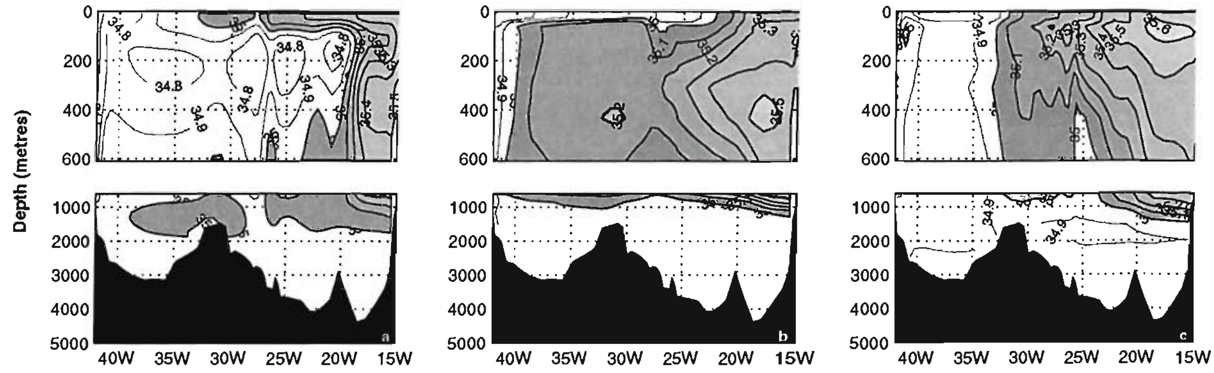

Figure 4.12: Salinity profiles along the 1997 WOCE AR7E hydrographic line for the a OCCAM, b ECCO model and c hydrographic data. *Shaded contours indicate salinity values great than 35.0. Data from the OCCAM and the hydrographic survey have been low-pass filtered in the horizontal with a 5-point hanning filter to reduce any mesoscale features present.*

[32] Figure 4.12 shows the salinity profiles along WOCE AR7E in 1997. The shaded region, of salinities greater than 35.0, gives an indication of the location of the Subpolar Front in each of the models and in the hydrographic data. OCCAM, as previously noted, has a more eastward flowing NAC, illustrated by the closely bunched contours to the east. ECCO on the other hand appears more characteristically similar to the hydrography. However, anomalously high salinities are observed west of the MAR in a more diffuse profile. In both the models the salinity maximum is some 300 *m* below that observed in reality.

[33] Figures 4.13 and 4.14 illustrate the skill of each model in reproducing the density

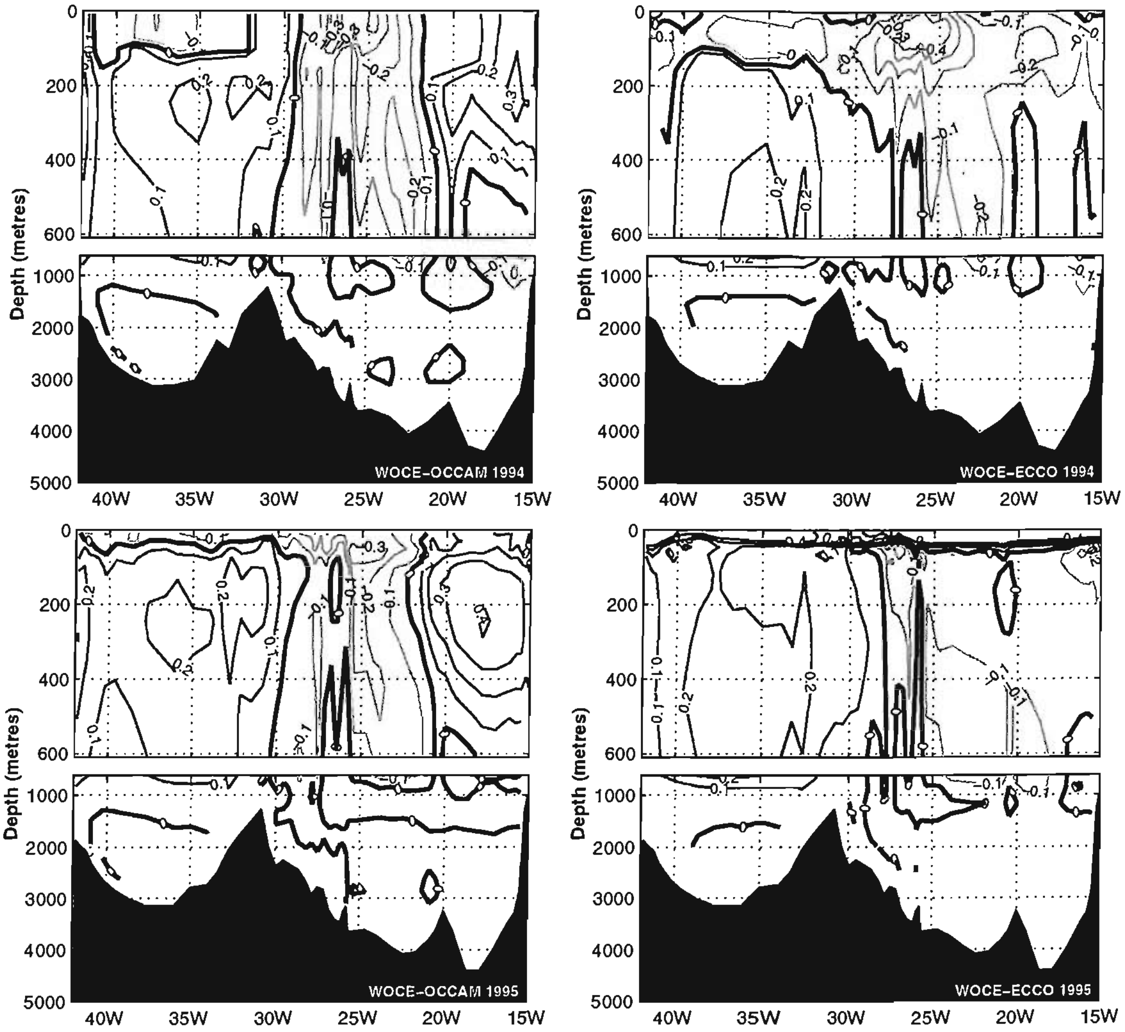

Figure 4.13: Density differences between hydrographic and model data for the various WOCE AR7E hydrographic surveys undertaken in the 1990s. *Grey contours signify that the model density is greater than that of the data and the black contours the reverse.*

structure found in four WOCE AR7E hydrographic surveys. Both models are unable to accurately reproduce observed densities in the upper 100 m of the water column. In the ECCO model this manifests itself as a tongue of relatively cold fresh water penetrating southward from the northern Iceland Basin across the AR7E transect. Subsurface, ECCO is doing considerably better job than OCCAM in the Iceland Basin with relatively little error in the density profile. A dipole structure in density difference exists east of 30°W in the OCCAM where the NAC is found to take a more eastward pathway through the Iceland Basin. Negative density anomalies between 30°W and 20°W in the OCCAM are due to the absence of warm saline water advected from the south. To the east of 20°W the waters in the OCCAM become anomalously warm, although salinity values remain

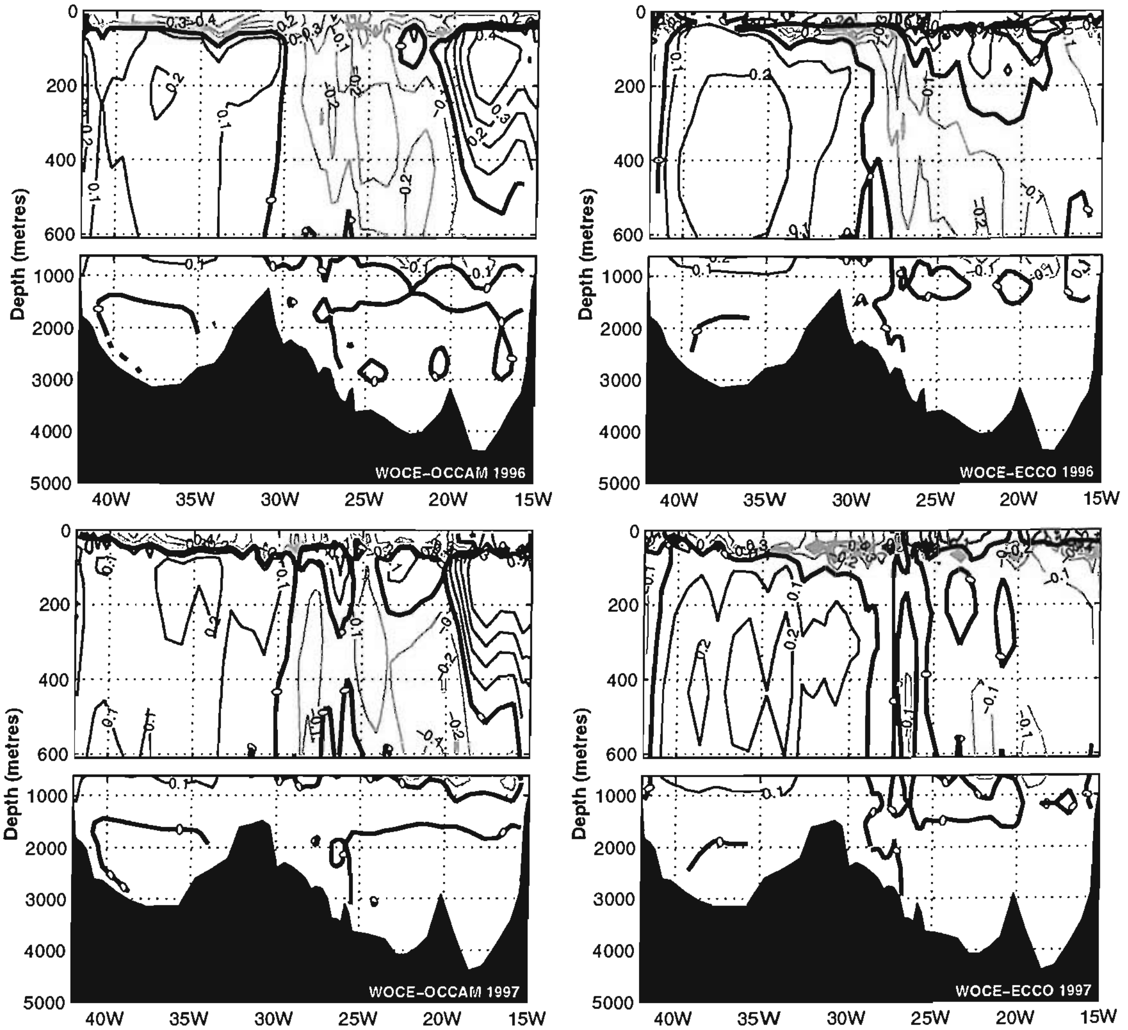

Figure 4.14: Density differences between hydrographic and model data for the various WOCE AR7E hydrographic surveys undertaken in the 1990s. *Grey contours signify that the model density is greater than that of the data and the black contours the reverse.*

less than observed.

[34] In the Irminger Basin the intermediate water masses are warmer and more saline than observed in the hydrography in the ECCO model, but less so in the OCCAM. In both models the temperature difference is the dominant factor, leading to anomalously light fluid in the intermediate ocean. At depth the density differences are minimal in both the Iceland and Irminger Basins in model, resulting from the low temporal variability.

[35] Even in the regions that density differences are small compared to the hydrography, the models have a deficiency in reproducing the required temperature and salinity characteristics. Figure 4.15 illustrates the change in temperature and salinity (*ts*) characteristics

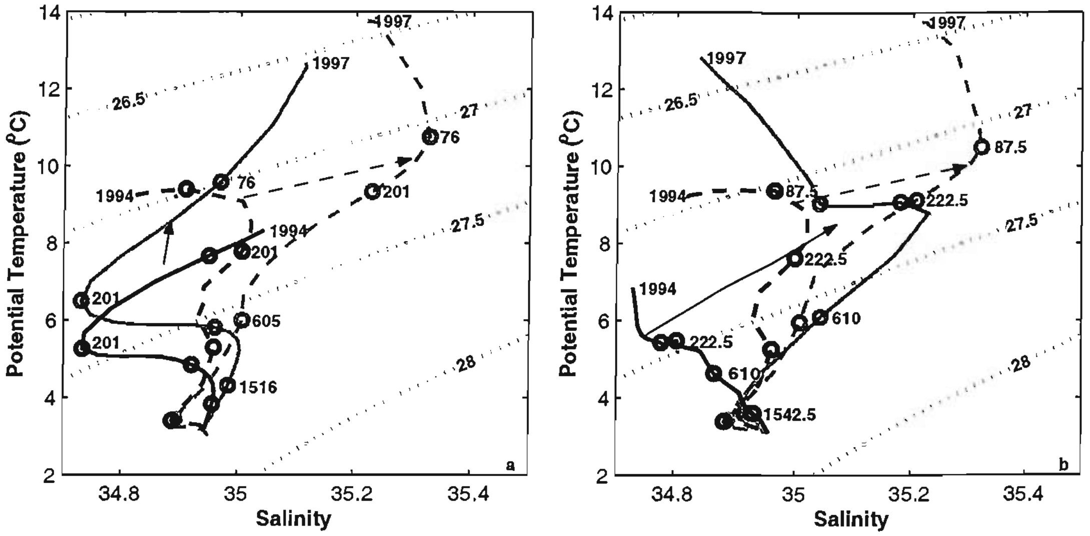

Figure 4.15: Temperature-salinity diagrams illustrating the temporal changes between 1994 (dark grey) and 1997 (light grey). *Hydrographic data are depicted by dashed lines and a OCCAM and b) ECCO by solid lines. Depth references (m) are given by the open circles.*

in the Iceland Basin between 1994 and 1997 (*cf.* Bersch, 2002). The translation of the *ts* curve of ECCO between 1994 and 1997 is somewhat similar in nature to that of the hydrography, in the sense that there is an increase in both temperature and salinity, whereas in OCCAM this is not the case. The water masses in the Iceland Basin in ECCO become increasingly warm and saline between 1994 and 1997, consistent with the additional advection of waters of Subtropical origin into the Iceland Basin from the south. In OCCAM the salinity of the water masses remains relatively constant with only a warming observed.

FISHES hydrographic data

[36] As we have previously mentioned the ECCO model assimilates a diverse range of observational data in obtaining an ocean state estimation. One of the data sets used in this process is that of the WOCE hydrographic surveys, so one would expect the model solution to be somewhat similar to that of the observation. For a further comparison, we will take data from the FISHES hydrographic survey that is independent of the model solution and compare the two.

[37] The hydrographic data are consistently warmer in the top 200 m of the ocean than the model, with a maximum difference at around 100 m over all longitudes of the $O(1°\text{C})$.

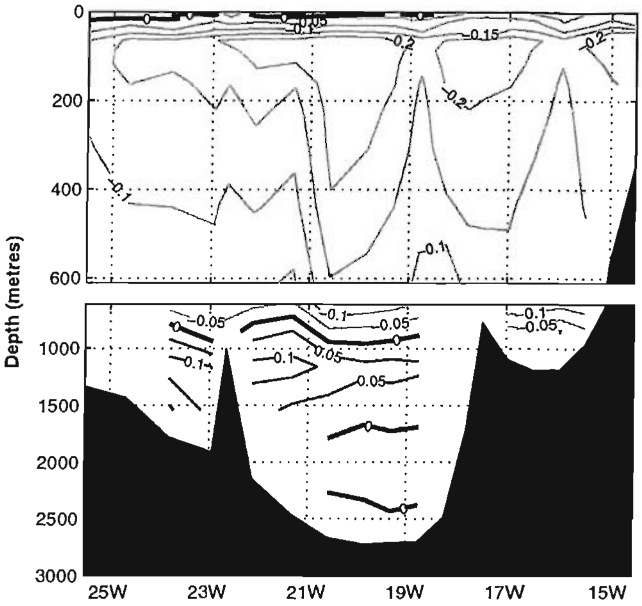

Figure 4.16: Density difference between the FISHES hydrographic data and output from the ECCO model. *Grey contours signify that the model density is greater than that of the data and the black contours the reverse.*

This is reflected in the density difference at this depth (Figure 4.16). Differences in salinity values remain relatively small, within 0.05. There is, however, anomalously low salinities in the model in the top 30 *m* to the west of 20°W indicated by the positive difference in density. Between the depths of 1000 *m* and 1500 *m* the model is too salty and too warm which may suggest that there is insufficient mixing between the upper and intermediate ocean. In the deep ocean there is relatively little difference between the observations and the model as one would expect with the model being initialised from a climatology and the variability at this depth relatively small.

4.5.4 Summary

[38] Both OCCAM and ECCO are unable to accurately reproduce temperature-salinity characteristics of the real ocean. There is a particular discrepancy in the surface layers of each model, with waters being generally too cold and fresh. As the model surface layers are typically only 5 grid points in depth, upper ocean mixing and Ekman processes in the models do not not fully resolve the character of the upper ocean. Krauss (1986) and Bersch *et al.* (1999) note, however, that the important depth range of 100 *m* to 600 *m*

is where we see the marked interannual changes that are unaffected by the seasonal cycle and surface processes.

[39] Errors in the top 1000 m of the Iceland Basin remain particularly large in OCCAM over the four transects; whereas in ECCO the error in density is minimal, only enhanced by mesoscale features in the hydrographic data. The principal source of error in OCCAM occurs as a result of the NAC turning northward into the Iceland Basin too far to the east in the Subpolar North Atlantic Ocean.

[40] In the Irminger Basin both models are generally too warm in the intermediate ocean, resulting in a region of lighter fluid illustrated in Figures 4.13 and 4.14. The reason for this remains unclear. Insufficient winter mixing or the inability of z-level models to represent overflow characteristics are possible explanations for the erroneous temperatures.

[41] The independent comparison of ECCO with data from the FISHES hydrographic survey re-enforces the findings from the WOCE hydrographic comparison: ECCO is found to be cooler and fresher in the upper ocean. Overall ECCO, although not able to reproduce the true water mass characteristics, does appear to capture the variability observed along the WOCE hydrographic line.

4.6 Discussion of results

[42] A brief validation of two different Ocean General Circulation Models has illustrated stark differences both in relation to observational data and between each model solution. From the results presented here we find that the pathway of the NAC differs considerably in the two models. Upon reaching the Grand Banks of Newfoundland the NAC tends to continue eastward passed the MAR before turning northward into the Iceland Basin in OCCAM. The pathway presented in ECCO appears to be more realistic turning northward towards the Flemish Cap before flowing eastward. It is important to reproduce the correct pathway of the NAC, described by e.g. Kearns and Rossby (1998), as errors will result in unrealistic feedbacks in the model. Any deviation in the NAC pathway would introduce an *erroneous surface heat budget* (Willebrand *et al.*, 2001). Unlike OCCAM, that has prescribed forcing, ECCO produces an estimate of the atmospheric forcing fields required to reproduce the observed ocean (Stammer *et al.*, 2001). This would overcome the problem

of any inconsistency between the atmospheric forcing and the upper ocean. There are, however, inherent problems with this technique, because if the model is unable to produce a realistic ocean state estimation the atmospheric solution will also be incorrect.

[43] Although it can be difficult to separate model drift from secular changes in the model solution, the negative drift in OCCAM sea surface height field (Figure 4.4) is clearly unrealistic given the observational evidence. OCCAM is initialised from Levitus temperature and salinity fields, therefore the boundary conditions, forcing fields and model physics are not consistent and require a period of adjustment. The 8 year spin up may not have been an adequate period to run the model into steady state. Less clear though is the observed steric height trend in ECCO. The total steric component in ECCO accounts for a 1 *cm* rise during this period, although the upper steric component is decreasing and the lower increasing. Köhl *et al.* (2003) note that globally the upper 200 *m* are cooler and fresher than observations suggest, with the reverse true at depth in ECCO. They suggest that this is an indication that the mixed layer physics in the model are inadequate.

[44] The heat gain by the Subpolar Gyre region and subsequent rise in SSH during the mid 1990s is not only a function of reduced atmospheric heat flux, but is also linked to changes in the ocean circulation. Reverdin *et al.* (1999) proposed that as just over half of the steric height gain could be explained by the anomalous ocean-atmosphere heat flux the additional heat gain must be associated with warmer waters advected into the region. There is indeed a peak in the heat transport into the region and a reduction in the heat flux to the atmosphere in 1996 (see Figure 4.5a). The additional oceanic heat transport may be explained by the reduced Ekman flux southward out of the region during periods of low NAO. The remaining contribution to changes in SSH could be associated with variations in the Ekman pumping velocity and the raising or lower of the thermocline. Reverdin *et al.* (1999) suggests this should *induce* an anomaly in the vertically integrated heat content.

4.7 Summary

[45] The comparison of two OGCMs with observations reveals several sources of error and inconsistency. The principal source of error in OCCAM is the inability to reproduce

the pathway of the North Atlantic Current, which appears to be a common shortfall in z-level OGCMs (Willebrand *et al.*, 2001). The realistic wind forcing used in OCCAM is also unable to induce the variability observed in the position of the Subpolar Front. A lack of mixed layer physics in the model prevents convective overturning occurring in the Labrador Basin, which maybe linked to a relatively weak overturning streamfunction in the Subpolar North Atlantic region (not shown).

[46] ECCO, although lacking the resolution of OCCAM, performs better in producing a realistic ocean state estimate. Much of this can be attributed to the assimilation of observations in a effort to constrain the model solution. Interannual variability in the Subpolar North Atlantic is consistent with observation. Although density characteristics are similar to those in the hydrography, temperature and salinity characteristics are somewhat erroneous in the upper ocean. This is possibly due to insufficient mixing across the seasonal thermocline.

[47] The assimilation of quality observations into ocean models, like that used in ECCO, can provide *a qualitatively more accurate description of the ocean state than is available based on either observations or models alone* (Lu *et al.*, 2002). It can therefore provide a valuable resource in the analysis of the ocean's variability and associated mechanisms over a particular temporal period. It is to this end that, in the remaining chapters, we will focus on the variability in the ECCO OGCM and try to identify changes in the large-scale circulation and associated controlling mechanisms in the Subpolar North Atlantic Ocean.

Chapter 5

Variability of the horizontal circulation

5.1 Introduction

[1] In the previous chapter we have seen that the horizontal circulation exhibits a fair degree of variability (Figure 4.8). There is also evidence that the ECCO ocean state is consistent with observational data. Over the last decade there have been several changes observed in the circulation of the Subpolar North Atlantic Ocean and in particular the position of the Subpolar Front (Heywood *et al.*, 1994, White and Heywood, 1995, Bersch *et al.*, 1999, Bersch, 2002). Other large scale changes have also been documented; Reverdin *et al.* (1999) found that there were significant interannual changes in sea-level elevation in the central Subpolar Gyre during the mid 1990s. A proportion of this change was closely linked to the reduced heat flux during the winter months. As this mechanism alone did not account for the total steric change, Reverdin *et al.* suggested that there was an added contribution through remote advection of heat into the region. In an analysis of drifter data Flatau *et al.* (2003) suggest that there was a reduction in the northeastward flow through the Iceland Basin and cyclonic circulation around the Irminger Sea during the period 1996/8. All these large-scale changes are primarily attributed to variations in the NAO-index, as the dominant mode of atmospheric variability in the Subpolar region.

[2] Although hydrographic surveys are invaluable in their own right, they are, however, extremely limited both spatially and temporally. The focus of this chapter is to use the ECCO ocean state estimation that assimilates many forms of observational data in

a physically consistent manner, to examine changes in the circulation and water mass distribution over the last decade and to investigate associated mechanisms. We will begin in Section 5.2 by presenting the changes in the location of the Subpolar Front in the model, analogous to Section 3.4.1. In Section 5.3, we will address the possible mechanisms for the frontal shifts and other changes in the large-scale circulation. In Section 5.4 we will explore the possibility of different export pathways from the Subpolar Gyre during different periods of the last decade. We will also document large-scale propagating features observed in the model, their possible link to changes in the large-scale circulation and summarise current research (Section 5.5). Finally we will summarise our findings from this chapter.

5.2 Frontal variability

[3] Unlike the nature of subtropical fronts produced by an Ekman convergence in the surface layer, the oceanic front between Subtropical and Subpolar regions is characterised by differing water mass characteristics. Gill (1982) suggests that the properties of the Subpolar Front may be influenced by the Ekman suction in the Subpolar Gyre and Ekman pumping in the Subtropical Gyre. Bersch (2002) proposes that the NAO is responsible for changes in the circulation of the Subpolar North Atlantic and hence influences the nature of the Subpolar Front. He suggests that during negative phases of the NAO and weaker westerly winds, waters of Subpolar origin spread southward along the continental slope of Newfoundland rather than eastward across the MAR. Consequently the position of the Subpolar Front shifts to the east in the Newfoundland Basin and to the west in the Iceland Basin. White and Heywood (1995) suggest that the longitudinal position of the Subpolar Front in the Iceland is dictated by the latitudinal position of the zero in the wind stress curl. They found that in 1993/4 the position of the Subpolar Front was further to the east, by 2-3° of longitude, than in 1992/3. Changes may also be linked to upstream variations in the Gulf Stream or the influence of intermediate and deep circulation on upper ocean flow pathways.

[4] Figure 5.1 shows the pathway of the NAC through the Newfoundland Basin. The location of the pathway is determined by fitting a cubic spline to the coordinates of maximum flow or *core* of the NAC. We find that over the period of the model run the position of the core of the NAC at the northwest corner moves southeastward, a degree of variability

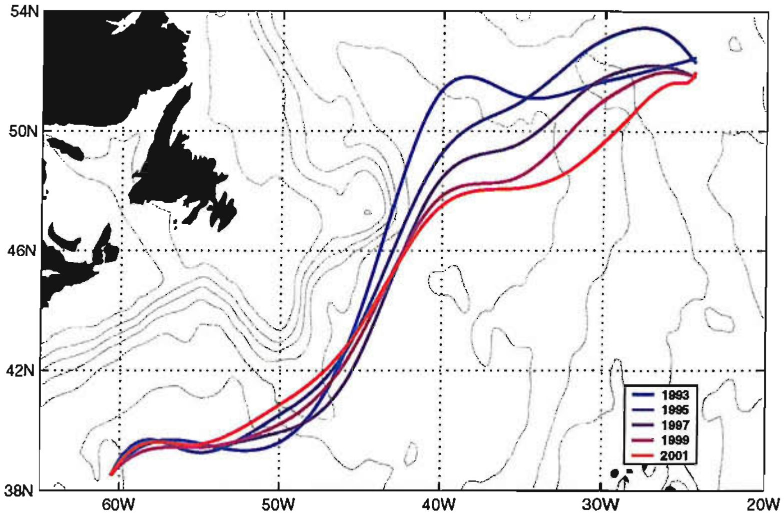

Figure 5.1: Interannual variability in the pathway of the North Atlantic Current in the Newfoundland Basin. *The pathway is defined by using a cubic spline through the locations of maximum flow in the region. Note that only every other year is plotted.*

that was not observed in the satellite study. However, the position of the NAC remains relatively unchanged south of 46°N. It is unclear as to the cause of this shift, although the time scale would suggest some kind of baroclinic adjustment. It is also noted that during this period the NAC decreased in strength over the model run.

[5] To examine this feature further we perform an EOF analysis on the depth integrated speed of the flow field over the upper 610 m of the water column. The upper 610 m was used as this described a significant proportion of the the NAC. The first two modes of this analysis describe coherently the evolution of the NAC over the model run (Figure 5.2). These two modes explain 66 % of the variance in the Newfoundland Basin. Upon closer inspection we see that the first mode of the EOF analysis, when projected back onto the mean field, explains the positional shifts of the current, whereas the second mode would infer that the flow narrows and intensifies between 1992 and 1995 before becoming increasingly broad and diffuse over the remainder of the run. Although the location of the maximum flow has shifted during the last decade, the position of the thermohaline front may not have due to a broadening of the current. To examine the changes in the position of the front across the Subpolar region we also examine the temperature and salinity fields.

[6] In Figure 5.3 we illustrate the year-to-year changes in the location of the Subpolar Front from the depth averaged temperature over the top 610 m of the water

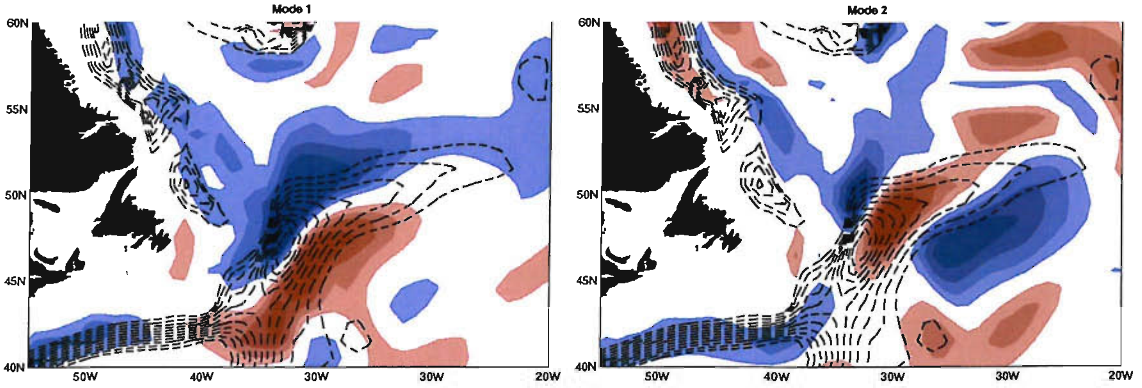

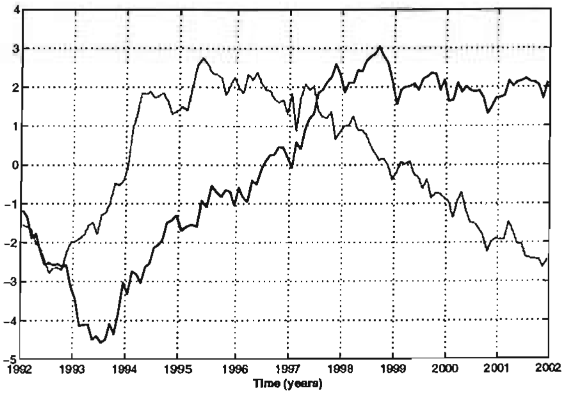

Figure 5.2: *The two leading spatial modes of an EOF analysis of depth integrated speed (0-610 m) in the Newfoundland Basin and their associated PCs (Mode 1, black, and mode 2, grey). The climatological mean speed is contoured (dashed lines) over the spatial modes for ease of reference.*

column in ECCO. The 8°C isotherm is taken here to represent the position of the front; we find a similar picture when contouring salinity. It is clear from the sequence of sub-figures that there are relatively large interannual changes in the position of this isotherm in the eastern Subpolar North Atlantic Ocean. Prior to 1996 the 8°C isotherm is east of the *climatological* mean position. After the NAO$^-$ event of 1995/6 the front is observed in a more westerly position, similar to changes observed in the satellite data (Figure 3.10). During the period between 1999 and 2000, NAO$^+$ years, the front retreats eastward to the position of the climatological mean. In the final year of the model run the front is observed in a more westerly position again, possibly linked to the NAO$^-$ winter of 2000/1. The eastward shift of the front in the Newfoundland Basin discussed by Bersch (2002) is not so apparent in the model data. There is a small shift to the east of the climatological mean in 1997/8, but not on the same scale as those shifts observed in the Iceland Basin.

[7] It is important to identify such changes in the strength and nature of the NAC and associated Subpolar Front as this is a significant pathway for the transport of heat poleward. It is shown both in the satellite data (Chapter 3; Figure 3.6a 1) and in the model that there is a weakening of the NAC. This weakening appears to be unrelated to any long term trend in the atmospheric forcing (see Figure 3.6b 1). However, it is unclear

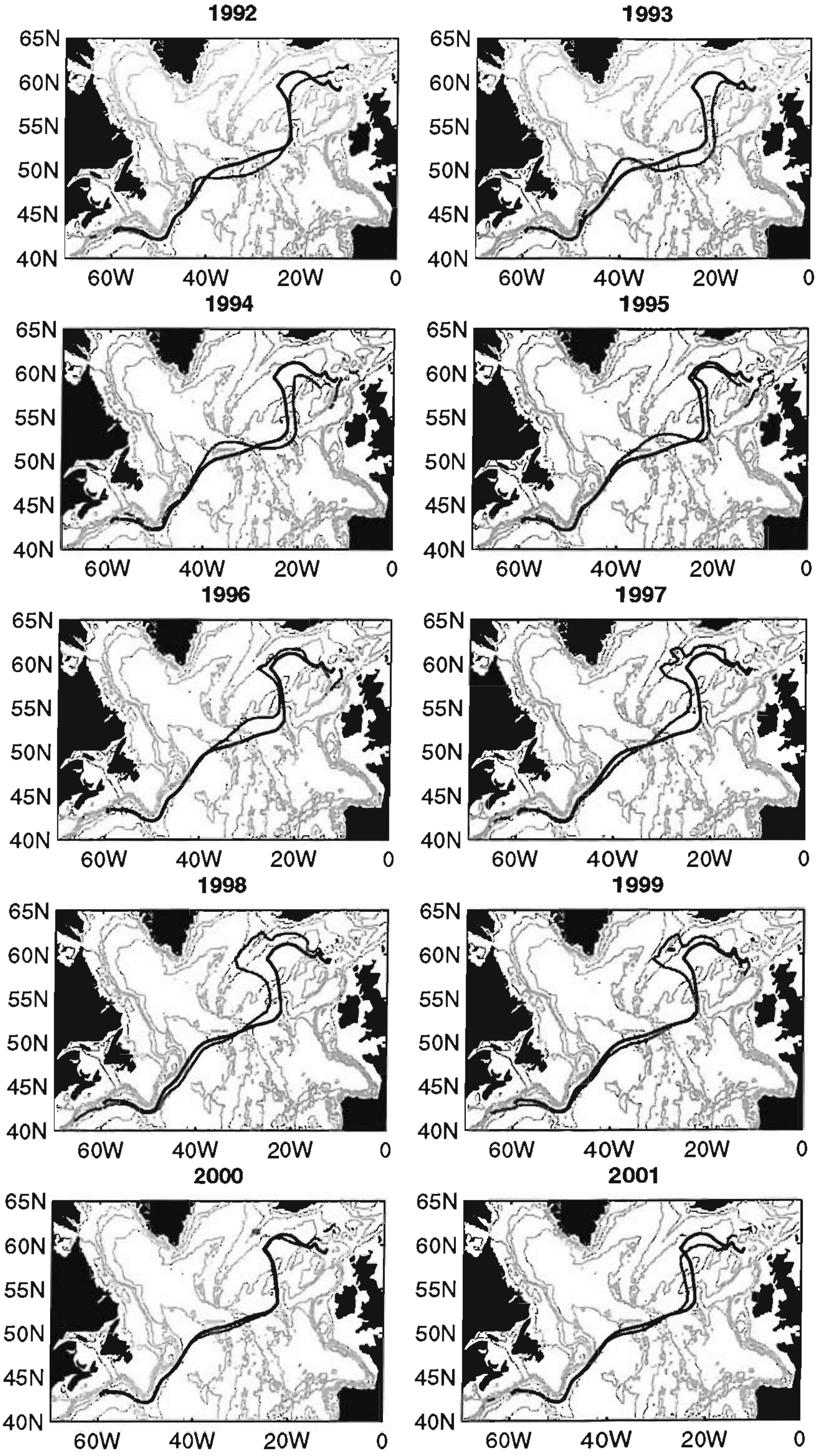

Figure 5.3: Shifts in the position of the Subpolar Front. *Annual means (grey) and climatological mean (black) of the 8° C isotherm of the depth integrated temperature (0-610 m).*

what precisely is causing this, but it is important nonetheless to note the changes as the NAC influences the climate of the Subpolar Region e.g. water mass characteristics, deep convection in the Labrador Sea etc.

5.3 Changes in the large-scale horizontal circulation

[8] In this section we will present the principal mechanisms controlling the large-scale horizontal circulation in the ECCO model. The first two modes of variability of the horizontal streamfuction:

$$\Psi_{bt}(x,y) = \int_0^L \int_{-H}^{\eta} v(x,y,z)dxdz \tag{5.1}$$

account for over 70% of the explained variance in an EOF analysis and therefore will be our primary focus. The first mode appears to contain much of the variability on seasonal to interannual timescales, whereas the variability of the second mode is of a predominantly lower frequency.

[9] Figure 5.4 shows the annual averages of the horizontal streamfunction. As we have previously illustrated there is a weakening of the circulation around the Subpolar Gyre over the model run (Section 4.3.3). From the sequence of annual averages we also find that the weakening of the Subpolar Gyre primarily occurs in the Labrador Basin. The consequence of this weakening is that towards the end of the model run the minimum in the streamfunction shifts from the Labrador to the Iceland Basin. These changes are gradual and are more likely to be linked with the lower frequency second mode as mentioned above.

First Mode

[10] Using the method of *Maximum Covariance Analysis* (MCA) monthly fields of the curl in the wind stress ($\nabla \times \tau$) and the horizontal circulation are analysed. The method of MCA identifies the closely coupled modes between two data fields (Björnsson and Venegas, 1997). This will allow us to explore the relative importance of the wind forcing on the variability of the horizontal circulation. A brief summary of this technique is outlined in Appendix B. As the two data fields used in this analysis are of different magnitudes, i.e. the Ψ_{bt} is of $O(10\ Sv)$ and the wind stress curl $O(10^{-7}Nm^{-3})$, it is necessary to normalise each data set prior to the analysis. This prevents one of the data sets, in this case the Ψ_{bt}, adding a bias to the covariance matrix used in the MCA.

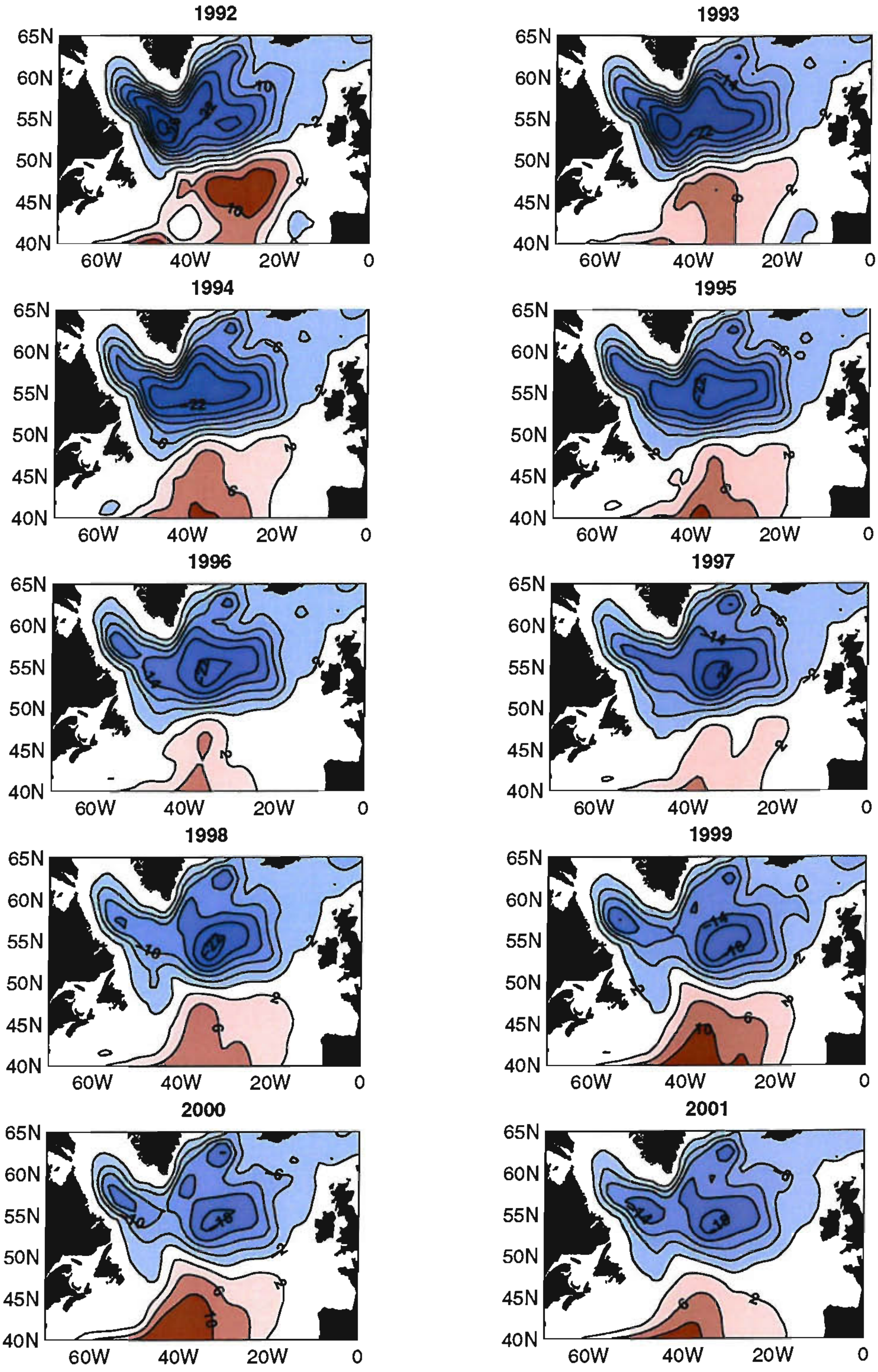

Figure 5.4: **Annual means of the depth integrated streamfunction of the Subpolar North Atlantic.** *Streamlines are contoured at 4 Sv intervals. Cyclonic circulation is signified by the blue shading and anti-cyclonic by the red.*

[11] In Figure 5.5 the spatial maps of the MCA are shown as homogeneous correlation maps[1]. Also depicted in Figure 5.5 are the temporal signals, and the associated correlation, r, giving a measure of the strength of the coupling.

[12] The first mode of the MCA, between Ψ_{bt} and $\nabla \times \tau$ (Figure 5.5a), accounts for 85% of total monthly variance of the ***combined*** signal. To assess the relative importance of each combined mode, the data are reconstructed (Equation B.5) and compared to the original data set. The variability observed in horizontal circulation at the Centre of Action (CoA) equates to a standard deviation of 4-5 Sv; values are similar once the seasonal cycle is removed prior to the MCA, 4 Sv with 90% of the variability accounted for by the first coupled mode. Figure 5.5b is the same as Figure 5.5a, but for an MCA between the Sverdrup transport and the wind stress curl, and reveals a qualitatively similar picture to that of $C_{map}(\Psi_{bt})$, although the zero line in $C_{map}(\Psi_{Sv})$ is a little further to the south. However, the two spatial maps of the wind stress curl and both PCs are identical suggesting that the principal mode of the horizontal circulation represents an immediate Sverdrup-*like* response to changes in the wind forcing.

[13] The fast barotropic response of the ocean circulation to the atmosphere may well impact on the shape of the Subpolar Front and on variations in oceanic heat transport in the region. On seasonal time scales the principal mode of the MCA represents an anomalous cyclonic circulation, centred on the Subpolar Front and to the south in the intergyre zone, in response to an anomalous negative south-to-north gradient in the wind stress curl during the summer months. Projected back on to the mean fields this represents an anomalous transport across the Subpolar Front and a decrease in the NAC in response to a weakening of the pressure gradient between the Iceland and the Azores. This seasonal character is also reflected on interannual timescales, although mostly dictated by winter-time variability and hence linked to the NAO. There is a 0.95 correlation between the winter-time PC (Ψ_{bt}) and NAO-index (95% significance level is 0.60). In the winters of 1995/6 and 2001/2 (NAO$^-$) we find a weakening of the pressure gradient leads to an anomalous cyclonic circulation centred on the Subpolar Front. This mechanism could conceivably be the catalyst for anomalous advection across the Subpolar Front and the *redistribution* of water masses in the Subpolar North Atlantic. This idea is consistent

---

[1] A spatial map of the correlation between the i^{th} principal component and the original data time-series at each grid point.

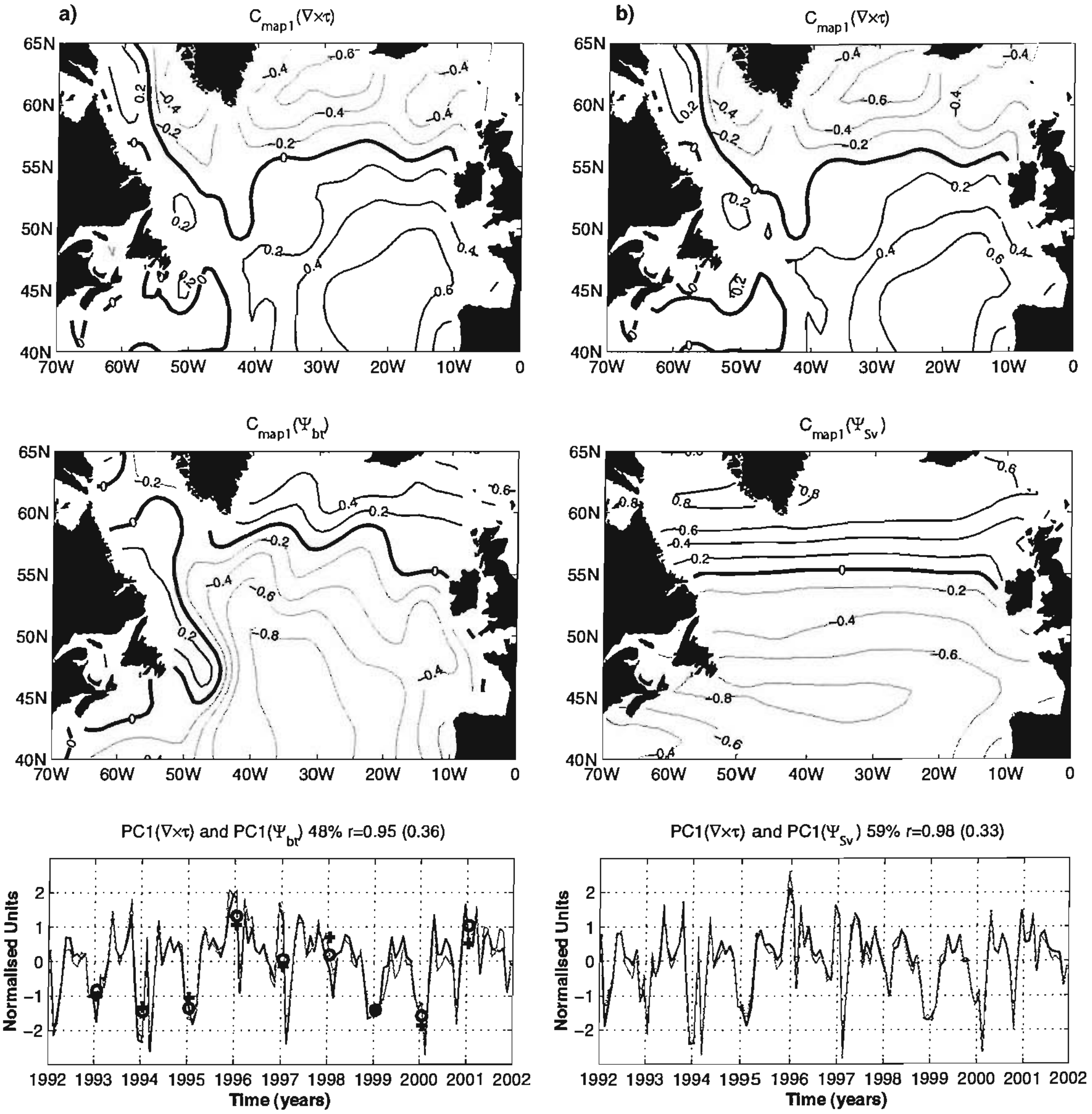

Figure 5.5: **Spatial maps and Principal Components (PC) for the leading mode of a MCA between the curl in the wind stress and *a)* the barotropic streamfunction and *b)* the Sverdrup transport.** *The spatial patterns are presented as homogeneous correlation maps, contoured with an interval of 0.2. The % indicates the fraction of the variance explained by each combined mode, r is the correlation between the two PCs (PC(*$\nabla\times\tau$*) is black and PC(*$\Psi_{bt/Sv}$*) is grey) and the values in the parentheses are the 99% significance levels for the correlations (determined by the autocorrelation of each PC, see Björnsson and Venegas (1997) for details). Winter-time values of *Ψ_{bt}* are plotted as black circles along with the winter-time NAO-index (black crosses). NB. the sign of the NAO-index is reversed for ease of comparison.*

with observations of the westward shift in the Subpolar Front in the Iceland Basin and a reduction in the eastward spreading of Subpolar Mode Water in 1996 (Bersch *et al.*, 1999).

[14] To assess the impact of this mode on the oceanic heat transport we take a transect through the CoA associated with the horizontal streamfunction at 45.5°N. Figure 5.6a shows the depth integrated heat transport anomaly, from Equation 4.2, to the west of the MAR and CoA (32.5°W) and Figure 5.6b the same but to the east.

[15] The two time series are anti-correlated, reflecting the nature of the first mode i.e. when northward transport to the east increases, the northward transport to the west decreases. We do not see the seasonal variations in the heat transport that we do in $PC1(\Psi_{bt})$. This is probably as a result of the seasonal heating and cooling in the upper ocean; even though the first mode suggests that there is a decrease in the northward volume transport, the additional heating of the summer months results in greater northward heat transport most notably to the west of the MAR. Also shown in Figure 5.6 are the winter-time heat transport and NAO-index. To both the west and the east there is a significant correlation between the heat transport and the NAO-index, 0.82 to the west and -0.85 to the east, 95% significance is 0.60. One would expect this high correlation as the first mode, dictating the circulation at the Subpolar Front and in the intergyre zone, is strongly coupled to the wind forcing, of which the NAO is the dominant mode of variability during the winter months.

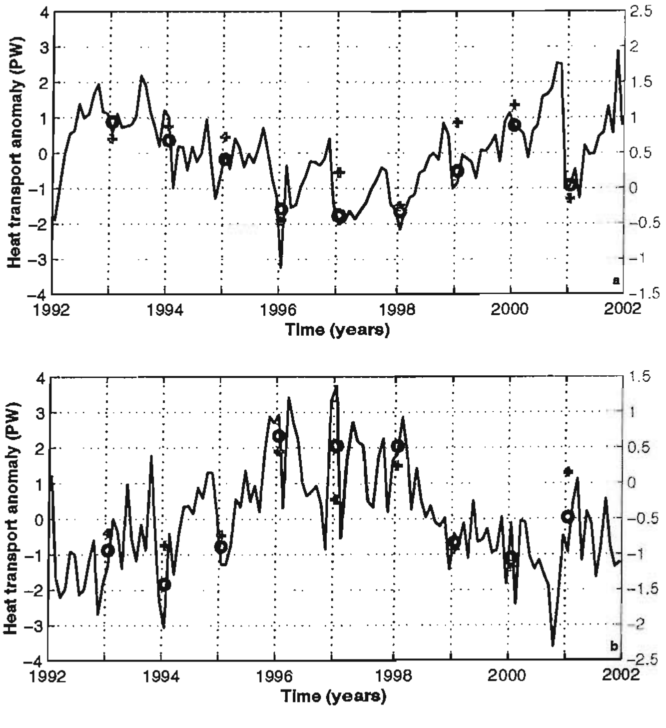

Figure 5.6: Heat transport anomaly (PW) at 45.5°N *a)* west of the MAR and *b)* east of the MAR. *Winter-time heat transport anomaly is indicated by the circles and the winter-time NAO index by the grey crosses. Note the sign of the NAO-index is reversed in b.*

[16] The anomalous northward heat transport to the east of the MAR observed during the mid 1990s coincides with the westward shift in the Subpolar Front in the Iceland Basin (Figure 5.3). During the period 1996-1998 an anomalous northward heat transport to east of the MAR and a westward shift in the front are associated with an anomalous cyclonic circulation. In the following years, 1999 and 2000, the scenario was reversed. The front retreated eastward in response to an anti-cyclonic circulation anomaly accompanied by an anomalous southward heat transport. In 2001, an NAO^- year, there is again an anomalous northward heat transport similar to that in 1996 with an accompanying westward shift of the Subpolar Front, although not of the same magnitude.

Second Mode

[17] The second mode of lower frequency variations is primarily reflected in the response of the circulation to changes in the baroclinic structure of the Subpolar Gyre. A similar MCA to that described previously reveals a strong coupling of the 1^{st} EOF in steric height and the 2^{nd} EOF of the horizontal streamfunction[2], accounting for 71% of the explained variance. Figure 5.7 illustrates the steric height changes between the beginning and the end of the model run. The dominant feature in the Subpolar Gyre is the large steric change in the Labrador Sea, coinciding with the location of the observed spin-down of the horizontal circulation, previously mentioned.

[18] We find close agreement in the steric height change between 1992 and 2001 (referenced to 2200 m) and the change in absolute sea surface height across the Labrador Basin (Figure 5.8). There is an increase in sea surface elevation in the central Labrador Basin and a decrease towards the boundaries over the model run. Associated with these changes is a slumping of the isopycnals in the central Labrador Sea, possibly linked to the reduced convective activity in the mid-to-late 1990s. Integrating the derived geostrophic velocity profile from such a sea surface height change produces an anomalous anti-cyclonic circulation and thus the observed spin down of the Subpolar Gyre.

[19] In a study of repeat hydrographic and altimeter data Reverdin *et al.* (1999) observe that there have been changes in sea level during the mid 1990s over the central Subpolar Gyre. They suggest that in addition to fluctuations in the heat flux, changes in the vertically integrated heat content could be attributed to anomalous advection. To investi-

---

[2] The 1^{st} EOF of the horizontal streamfunction being attributed to the atmospheric forcing.

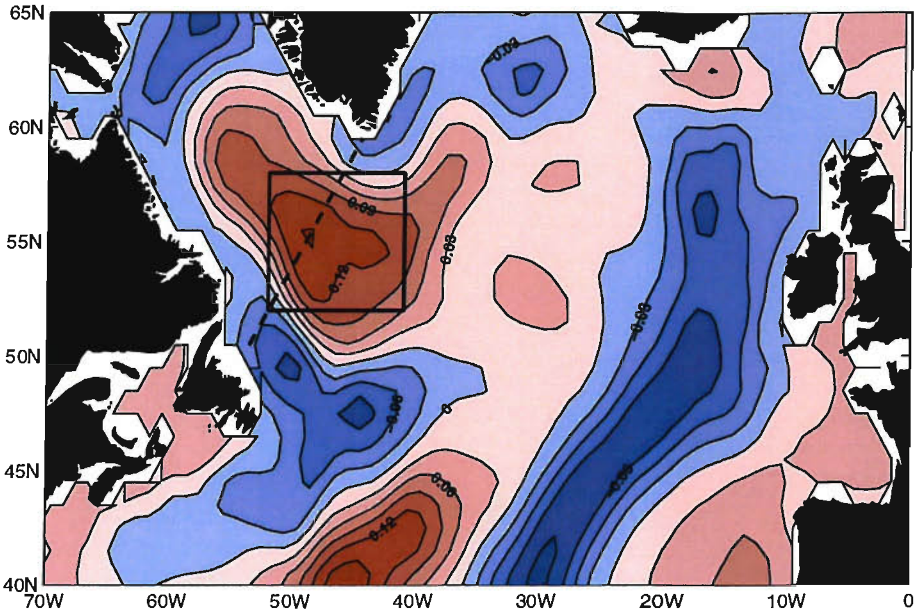

Figure 5.7: Difference in steric height between 1992 and 2001, the beginning and end of the model run. *Contours intervals are every 0.03 m.*

gate this idea further we take the region signified by the box in Figure 5.7 to examine the changes in heat energy within the Labrador region. The change in the vertically integrated heat content is expressed as:

$$hc = \rho C_p \int_{-H}^{\eta} \int \int \frac{\Delta T}{\Delta t} dz dy dx \tag{5.2}$$

where ρ is a reference density and C_p the specific heat capacity of sea water. Assuming that there is no significant contribution by diffusive processes the changes in heat content can be approximated by:

$$hc = ht - hf \tag{5.3}$$

where ht is the heat transport into the box, previously given by Equation 4.2, and hf is the heat flux from the box to the atmosphere.

$$hf = \int \int Q dy dx \tag{5.4}$$

where Q is the prognostic variable of heat flux (Wm^{-2}) stored in the model output. Figure 5.9 shows the break down of each of the components of Equation 5.3. The combined heat flux and heat transport value is very similar to that of the change in heat content, with the most notable gain in heat energy during the winter months in 1995/6. As one would expect the heat flux in the region sets the seasonal variability, with little contribution from

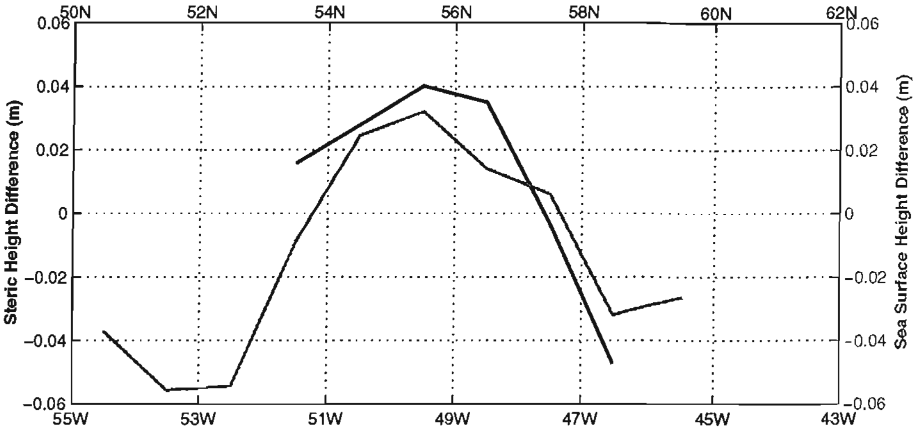

Figure 5.8: Steric height change from 1992 to 2001 (black line, referenced to 2200 m) and the absolute sea surface height change from 1992 to 2001 (grey line) across the Labrador Basin. *See dashed line in Figure 5.7 for location of the transect.*

advection. However, the interannual changes in the two components are of a comparable magnitude.

[20] We have already shown the difference in sea level elevation between years of 1995 and 1996, with the switch from an NAO$^+$ to an NAO$^-$ phase, from altimeter data in Figure 2.8. Figure 5.10 shows the time evolution of the sea surface height anomaly and the steric height anomaly. The latter is given by:

$$\eta'_p = \frac{1}{\rho_0}\int_{-H}^{0} \rho(S,T,z)' dz \tag{5.5}$$

where ρ, the density, is dependent upon salinity (S), temperature (T) and pressure (P) (Stammer, 1997). Also plotted are the thermal and haline components of the steric height anomaly which are calculated simply by setting $S = 35$ and $T = 0$ respectively in Equation 5.5.

[21] While the seasonal cycle in both the sea surface height anomaly and the steric height anomaly are of similar magnitude, primarily dictated by the thermal component, the long term trend in the steric height anomaly appears to be set by the haline component. The increase in steric height over the model run from the haline component corresponds to a freshening of 0.033 over the whole of our domain. This freshening in the Labrador Sea is consistent with observations reported by Dickson *et al.* (2002), who found a freshening of deep waters in the Labrador Sea of the $O(0.02)$ over the last decade.

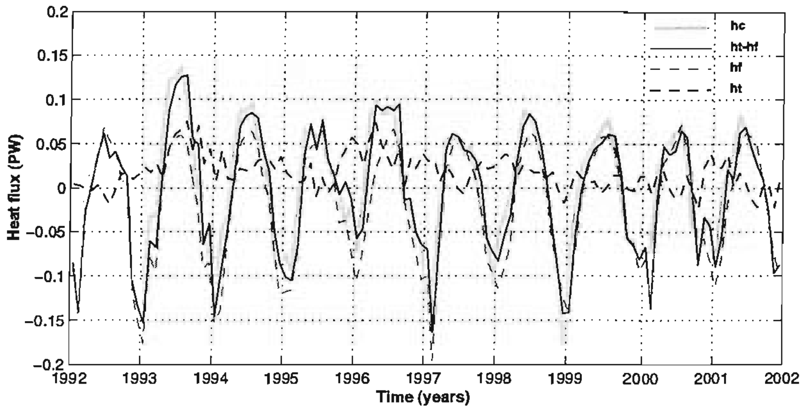

Figure 5.9: Heat energy balance in the Labrador region signified by the rectangular box in Figure 5.7. *The change in oceanic heat content hc is given by the thick grey line,* $ht - hf$ *by the thin black line and ht and hf by the dark and light dashed grey lines respectively.*

[22] To address the question concerning the change in the *heat content* in the Labrador region we break down the thermosteric component into contributions from the heat flux and heat transport by calculating the associated changes in sea surface height (Equation 4.5; Figure 5.11). Focussing on the changes in steric height between the NAO^+ year of 1995 and the NAO^- year of 1996 we find that in addition to the height change induced by a reduced heat flux there is also a comparable contribution to the sea level change from the advective component ($\sim$ 2 *cm* by each). We also note that there was a significant contribution to the steric height change by the advective component in 1993, although conversely there was an increase in the heat flux during this period. The northward excursion of the NAC during this period (Section 5.2) would explain the gain in heat energy by advection during an NAO^+ year. After the event of 1995/6 the anomalous heat gain remains until 1999 when a switch in the phase of the NAO reduces the contribution of heat energy through advection. This appears to be characteristic of a baroclinic response of the ocean, as there is no instantaneous response. In 2001, a NAO^- year, there is an increase in the heat flux component of the steric height, but very little from the advective component, which suggests that the relationship between changes in the atmosphere, in particular the NAO, and the ocean is more complex than often suggested.

[23] To further quantify the changes in sea level observed by Reverdin *et al.* (1999), we take a closer look at the anomalous heat transport between 1995 and 1996. Figure 5.12a illustrates the difference in heat transport, per m^2, between these two years along each side

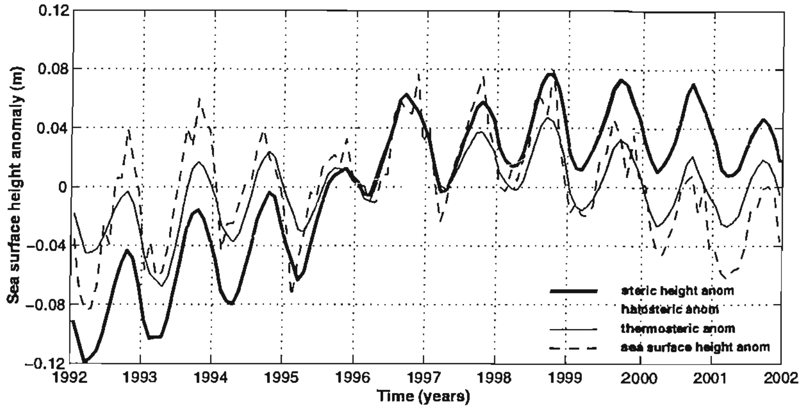

Figure 5.10: Time evolution of the absolute sea surface height anomaly (dashed), steric height anomaly (thick black), thermal component of the steric height anomaly (dark grey) and haline component of the steric height anomaly (light grey) in the central Labrador Sea.

of the sample domain in the Labrador Sea (heat entering the region is signified by the red shades). From this we find that the majority of anomalous heat enters the Labrador region from the southeast-to-east and from the north of the domain. The first, penetrating deeper in the water column could possibly be from the influence of the NAC or a strengthened Labrador Current retroflection (Bersch, 2002). The anomalous heat transport into the north of the domain is predominantly a surface feature. We suggest that this is remote advection of waters from the Irminger Basin that also have experienced the reduced heat fluxes of the 1995/6 winter via the Greenland currents. The total heat transport integrated

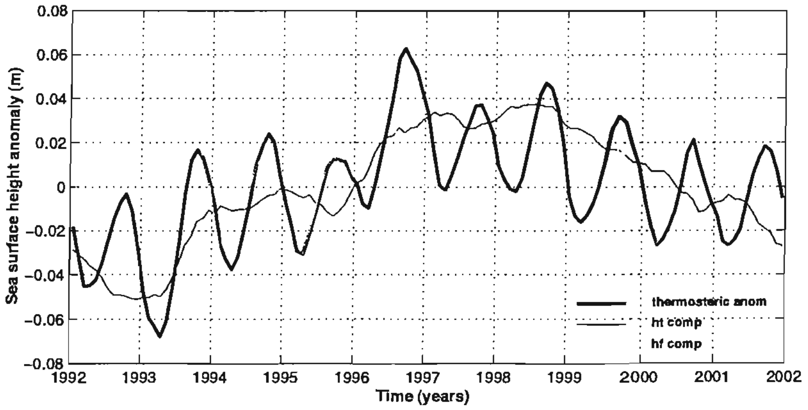

Figure 5.11: Time evolution of the thermal component (thick black), heat flux component (light grey) and heat transport component (dark grey) of the sea surface height anomaly in the central Labrador Sea.

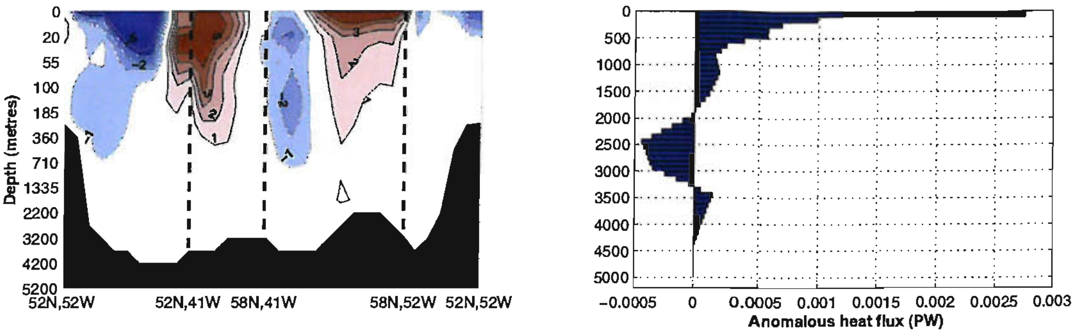

Figure 5.12: ***Left*, the difference in heat transport between 1995 and 1996 (Wm^{-2}) along each side of the box in the Labrador region defined in Figure 5.7.** *Contour intervals are 1×10^5 Wm^{-2}. Right, Total heat transport as a function of depth. Bin intervals are every 100 m.*

around the perimeter of the domain confirms that the majority of the anomalous heat transport into the region occurs in the upper ocean (Figure 5.12b).

[24] In summary: two modes of variability in the horizontal circulation have been identified that account for over 70% of the explained variance. The first mode is closely coupled to the wind forcing on seasonal-to-interannual time scales and thus to the NAO. The spatial pattern of the *First Mode* is unchanged once the seasonal cycle is removed. This suggests that the interannual characteristics (namely the NAO) are similar to those of the high frequency procession of the seasons, as suggested by Flatau *et al.* (2003). Moreover fluctuations in the *First Mode* appear to provide a plausible mechanism for the change in the characteristics of the Subpolar Front, at least in the eastern Subpolar North Atlantic.

[25] The *Second Mode* characterises the lower-frequency variability of the system. Changes in the baroclinic structure of the Labrador Sea are found to influence the strength of the Subpolar Gyre. The first mode of the winter mixed layer depth in the Labrador region (not shown), explaining 39% of the variance, reveals a progressive decrease over the model run, which could have a dynamical link to the decrease in the strength of the circulation in the Labrador region. In an idealised model experiment, forced only by varying heat fluxes and a wind stress climatology, Eden and Willebrand (2001) found that there was a 2-3 year lagged response in the barotropic streamfunction to the mixed layer depth in the Labrador Basin. This they suggest, was a coupling of the baroclinic structure and the barotropic mode. The results presented here emphasise the importance of the baroclinic structure on the long-term evolution of the circulation of the Subpolar Gyre.

5.4 Lagrangian analysis

[26] Export pathways of deep and intermediate waters from the Subpolar Gyre may be influenced by the anomalous circulation brought about by changes in the atmospheric forcing (Section 5.3). This in turn may alter the ocean's response to climate variations in particular the dynamical response in the Subtropical basins (Curry and McCartney, 1996). Lozier (1997) and Bower *et al.* (2002) have suggested that there may exist different export pathways of North Atlantic Deep Water either side of the MAR; along the western boundary and along the eastward flank of the MAR. Bersch (2002) also claims that there has been reduced spreading of Labrador Sea Water east across the MAR during the mid 1990s.

[27] Here we examine the mass transport over three different periods:

- 1993 an NAO^+ year,
- 1996, the year following the extreme NAO^- winter of 1995/6 and extended period of NAO^+ forcing
- and 2001, an NAO^- year, but after a reduced period of NAO^+ forcing.

Using lagrangian diagnostics and monthly mean velocity fields from the ECCO model, we quantify the mass transport for each of these period. In addition, we examine whether or not there is any significant change in the export pathways to the south, in response to a change in the phase of the NAO and shape and strength of the Subpolar Gyre.

[28] Lagrangian diagnostics presented in this section are based on an algorithm developed by Blanke and Raynaud (1997) to compute passive particle trajectories given a stationary velocity field on a *C-grid* configuration. Annual mean mass exchanges are derived from 12 independent monthly lagrangian integrations, therefore retaining any seasonal variations.

[29] The changing shape of the Subpolar Gyre previously mentioned is illustrated qualitatively in Figure 5.13. Particle trajectories follow a more direct pathway from west of the MAR into the Iceland Basin in 1998. The pathway through the Iceland Basin is further to the west in 1998, consistent with the shift in the Subpolar Front. Once in the Subpolar Gyre particles remain in the Labrador Basin in 1998, whereas in 1993 they follow a more protracted route across the MAR into the Iceland Basin before returning to the

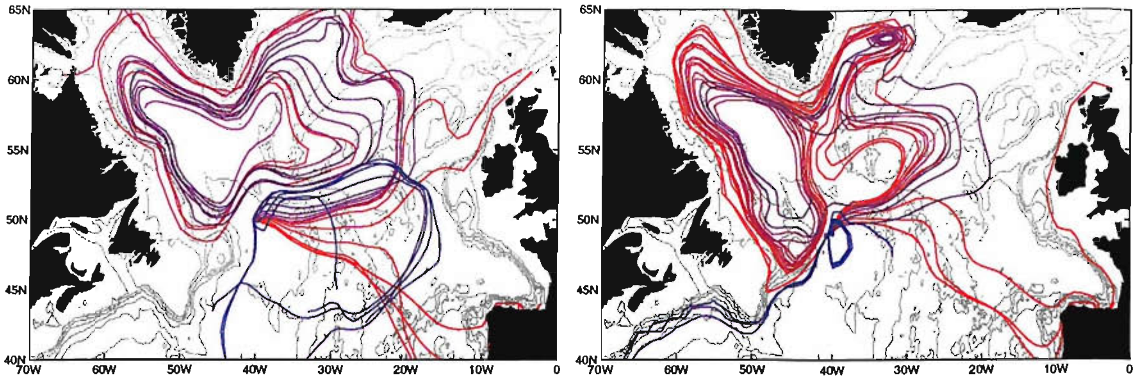

Figure 5.13: Lagrangian particle tracking in the Subpolar Region. *A series of particles were seeded to the west of the Mid Atlantic Ridge between the surface (red) and depth (blue) and tracked in the mean velocity field for the years left) 1993 and right) 1998.*

west. These observations are again consistent with hydrographic data presented by Bersch (2002), who identifies an anomalous southward spreading of Labrador Sea Water in the Newfoundland Basin after the NAO$^-$ event of the mid 1990s.

[30] Surface particles, indicated by the *flame* red contours, travel immediately southeastward in Ekman layer towards 40°N, 15°W in both years, more so in 1993 (NAO$^+$), due to stronger zonal winds (see Figure 2.9). Particle trajectories in the intermediate and deep ocean ocean reveal very different circulation characteristics. In 1993 the particles at depth circulate the inter-gyre zone anti-cyclonically. They pass over the MAR, possibly through one of the fracture zones, before circulating southward, whereas in 1998 these particles tend to circulate to the west of the MAR and follow the pathway of the Deep Western Boundary Current. This example highlights the immediate barotropic response of inter-gyre zone to changes in the atmosphere, illustrated by the principal mode in the MCA (Section 5.3).

[31] To further quantify these changes a series of off-line lagrangian experiments were performed. A series of particles were seeded along, and over the full ocean depth of, a transect in the Labrador Sea ($O(10000)$ particles accounting for 1×10^{-2} Sv each). The particles were tracked in monthly mean flow fields until they exited the study domain. Figure 5.14 illustrates the export pathways of waters from the Labrador Basin for the three years of interest. These data are additionally broken down to examine the export of waters from the upper and lower ocean (Table 5.1).

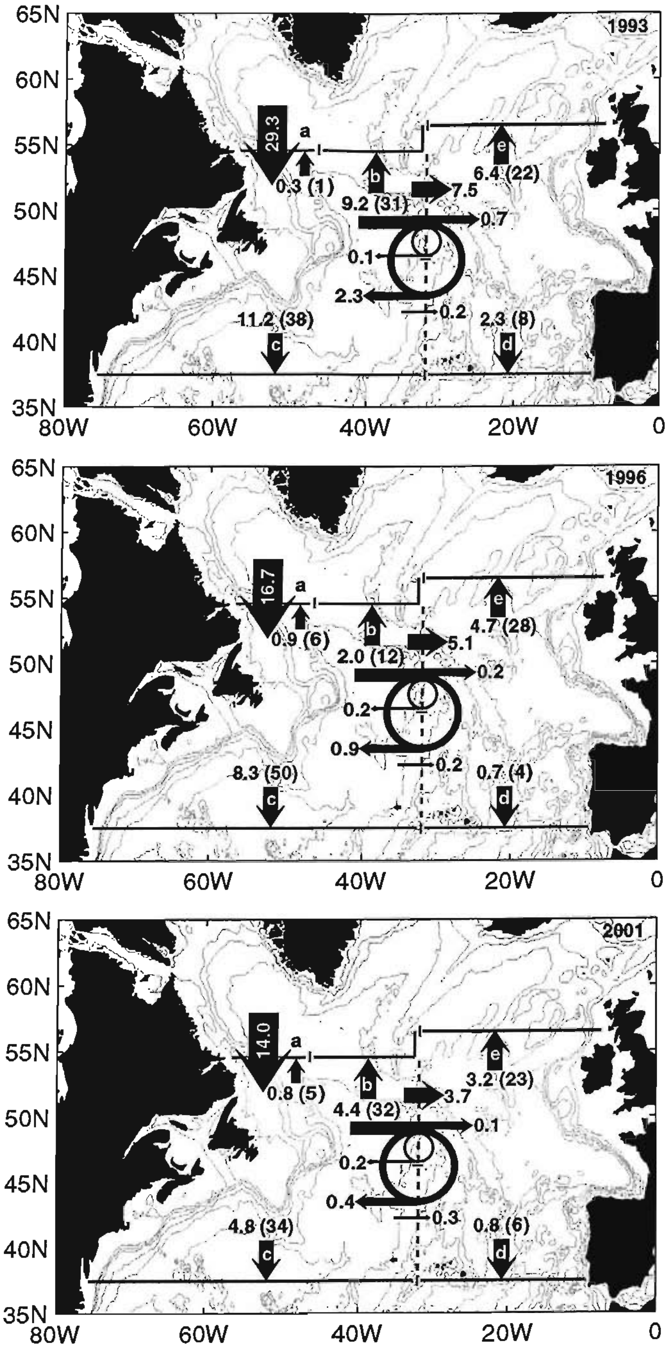

Figure 5.14: Quantitative lagrangian particle tracking in the Subpolar Region. *A series of particles were seeded in the Labrador Basin and subsequently tracked until leaving the study domain for the years 1993, 1996 and 2001. Sections are defined* **a** *through to* **e** *. Transport values are in Sv and percentages are given in the parentheses.*

[32] The total volume flux in each of the years is different as there is a varying degree of southward transport through the cross sectional area of transect **a** at different times of the model run. With the spin-down of the Subpolar Gyre there is an associated weakening of the southward transport in the western Labrador Sea between 1992 and 2001. In addition an increasing percentage of particles seeded along the transect in the Labrador Basin may not enter the sample domain as a consequence of the changes in circulation over the model run.

[33] If we now examine the export of water of Labrador origin to the south, through sections **c** and **d** (Figure 5.14 and Table 5.1), we find that there are differences between the NAO$^+$ year of 1993 and NAO$^-$ year of 1996. In 1993 38% of the particles starting out in the Labrador Sea follow a southward pathway to the west of the MAR compared to 50% in 1996. Limiting the analysis to particles released below 1500 m we find an increased percentage transport through this section with values of 62% and 87% in 1993 and 1996 respectively. The

	a	b	c	d	e	total
1993 *total*	0.3 (1)	9.2 (31)	11.2 (38)	2.3 (8)	6.4 (22)	29.3
upper	0.2 (1)	6.2 (43)	2.0 (14)	1.2 (9)	4.8 (33)	12.6
lower	0.1 (0)	3.0 (20)	9.1 (62)	1.1 (7)	1.5 (10)	14.6
1996 *total*	0.9 (6)	2.0 (12)	8.3 (50)	0.7 (4)	4.7 (28)	16.6
upper	0.7 (8)	1.9 (22)	1.3 (16)	0.5 (6)	4.2 (48)	9.6
lower	0.2 (3)	0.1 (1)	7.0 (87)	0.2 (2)	0.5 (6)	8.0
2001 *total*	0.8 (6)	4.4 (31)	4.8 (34)	0.8 (6)	3.2 (23)	14.0
upper	0.4 (4)	4.1 (45)	1.4 (15)	0.7 (7)	2.5 (28)	9.1
lower	0.4 (8)	0.3 (5)	3.4 (71)	0.1 (2)	0.6 (13)	4.8

Table 5.1: Exports from the Labrador Sea *Transports, in Sv, through sections shown in Figure 5.14 for 1993, 1996 and 2001 (percentage of total given in parentheses). The upper water column is defined as that above 1500 m and conversely the lower below.*

reverse is true to the east of the MAR with 7% of the particles released below 1500 *m* in 1993 reaching section **d** and just 2% in 1996. This suggests that the circulation anomaly indicated in the first mode of the MCA may influence the spreading and export of intermediate and deep waters from the Labrador Basin; the anticyclonic anomaly promoting an eastward shift in the Subpolar Front in the Newfoundland Basin and eastward spreading of Labrador Sea Water in 1993, whereas the converse is true in 1996. However, in 2001 although the percentage of particles released below 1500 *m* reaching each section is between those of 1993 and 1996 as one might expect, 71% to the west and 2% to the east, over the total depth range figures are similar to that of 1993. As we have seen from the satellite data, however, 2001 represents a switch from an NAO^+ to and NAO^- phase, as did 1996, the change in circulation appears to be characteristically different.

[34] With the increased spreading eastward in NAO^- years one might expect to observe an increase in export into the eastern Subpolar North Atlantic in addition to anomalous export to the southeast through section **d**. Examining the two northern sections, **b** and **e**, we find that the largest difference between each of the years is through section **b** into the Irminger Basin. In 1993 the export from the Labrador Basin was larger into the Irminger Basin than into the Iceland Basin. In 1996 the reverse was true. The largest difference is seen when examining the export below 1500 *m*. In 1993 20% was exported to the Irminger Basin compared to 1% and 5% in 1996 and 2001 respectively. To the east the export figures are a little more similar. Overall the export through these sections is less in

1996 than in both 1993 and 2001. The greater upper ocean transport observed at section e into the Iceland Basin in 1996 may be due to a combination of reduced southward Ekman transport and the wind induced cyclonic circulation anomaly centred on the Subpolar Front previously discussed.

[35] From this brief study into export from the Labrador Sea we have not conclusively established the existence of an export pathway along the eastern flank of the MAR to the south, but have shown significant changes in the export to the west of the MAR. In a negative phase of the NAO the preferential pathway for export from the Labrador Basin southward is to the west of the MAR. In a positive phase there is increased transport into the Irminger Basin and possibly south east of the MAR. Further studies are required to determine the changes in export with the circulation using longer model integrations and to address the question of how topography may influence the export.

5.5 Propagating Features

[36] Recently there has been growing interest in the low-frequency propagation of large-scale temperature anomalies across oceanic basins. Using ship based observations Sutton and Allen (1997) have previously shown the existence of sea surface temperature (SST) anomalies propagating eastward along the pathways of the Gulf Steam (GS) and NAC. From a Hovmöller diagram they observed the SST anomalies to propagate at speeds significantly slower ($\sim$1.7 cms^{-1}) that that of the typical near surface currents. They hypothesize that these anomalies could in fact be advected by subsurface currents. From recent modelling efforts Sinha *et al.* (2004) also observe similar eastward propagating features along the boundaries between the oceans Subtropical and Subpolar Gyres.

[37] Previous studies into SST variability in the North Atlantic have focussed primarily on the dominant stationary mode, the SST tripole. Rodwell *et al.* (1999) and Mehta *et al.* (2000) identified possible feedback/forcing from SSTs on the atmosphere, underlying the importance of coupling between the two systems. If there is any significant feedback from eastward propagating SST anomalies Sutton and Allen (1997) suggest that a degree of predictability will be introduced into the system. Most if not all previous studies into these eastward propagating anomalies have focussed on surface features. Here we present

results from ECCO that suggest that in fact these features are observed not only at the surface, but over the upper 610 m of the water column.

[38] There are several theories for the generation and eastward propagation of surface temperature anomalies. As previously mentioned, Sutton and Allen (1997) suggested that the subsurface propagation of anomalies is communicated to the surface layers during the winter periods when the seasonal thermocline is eroded. Conversely, in a recent model analysis Sinha *et al.* (2004) found that surface anomalies propagated eastward at speeds consistent with that of the mean surface flow field to first order, with no dynamical contribution from the anomaly itself. Other possible mechanisms include; the eastward advection of Rossby waves by the mean flow (Nonaka and Xie, 2000) and the effect of the variable speeds of Rossby wave propagation[3] leading to the apparent eastward propagation of anomalies along the Gyre boundary (*Killworth pers. comm.*). One final mechanism is that suggested by Cooper and Gordon (2002), whereby anomalies are thought to be influenced by the production of mode waters in the Labrador Basin and their subsequent interaction with the NAC.

[39] One of the contentious issues in these previous studies is the method used for identifying the eastward propagation of surface features. In both studies by Sutton and Allen (1997) and Cooper and Gordon (2002) the traditional tool of a Hovmöller diagram was used. In Sutton and Allen (1997) temperature anomalies along the climatological pathway of the Gulf Stream and NAC were identified. Whereas in the study by Cooper and Gordon the mean pathway of the major current systems was used as their modelled NAC followed a more southerly trajectory into the Subpolar North Atlantic Ocean. As we have previously seen there is a strong front associated with the region separating the Subpolar and Subtropical Gyres. We have also shown evidence, both in the ECCO model (Section 5.2) and in the Satellite data (Chapter 3), that there are significant shifts in the Subpolar Front from the climatological mean location. These interannual fluctuations in the frontal system will introduce anomalies in temperature and salinity along the climatological mean pathway of the NAC not associated with the locally propagating features in the region. In the following analysis we will present our results firstly in the form of the conventional

---

[3] As the propagation speed of Rossby waves rapidly reduces with latitude, the signal at higher latitudes will tend to arrive at the western boundary after those at lower latitudes. The Rossby waves are generated from a northward propagating Kelvin wave along the eastern boundary.

Hovmöller diagrams, then using the more sophisticated technique of Complex Empirical Orthogonal Function analysis.

[40] Typical length scales of the anomalies observed in ECCO are of the order of several 100s of kilometres and are present over the upper 610 m of the water column. Near surface anomalies are $\sim \pm 3$ °C and $\sim \pm 0.6$ in salinity. Propagation speeds near the surface appear to be quicker than at depth, $\sim 5-6\ cms^{-1}$. At a depth of 610 m anomalies are $\sim \pm 2$°C and $\sim \pm 0.1$ in salinity. Propagation speeds at this depth are of the $O(1\ cms^{-1})$. The density signal of these anomalies is dominated by the temperature and also appears to have corresponding signals in both velocity and sea surface height fields. The anomalies generally propagate along the boundary between the Subpolar and Subtropical Gyre, turning northward into the Iceland Basin before decreasing in magnitude. Figure 5.15 illustrates the propagation of temperature anomalies eastward along 49.5°N at various depths. Note that the magnitude of the anomalies decreases towards the east. This is as a direct result of the anomalies taking a more northeastward trajectory to the east of the MAR away from the sampled latitude. These features are also confirmed in 2D animation sequences of temperature anomalies at various depth levels. For an example see Figure 5.16.

[41] It is unclear whether the propagation mechanism of anomalies across the Subpolar North Atlantic Ocean is simply through the advection by the mean flow. Examination of the Hovmöller diagrams (Figure 5.15) and the typical velocities found at each level of the model reveal that they are of approximately the same order of magnitude. However, in Figure 5.16 we see that this may not always be the case. A negative temperature anomaly has been identified propagating from west to east. Using the lagrangian diagnostic techniques previously described (Section 5.4), we can track the location of particles in the flow field. In a qualitative experiment, nine particles have been seeded in the negative temperature anomaly and set to a fixed depth level. Initially it appears that the passive particles and temperature anomaly are being advected at similar speeds. Although by the summer of 1994 we find that the particles have left the anomaly. As the neutrally buoyant particles are being advected by the instantaneous flow field, therefore containing any dynamical changes due to the anomaly, this would suggest that the anomaly is being

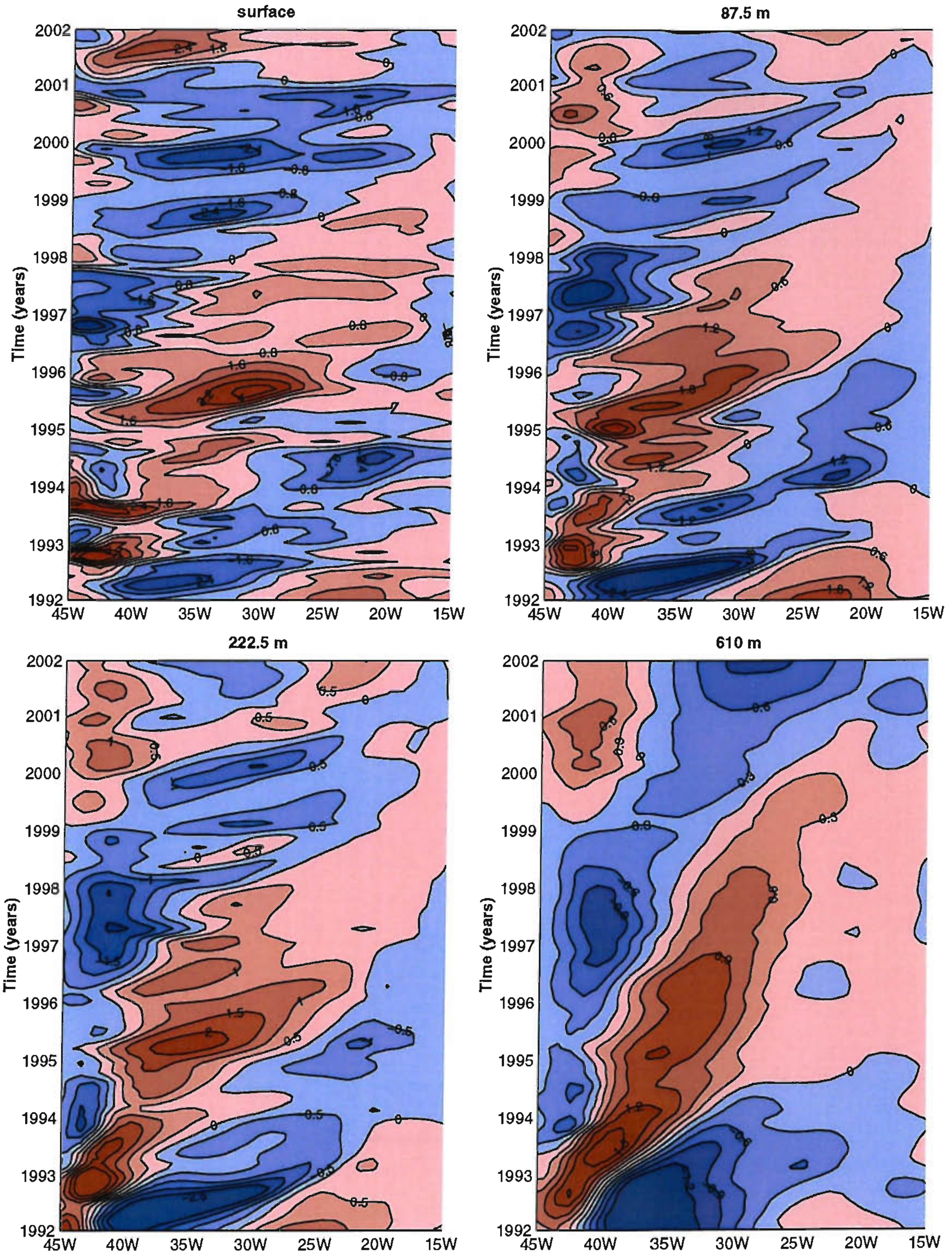

Figure 5.15: A series of Hovmöller diagrams illustrating the propagation of temperature anomalies at various depths in the upper ocean along 49.5°N. *Intervals are irregularly contoured.*

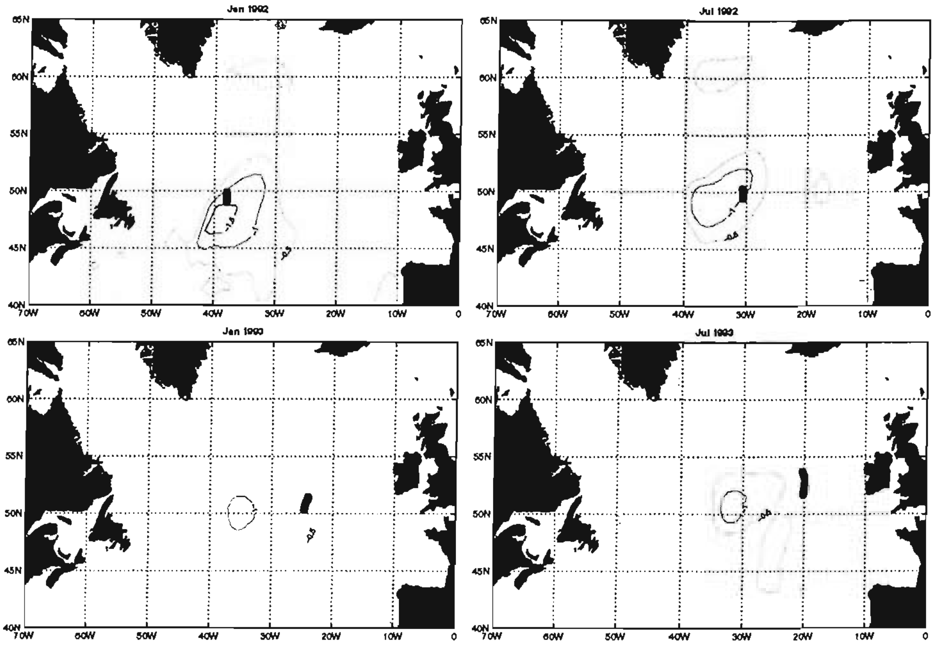

Figure 5.16: A series of snap-shots of the propagation of a negative temperature anomaly along the boundary between the Subpolar and the Subtropical Gyre at 222.5 m. *The anomaly is contoured every 0.5° C. Nine neutrally buoyant passive particles (black circles) were seeded in the negative temperature anomaly on January 1992.*

modified in the vertical.

[42] In the original unfiltered Hovmöller diagrams we see a difference in propagation speed and magnitude of the anomalies. At the surface, even after the seasonal cycle is removed from the temperature field, an eastward propagating signal is seen at annual frequencies (Figure 5.15 'surface'). This suggests that there is indeed a component advected by the mean flow field, which is also noted by Krahmann *et al.* (2001). At 610 m there is a slower multi-annual signal, of the $O(1\ cms^{-1})$. If we now low-pass filter the time series removing annual and sub-annual frequencies, we find a more coherent pattern over a range of depth levels (Figure 5.17). Propagation of temperature anomalies at the surface are now of the $O(1\ cms^{-1})$, significantly slower than that of the mean flow. Figure 5.18 shows the lagged correlation analysis between the surface signal and that at 222 m and 610 m respectively. To a depth of 222 m the propagation of temperature anomalies is significantly tied between 45°W and 15°W, with no obvious lead or lag present. At 610 m the signal is not as closely tied to the surface signal. Although still significantly correlated to the surface anomalies the signal at the surface propagates eastward at a greater speed that at depth signified

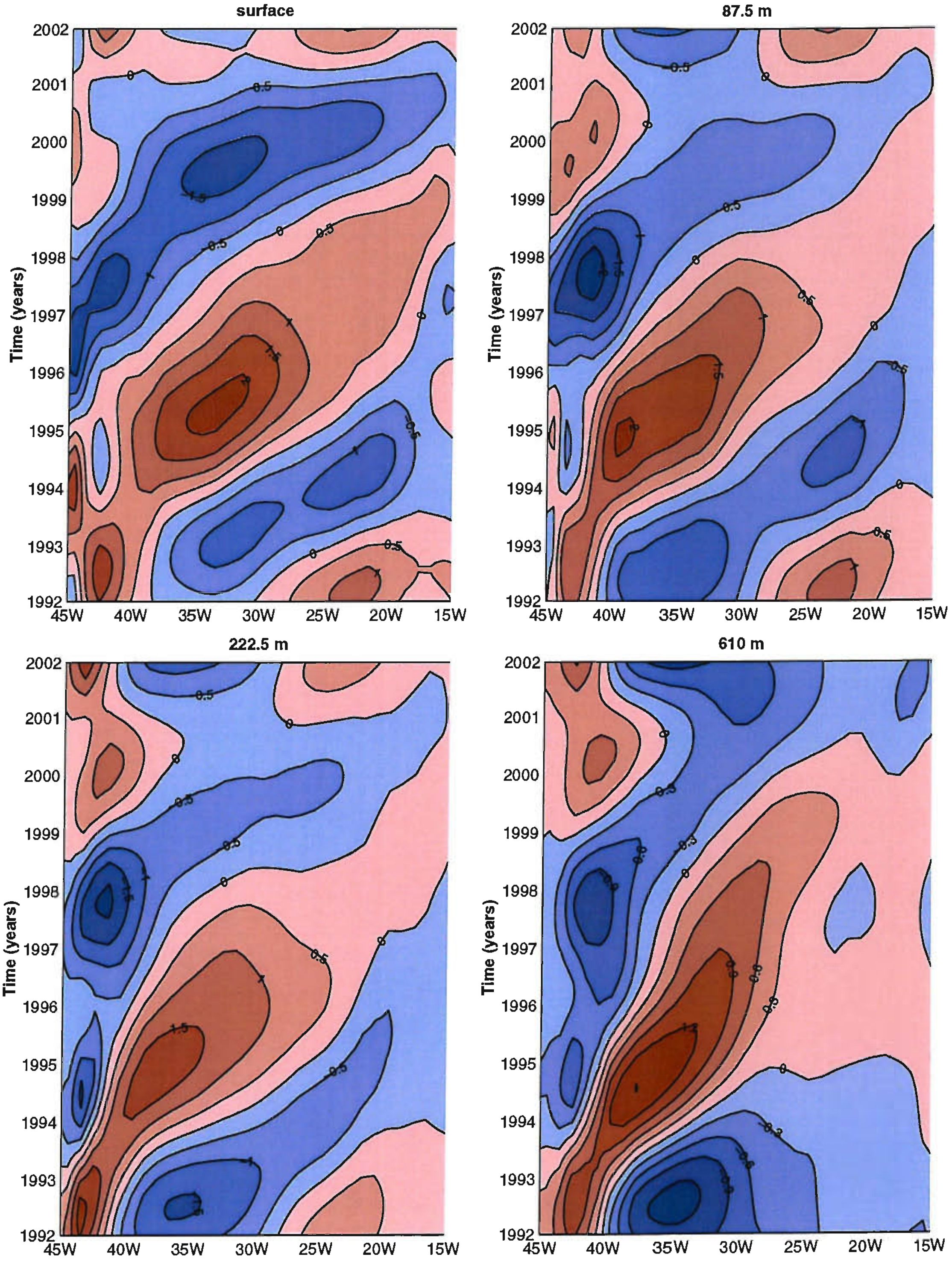

Figure 5.17: As Figure 5.15, but all data have been low-pass filtered removing frequencies greater than 0.4 yr^{-1}.

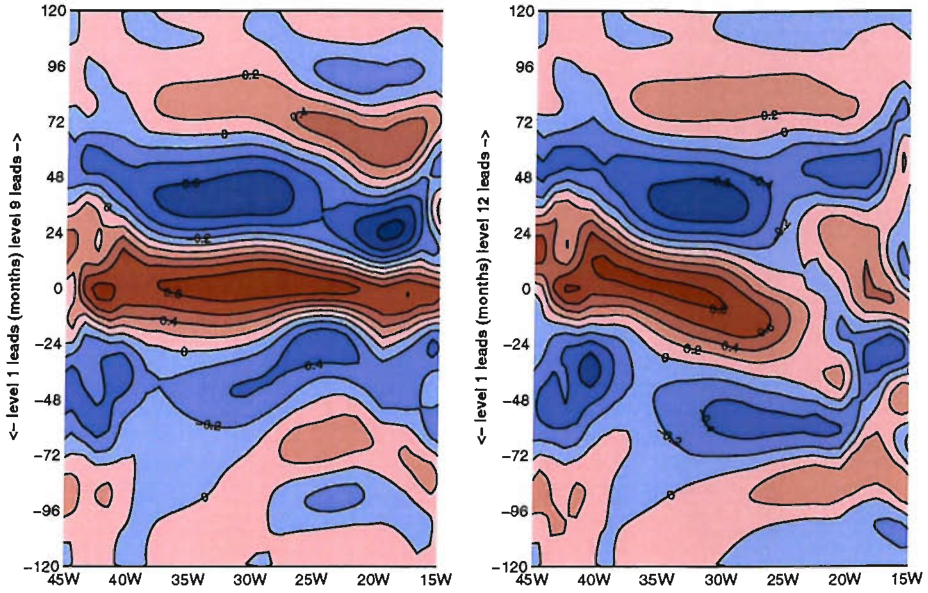

Figure 5.18: Lagged correlation - longitude diagrams at 49.5°N between surface temperature anomalies and temperature anomalies at 222.5 m (*left*) and at 610 m (*right*). *Contour intervals are every 0.2. The 99% significance level is 0.25.*

by the downward sloping contours and decrease in the correlation coefficient to the east. This may be a real signal or may be a function of the filtering employed[4]. Below this depth there is no significant correlation to the surface signal.

[43] An alternative approach to the methods outlined above is through the use of Complex Empirical Orthogonal Function (CEOF) analysis (see Appendix B for further details). Ideally, the technique of CEOF analysis allows the isolation of a signal in time and space, unlike conventional EOF analysis. That is to say one can identify propagating signals at specific frequencies. Figure 5.19 shows the first mode, explaining 68% of the variance, of the depth integrated temperature over the upper 610 m. This mode clearly illustrates an eastward propagating feature along the boundary of the Subpolar Gyre. The time taken for the feature to propagate from the Grand Banks of Newfoundland in to the Iceland Basin, as indicated by the phase shift, is approximately 4 years. This propagation speed is consistent with our previous results.

[44] The propagation of density anomalies also carries with it a dynamical signal. Similar

---

[4] As we use a low-pass filter with a cut off frequency of 0.4 yr^{-1} the surface signature may still contain some higher frequency components. Ideally a decadal low-pass filter would be used, but the model run is of insufficient length.

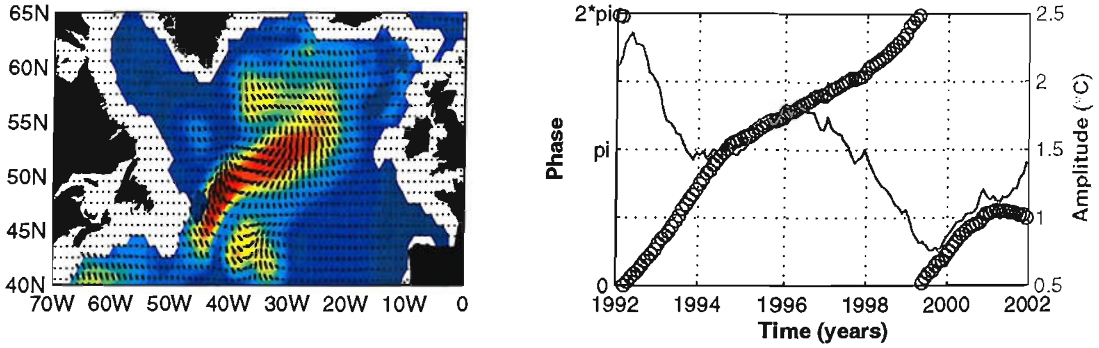

Figure 5.19: The first mode of a CEOF analysis of the depth integrated temperature over the top 610 m of the water column, *explaining 68% of the variance. Left, a spatial representation and right a temporal representation of the phase and magnitude associated with the first mode. See Appendix B for details on interpretation.*

analyses to that shown in Figure 5.19 reveal propagating signals in both the zonal and meridional velocity fields across the Subpolar North Atlantic Ocean. This dynamical signal may in fact influence the evolution of the Subpolar Front outlined in Section 5.2. Figure 5.20 shows a lagged correlation analysis between the time-series of latitudinal position of the Subpolar Front at various degrees of longitude. Each time-series of latitudinal position is correlated to the most westerly time-series, revealing an eastward propagation in the shape of the front. The speed at which the adjustment to the shape of the front propagates is $\sim 1.7\ cms^{-1}$, as one would expect a similar order of magnitude to the propagation of the density anomalies.

[45] In summary, we have shown the existence of eastward propagating features in the relatively short ECCO model run. Previous model studies have also revealed similar characteristics, but only at the surface (Krahmann *et al.*, 2001, Cooper and Gordon, 2002, Sinha *et al.*, 2004). From the analysis of unfiltered Hovmöller diagrams there is evidence of variable propagation speeds of anomalies over a range of depths, with possible communication across depths as suggested by Sutton and Allen (1997). From low-pass filtered data we find a positive large-scale temperature anomaly that formed in the western Subpolar North Atlantic and propagated to the east into the Iceland Basin by the mid-to-late 1990s coinciding with the change in circulation (*First Mode*, Section 5.3) and the westward shift in the Subpolar Front (Section 5.2). An upper ocean CEOF analysis shows a somewhat localised response along the Subpolar Front compared to previous studies;

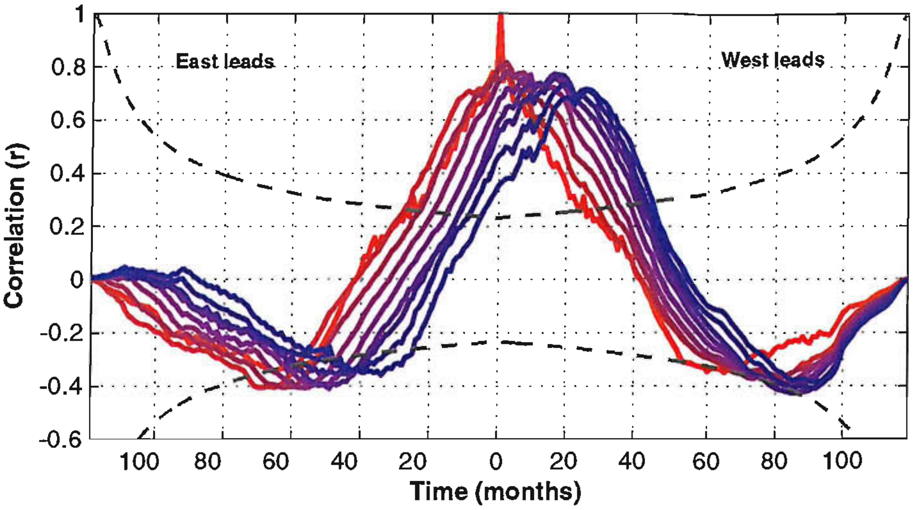

Figure 5.20: Propagation of frontal characteristics. *A lagged correlation analysis between the latitudinal positions of the Subpolar Front at various degrees of longitude with respect to the most westerly point. Curves red through to purple indicate longitudes 42.5° W through to 25° W in 2.5° increments. Note as the correlation is with respect to the most westerly time-series it has a correlation of 1 at lag 0. 99% confidence intervals are given by the grey dashed lines.*

the region in which propagation is observed in ECCO is solely along the Subpolar Front with little or no signal in the Gulf Stream region to the south.

[46] One of the principal mechanisms associated with propagating anomalies observed in previous studies is the generation through anomalous heat fluxes. We suggest this is probably not a significant mechanism in the case of the generation of anomalies in ECCO. Anomalies in both temperature and salinity propagate in unison and over the entire upper ocean, negating this mechanism. If the anomalies were solely a function of anomalous heat fluxes then there would be little change in the salinity associated with these features. Krahmann *et al.* (2001) propose two basic mechanisms for the generation of temperature anomalies: the local formation by anomalous heat fluxes, as mentioned, and the heat transport divergence and subsequent advection. They suggest from their modelling study that these mechanisms can be partitioned: two thirds attributed to heat transport divergence and one third to anomalous heat fluxes. It is precisely because the low-frequency large-scale anomalies are deeper reaching than the surface layers of the ocean that we suggest the principal mechanism in this case to be variations in heat transport resulting from fluctuations in the large-scale circulation. For the case of the higher frequency anomaly propagation in the surface layer that we saw in the unfiltered

data, heat flux anomalies may play a role.

[47] Evidence of these anomalies in nature is sparse. Evaluation of satellite products (Topex/Poseidon and ERS gridded altimeter data and SST data from the AVHRR) is inconclusive and does not show the clear propagation apparent in the analysis conducted by Sutton and Allen (1997). In addition to model simulations that exhibit strong eastward propagation in response to idealised NAO-like forcing, Krahmann *et al.* (2001) present simulations with realistic forcings and results from observational data that are less convincing. Some of the observational data even appear to exhibit westward (*upstream*) propagation of anomalies. As the ECCO model assimilates SSTs and temperature and salinity characteristics from hydrographic sections one would expect a truer representation of the ocean than model alone. The model has realistic forcings and exhibits a clear propagation signal over the entire upper ocean and not just as a surface phenomenon. Although these features may be unrealistic it is still important to document them as they consistently occur in General Circulation Models in some form or another.

[48] As we previously alluded to, the generation of anomalies may in some way be linked to interannual variations in the *First Mode* (Section 5.3). It is conceivable that the Sverdrup-like response of the ocean to the atmospheric forcing could produce such anomalies via variations in the northward heat transport west of the MAR and may account for the large-scale temperature anomalies observed. The general pattern in the northward heat transport to the west of the MAR (Figure 5.6) is qualitatively similar to the pattern of temperature anomalies in the western portion of Figure 5.17, but further analysis is required to confirm and quantify this mechanism. Ideally, due to the nature of the anomalies, a longer model run is required.

[49] In their idealised experiments Krahmann *et al.* (2001) found that specific NAO forcing periods comparable to the cross-basin advective timescales acted to maintain the anomalous features. The ocean advection transports the anomaly created in the first half of the pathway to the second half of the pathway in exactly the time which the external forcing switches from one state to the other, thus re-enforcing the remotely created anomaly. In the ECCO model run we find that the locally generated anomaly in 1992/3 propagates into the Iceland Basin as the phase of the NAO switches from a positive to a negative phase, thus maintaining the anomaly. This is illustrated by the anomalous heat transport

northward to the east of the MAR (Figure 5.6). Again in 1999/2000, when the NAO is in a positive phase and there is an anomalous heat transport to the west of the MAR, there are the beginnings of a positive temperature anomaly. However, the phase of the NAO changes within two years and therefore no coherent propagation is observed.

[50] The mechanism proposed by Cooper and Gordon (2002), that Labrador Sea Water production plays a dynamical role in the eastward propagation of temperature anomalies, may just be incidental to the anomalous heat transport, as both are influenced to some degree by the phase of the NAO. However, there may also be a coupled effect between these two mechanisms that needs to be further investigated. Cooper and Gordon suggests that the increased production of Labrador Sea Water results in positive SST anomalies off Newfoundland. The idea is that the increased density gradient between the Labrador Sea Water and the waters of Subtropical origin to the south act to increase the strength of the NAC therefore inducing SST anomalies along the mean pathway. Bellucci (2004) conversely suggest that it is the periodic sign reversal of SST anomalies that modulates the formation of Labrador Sea Water. Sinha *et al.* (2004) stress that similar eastward propagation is found at gyre boundaries in the Pacific Ocean, where deep convection such as that observed in the Labrador Basin is absent. In ECCO we find little evidence of eastward propagation of anomalies from the Labrador Basin. It must be noted, however, that the time-series of the ECCO model run is insufficient to prove or disprove the existence of the mechanism proposed by Cooper and Gordon (2002).

[51] The question also remains of what type of sampling strategy is best to quantify these propagating features. The inherent problem with using the climatological pathway of the NAC or a particular line of latitude to sample along is that the pathway of the NAC is highly variable and thus the pathway of the anomalies will change. If the anomalies are a dynamical part of the changes in the position of the pathway of the NAC this may not be such of an issue. The use of the technique of CEOF analysis in place of the traditional tool of Hovmöller diagrams appears to allow a quantitative better description of propagating features. However, it is still useful to run animations to confirm the results of any such analysis.

5.6 Discussion of results

[52] Previous analysis of satellite altimeter data (Chapter 3) revealed a decrease in the amount of eddy energy in the Newfoundland Basin suggesting that the strength of the NAC had decreased over the study period. It is also evident from analysis of ECCO that there is a weakening of the NAC and more generally the Subpolar Gyre. This may be a true representation or just a coincidental artifact of both data as they are not completely independent. The decline of the Subpolar North Atlantic Circulation over the 1990s has also been recently confirmed by Häkkinen and Rhines (2004), albeit with the same altimeter data. The model also appears to exhibit greater interannual variability at the *Northwest* Corner than observed in the satellite data. This variability is primarily in the position of the *core* of the NAC, defined by the maximum flow, although this is not reflected to the same degree in the positional variability of the isotherms. The difference between position of the *core* and isotherms appears to be related to a broadening of the NAC, and hence isotherms, to the northeast of the Flemish Cap the over the model run (Figure 5.2), compensating the southeasterly shift in the *core*.

[53] The reduction in strength of the Subpolar Gyre is primarily explained by the low-frequency fluctuations in the baroclinic structure of the western Subpolar North Atlantic. In the *Second Mode* we find a reduced doming of the isopycnals in the central Labrador Sea over the period of the model run. The observed decline of the gyre strength, $\sim 10\ Sv$, is consistent with estimates reported by Häkkinen and Rhines (2004), who used altimeter data to derive geostrophic velocities. However, they find the majority of the change to occur in the Irminger Basin.

[54] Seasonal-to-interannual variability in the horizontal circulation is largely attributed to the instantaneous response of the ocean to changes in the wind forcing as presented in a modelling study by Eden and Willebrand (2001). Our result is, unsurprisingly, in agreement with that presented by Eden and Willebrand as the atmospheric forcing is independent of the model physics used in an OGCM. They concluded that the increased presence of the saltier waters, associated with the NAC in the eastern Subpolar Gyre and along the Reykjanes Ridge, can be attributed to a Sverdrup response to the change in the wind stress. This response is also thought to include a south-eastward shift of the NAC in the western Subpolar North Atlantic (Bersch, 2002). However, Bersch's observation is

contrary to findings from satellite derived eddy kinetic energy inferences (Section 3.4.1). In 1996 there is very little evidence of a shift in observed eddy kinetic energy front found in the Newfoundland Basin. This is also apparent in the difference between drifter trajectories in NAO$^+$ and NAO$^-$ years, presented by Flatau *et al.* (2003) (*see their Figure 10*), where stronger northward flow is observed at the Flemish Cap in the NAO$^-$ years. ECCO, on the other hand, does exhibit the southeastward shift of the NAC, however, the shift persists over the course of the model run and does not exhibit an NAO-like behaviour. This may indicate that changes in the Newfoundland Basin may not just be a function of the *First Mode*. Indeed, Lu and Stammer (2004) suggest that in western boundary currents and at high latitudes there is a deviation from the simple Sverdrup balance. They find that the bottom pressure torque, lateral friction and nonlinear advection terms become increasingly important factors in determining the mean circulation.

[55] Flatau *et al.* (2003) also note that the interannual variations observed in the Subpolar Gyre reveal similar patterns to those exhibited on seasonal time scales; i.e. in summer months there are weaker westerly winds, similar to those of NAO$^-$ years and in winter months stronger westerly winds, as in NAO$^+$ years. They suggest, from drifter data, that there is a spin up of the Subpolar Gyre in NAO$^+$ years and a spin down in NAO$^-$ years. The *First Mode* in our analysis would suggest this as the case is the circulation anomaly presented in Figure 5.5 would act to increase/decrease the transport along the gyre boundary. However, superimposed on this short-term variability is a long-term trend in the strength of the circulation influenced by the baroclinicity of the Subpolar Gyre.

[56] In addition to explaining the seasonal-to-interannual changes in the circulation the *First Mode* presented in Section 5.3 also provides a feasible mechanism for the observed generation and subsequent propagation of temperature and salinity anomalies in the ECCO model. There is a strong similarity between the *First Mode* of the MCA and the *Inter-Gyre Gyre* mechanism proposed by Marshall *et al.* (2001). However, in our analysis the anomalous circulation extends from the intergyre zone further into the Subpolar Gyre than in the schematic by Marshall *et al.*. They predicate that the Inter-Gyre Gyre mechanism characterises a strongly damped standing wave oscillator, but note that superimposed on this feature will be advection by the mean currents, namely the NAC.

[57] Previous studies have suggested that the propagation of surface temperature anoma-

lies has been observed along the entire length of the Gulf Stream - NAC pathway (e.g. Sutton and Allen, 1997, Krahmann *et al.*, 2001). We find that the propagation of anomalies is restricted to the Subpolar and intergyre region as it appears to be primarily a function of the variable wind forcing in this region as outlined above. The idea of Marshall *et al.* (2001), that the superimposition of advection by the mean currents on *oscillations* in the Subpolar Front, is consistent with that observed at depth in ECCO, although not in the surface layers. This mechanism would require communication in the vertical to explain the low-frequency propagation observed.

[58] There may also be a natural forcing frequency to the system. Krahmann *et al.* (2001) illustrate that propagating anomalies exist only under certain forcing frequencies. For example: the positive temperature anomaly found in the Newfoundland Basin in 1993 (Figures 5.17 and 5.19) propagates eastward at such a rate that it enters the Iceland Basin to coincide with a switch in the phase of the *First Mode* in 1996. During this period, as we have previously seen, there is a anomalous northward heat transport to the east of the MAR (Figure 5.6), thus re-enforcing the observed anomaly.

[59] Bellucci (2004) also attributes anomalous wind forcing to a departure of the isotherms from climatological mean pathway of the Subpolar Front generating the afore mentioned SST anomalies. Bellucci suggests that there is a delayed displacement of the front which is likely to explain the eastward propagation of the large amplitude SST anomalies in the vicinity of the NAC. This is consistent with the evidence of propagating frontal characteristics presented in Figure 5.20.

[60] Sutton and Allen (1997) suggest that the slow propagation of oceanic anomalies compared to the atmospheric dynamical timescales may allow a measure of predicability in the system. As the temperature anomalies observed in ECCO are distributed over the entire upper ocean, seasonal dampening will not have as great an impact as it would on surface anomalies alone. This would allow the persistence of anomalies over several years and thus a possible degree of predicability. Studies such as that by Czaja and Frankignoul (1999) have suggested that SST anomalies can contribute to atmospheric circulation variability. It is also interesting to note that previous studies into propagating features have only been performed with coarse resolution models, in which the currents and the tracer fields are more diffuse. Increasing the resolution of the model grid, to include eddy dynamics, may

well change the characteristics of the observed anomalies.

5.7 Summary

[61] It has been demonstrated that on seasonal time scales the leading mode of variability in the horizontal circulation reveals a Sverdrup-like response to the variable wind forcing. An increase in the winter-time pressure gradient between Iceland and the Azores leads to an anomalous anti-cyclonic circulation centred on the intergyre zone. This effectively increases the northward transport to the west of the MAR in the NAC and leads to an anomalous transport southward to the east. On interannual time scales this anomalous circulation feature exhibits similar spatial characteristics. In the NAO$^-$ years of 1995/6 and 2000/1 we see an anomalous cyclonic transport, centred on the intergyre zone and the Subpolar Front, reducing the strength of the NAC and increasing transport to the east of the MAR. On interannual time scales this mechanism results in an anomalous heat transport northward to the east of the MAR (Figure 5.6b) and conversely a decrease in the heat northward heat transport to the west. However, the interannual variations in heat transport are not observed on seasonal time-scales as result of the much stronger signal in seasonal heating and cooling.

[62] Associated with these changes in circulation and heat transport are lateral shifts in the position of the Subpolar Front. In NAO$^-$ years the anomalous cyclonic circulation generated by a weakening pressure gradient prevents the eastward spreading of Subpolar Waters into the Iceland Basin. Bersch (2002) suggests that these waters follow a more southerly trajectory to the west of the MAR and hence account for variations in the position of the Subpolar Front. The subsequent change in the shape of the gyre is nicely illustrated in the qualitative lagrangian experiments presented in Section 5.4.

[63] We also find that the long term weakening of the horizontal circulation is not reflected in the atmospheric forcing. The decrease, primarily occurring in the Labrador Basin, appears to be linked to the change in the baroclinic structure in the Subpolar Gyre. Slumping of the isopycnals in the Labrador Sea, possibly connected to the weakening of winter-time deep convection over the model run, leads to a gain in steric height and subsequent spin down of the gyre.

[64] Analysis of heat content changes in ECCO are consistent with changes observed by Reverdin *et al.* (1999). In addition we have quantified the sources of the observed heat gain in the Labrador region between the well known phase reversal in the NAO-index between 1995 and 1996. We also note that a similar phase reversal between the NAO$^+$ years of 1999 and 2000 and the NAO$^-$ year of 2001 does not induce changes in the oceanic advection of heat into the region as in 1996.

[65] Coupled to the changes in the Subpolar circulation outlined above are the variations in the export of intermediate and deep waters from the Labrador Basin. Using lagrangian diagnostics we identify changes in the export pathways under different circulation regimes. Although there is the suggestion of increased export southward to east of the MAR under an NAO$^+$ state, the primary change occurs to the west where a larger proportion of the intermediate and deep waters escape southward under NAO$^-$ conditions.

[66] The results from ECCO have also provided further evidence for the existence of eastward propagating anomalies in the North Atlantic. The anomalies observed are of the $O(2°C)$ and $O(0.3)$ in salinity and propagate at speeds of the $O(2\ cms^{-1})$, much slower than surface velocities. These anomalies have only previously been observed as surface features and not over the entire upper ocean as in this study.

[67] This work illustrates that although we can identify leading modes of variability in the system there are no simple relationships between forcing mechanisms and changes in the circulation, heat transport, or position of the Subpolar Front. There are clear differences between the NAO$^+$ years of the early 1990s and the period after the sudden reversal of the NAO-index in 1996, similar changes between the NAO$^+$ years of 1999 and 2000 and the NAO$^-$ year of 2001 are characteristically different. By extending the length of the model run, assimilating the increasing number of observations available, we would be able to further quantify the large-scale interannual changes and in particular the effect of sudden reversals in the phase of the NAO.

Chapter 6

Meridional Overturning Circulation Variability

6.1 Introduction

[1] The meridional overturning circulation (MOC) in the North Atlantic describes the northward transport of relatively warm saline surface waters poleward, the subsequent sinking to depth and return equatorward as deep and intermediate waters (Macdonald and Wunsch, 1996). Variations in the overturning circulation may therefore have an impact on the northward heat transport and horizontal circulation of the ocean. To this end it is of significant importance to understand the role of the MOC and its variability in the climate system.

[2] The downwelling limb(s) of the MOC is generally described as the localised sinking occurring at high latitudes due to extreme conditions (Gill, 1982). Mechanisms for the transfer of surface waters to depth have been recently examined by Marotzke and Scott (1999) and Spall and Pickart (2001), and have become a topical area of research. Spall and Pickart (2001) suggest that the dominant mechanism for the downwelling is convective mixing near steep topography, other possible mechanisms being: Ekman convergence, baroclinic instability of convective sites and subduction at colliding boundary currents. Dense water formation has in the past been linked to the strength of the downwelling limb(s) of the MOC. However, Mauritzen and Häkkinen (1999) suggest that there is evidence that it may not be as tightly linked as previously thought, allowing for possible changes in the volume of particular water masses.

[3] There have been several observational efforts, particularly in the Subtropical North Atlantic Ocean, at determining the northward heat transport (e.g. Hall and Bryden, 1982, Macdonald and Wunsch, 1996, Lorbacher and Koltermann, 2000). However, there are large uncertainties in measuring the overturning circulation and temporal evolution of northward heat transport from hydrographic sections. This is in part due to the large annual cycle and the asynoptic nature of cross basin hydrographic surveys. This issue is currently being addressed through the initiation of a long-term monitoring program focussed on 26.5°N (Marotzke *et al.*, 2002).

[4] It remains to be seen how representative a single hydrographic section is of the northward heat transport. It is important to understand the high-frequency fluctuations of the system if we are going to use such observations to formulate an estimate of the long term mean oceanic fluxes. In an ocean model intercomparison Böning *et al.* (2001) found that using *relatively weak* wind forcing they observed an annual amplitude of 0.4-0.5 *PW* in the meridional heat flux at 25°N. Although it is still unclear how realistic the northward heat transport in Ocean General Circulation Models is, they do provide a useful tool in diagnosing sources of variability.

[5] There have been several previous studies linking much of the variability in the North Atlantic Ocean with the North Atlantic Oscillation (NAO; Section 2.5). As the dominant mode of atmospheric variability, the dynamic phase of the NAO is in unison with the position of the zero in the curl of the wind stress. Positive (negative) anomalies in the wind stress curl lead to an anomalous divergence (convergence) in the surface layer. This gives rise to what is termed Ekman suction, upwelling, and Ekman pumping, downwelling.

[6] Several mechanisms have been identified for the variability of the overturning circulation in the North Atlantic Ocean (Beismann *et al.*, 2002); the fast barotropic response to the wind stress (Hall and Bryden, 1982, Eden and Willebrand, 2001) and the delayed baroclinic response to the wind stress (Eden and Willebrand, 2001, Gulev *et al.*, 2003), heat flux anomalies (Gulev *et al.*, 2003) and convective activity in the Labrador Sea (Eden and Willebrand, 2001). Using the ocean state estimation produce by ECCO (Stammer *et al.*, 2002, Köhl *et al.*, 2003) we describe various aspects of the overturning circulation and examine the relationship between the wind field and the MOC in Subpolar North Atlantic Ocean over the last decade.

6.2 Meridional Overturning Circulation

[7] The mean meridional overturning streamfunction spanning the entire model period is contoured for the North Atlantic between 20°N and 80°N in Figure 6.1a. The average overturning in the North Atlantic is 18 Sv, of which 3 Sv is upwelled in the *intergyre zone* (40°N to 50°N) into the upper ocean. The strength of the overturning in the Subpolar North Atlantic Ocean appears to vary both on seasonal and interannual time scales. The temporal variability of the overturning strength at 50°N and at a depth of 1160 m is depicted in Figure 6.1b.

[8] The amplitude of the seasonal harmonic at 50°N, 1160 m is of the order 1.8 Sv peaking in May. Although the time series has a variance of around 4 Sv there are extreme events present when the overturning decreases by approximately 8 Sv in the order of months. The overturning in the Subpolar Gyre at 55°N has a very similar temporal profile with a seasonal amplitude of 1.4 Sv and with no significant difference in the timing of the maximum.

[9] The mean state of the MOC differs from model to model, as it is dependent upon the numerics and forcing employed (Böning *et al.*, 2001, Beismann *et al.*, 2002). For example, Mauritzen and Häkkinen (1999), in diagnosing the relationship between dense water formation and the overturning circulation, present an overturning circulation that is distinctly different in spatial characteristics to that of the ECCO model. The maximum overturning in their model is observed at around 35°N, some 20°of latitude to the south of where we find the maximum occurring in the ECCO model (cf. Figure 2 from Mauritzen and Häkkinen (1999)).

[10] The latitude at which the maximum overturning occurs varies over the model run (Figure 6.1c). Generally we see a weakening of the overturning in the Subpolar North Atlantic and a strengthening in the Subtropical North Atlantic during the winter months. This is characterised by a shift in the position of the maximum overturning from 50°N southward towards 20°N, our sample domain boundary. However, in 1995/6, a winter with a low NAO-index, the strength of the overturning remains relatively robust in the Subpolar North Atlantic. This is illustrated by the persistence of the maximum overturning at 50°N. The depth at which the maximum overturning is observed is constant throughout

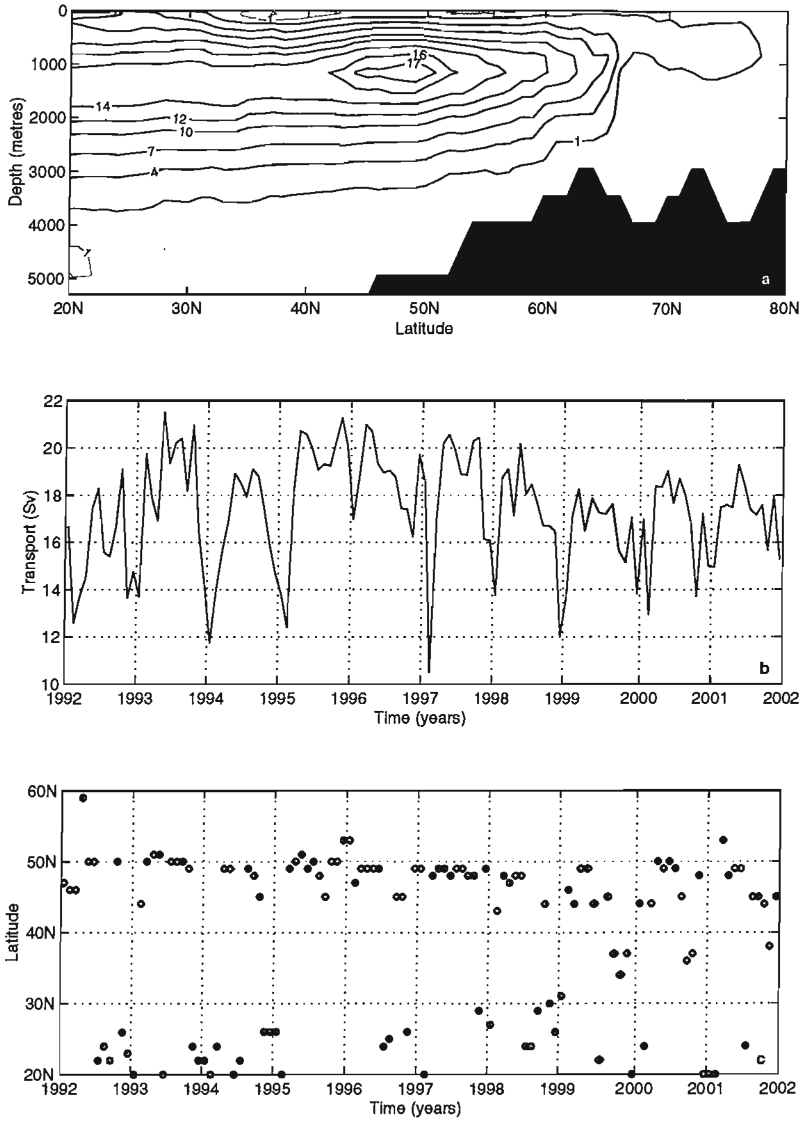

Figure 6.1: *a) Meridional Overturning Circulation for the North Atlantic Ocean between 20° N and 80° N. The overturning streamfunction is contoured irregularly; black contours represent a positive overturning and the grey a negative overturning. b) Time series of the overturning streamfunction at 50° N and at 1160 metres depth. c) Time series of the latitude at which the maximum overturning between 20° N and 80° N occurs between 1992 and 2002.*

the model run, between levels 14 and 15 of the model, corresponding to depths of 1160 m and 1542.5 m respectively.

[11] Figure 6.1c can be explained, in part, by the annual cycle present in the wind field. Figure 6.2 depicts the monthly mean meridional transport anomalies across a particular line of latitude in the Subtropical and the Subpolar North Atlantic Ocean. In the spring there is a positive contribution to the northward mass transport in the Subpolar region,

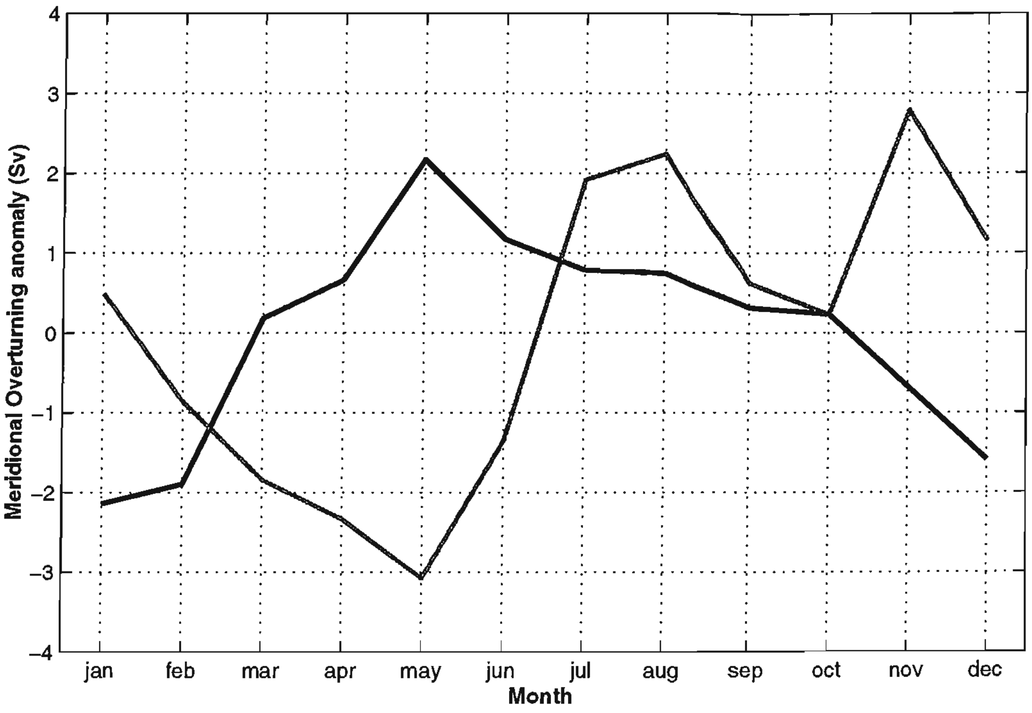

Figure 6.2: Annual cycle of the monthly mean meridional overturning transport anomalies above 1160 *m* for 25°N (grey) and 50°N (black).

whereas this contribution is negative in the Subtropics. The result is a maximum in the overturning situated in the Subpolar North Atlantic Ocean. The converse is true in early winter. However, when there is a weakening of the annual harmonic, e.g. in 1995/6 and more generally in NAO$^-$ years, the anomalous mass transport is insufficient to reduce the overturning in the Subpolar North Atlantic to a level lower than that observed in the Subtropics. The suggestion is, therefore, that the seasonal-to-interannual variability in the MOC can be primarily attributed to fluctuations in the Ekman transport. In addition the seasonal differences between the transports in the Subtropical and Subpolar North Atlantic will result in anomalous upwelling (downwelling) in the inter-gyre zone. These ideas will be further developed in Section 6.4.

6.3 Components of the MOC

[12] The overturning circulation can be separated into three components: barotropic, baroclinic and Ekman. The *barotropic* or *external* mode is given by:

$$\Psi_{bt}(y,z) = \int_{-H}^{\eta} \int_{0(y)}^{L(y)} \overline{v}(x,y)dzdx. \tag{6.1}$$

where $\overline{v}$ is the barotropic velocity component. This mode represents the contribution to the overturning by the depth integrated transport in a basin with realistic topography. Figure 6.3 shows the annual average overturning circulation attributed to the external mode for the Subpolar region. There appears to be relatively little contribution to the overturning circulation by the external mode. Further to the south, in the Subtropical North Atlantic Ocean, there is a large positive contribution to the overturning circulation (not shown). This overturning, of $O(20Sv)$ is associated with the transport in the Gulf Stream along the relatively shallow topography northward up to Cape Hatteras. The external mode contribution to overturning in the Subpolar North Atlantic Ocean appears to decrease over the period of the model run, most probably related to the spin down of the horizontal circulation presented in the previous chapter.

[13] Figure 6.4 shows the first two leading modes of an Empirical Orthogonal (EOF) analysis (see Appendix B for further details) of the external mode, which account for over 50% of the observed variability. The first mode has a Centre of Action (CoA) located between 45°N and 50°N. This mode would be consistent with a contribution to the overturning from the NAC. Between 45°N and 50°N the NAC is observed to hug the topographic contours of the the Grand Banks of Newfoundland (Kearns and Rossby, 1998). During the first few years of the model run the pathway of the NAC was further to the west over shallower topography, thus contributing more to the external mode as reflected in the associated Principal Component (PC). There is also a strong seasonal signal in the first mode that may be related to the wind forcing of the horizontal circulation seen in Figure 5.5.

[14] The density driven component of the overturning circulation, or *baroclinic* mode, is given by:

$$\Psi_{ther}(y,z) = \int_{-H}^{\eta} \int_{0(y)}^{L(y)} v_{therm} dzdx \tag{6.2}$$

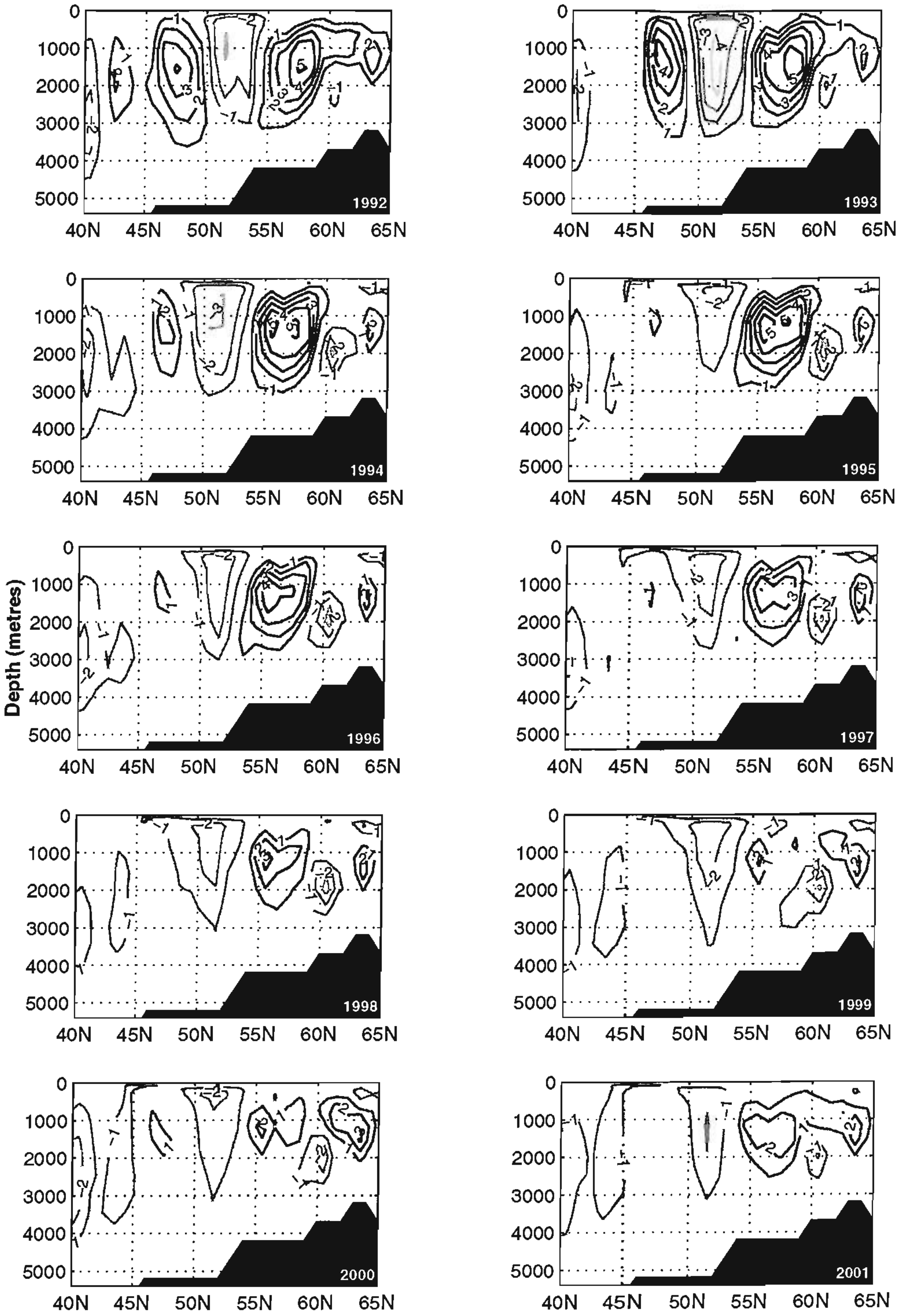

Figure 6.3: Annual mean overturning streamfunction for the barotropic or *external* mode. *Contour intervals are every 1 Sv. Positive contours signify a positive overturning in an clockwise sence as viewed.*

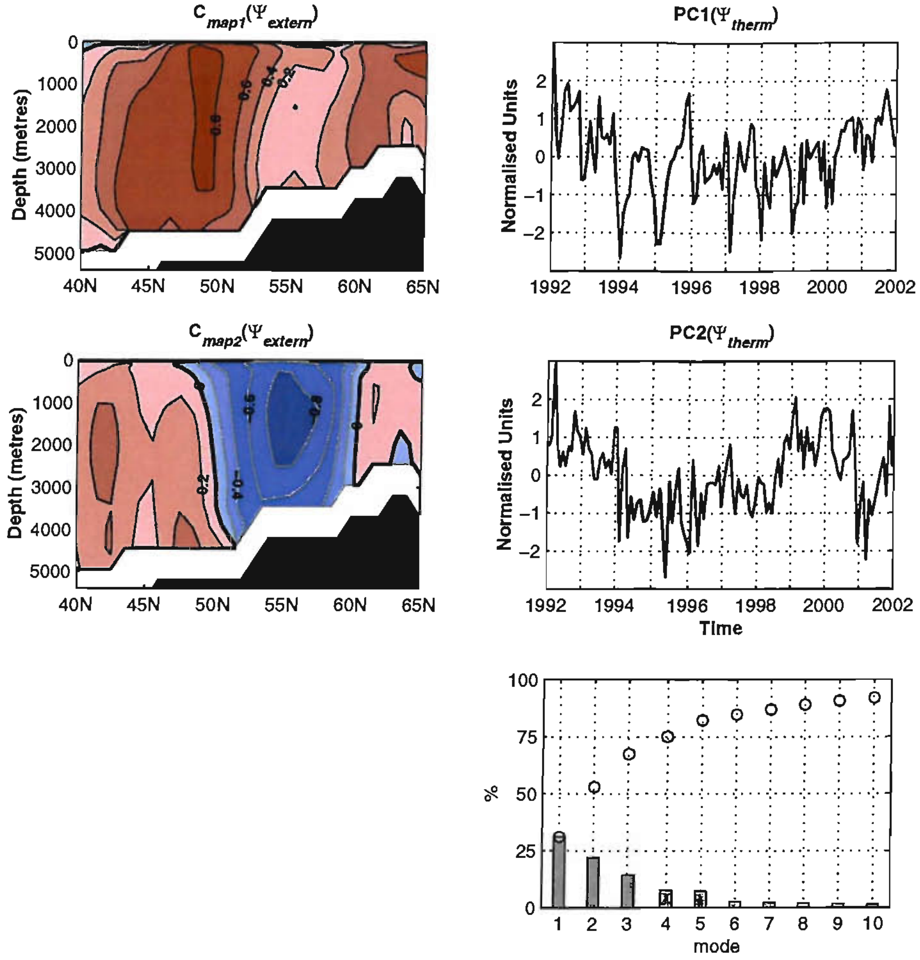

Figure 6.4: Spatial maps and Principal Components (PC) for the first two modes of the EOF analysis of the barotropic component of the MOC. The spatial patterns are presented as correlation maps, contoured with an interval of 0.2. The percentage of variance explained is also shown for the first ten modes.

where v_{therm}, the thermal wind component of the meridional velocity is given by:

$$v_{therm}(x, y, z) = -\frac{fg}{\rho}\int_{-H}^{z}\frac{\partial\rho}{\partial x}dz, \tag{6.3}$$

where f is the coriolis parameter, g is gravity and ρ is the density. As one can see from Figure 6.5 it is the density structure that sets the time-mean structure of the MOC in the Subpolar North Atlantic Ocean.

[15] An EOF analysis of the baroclinic contribution to the overturning circulation is also performed and shown in Figure 6.6. The PC of the first mode, contributing close to 50% of the observed variability, illustrates the difference in nature between the baroclinic mode and the external mode. Variations in the overturning, due to changes in the density

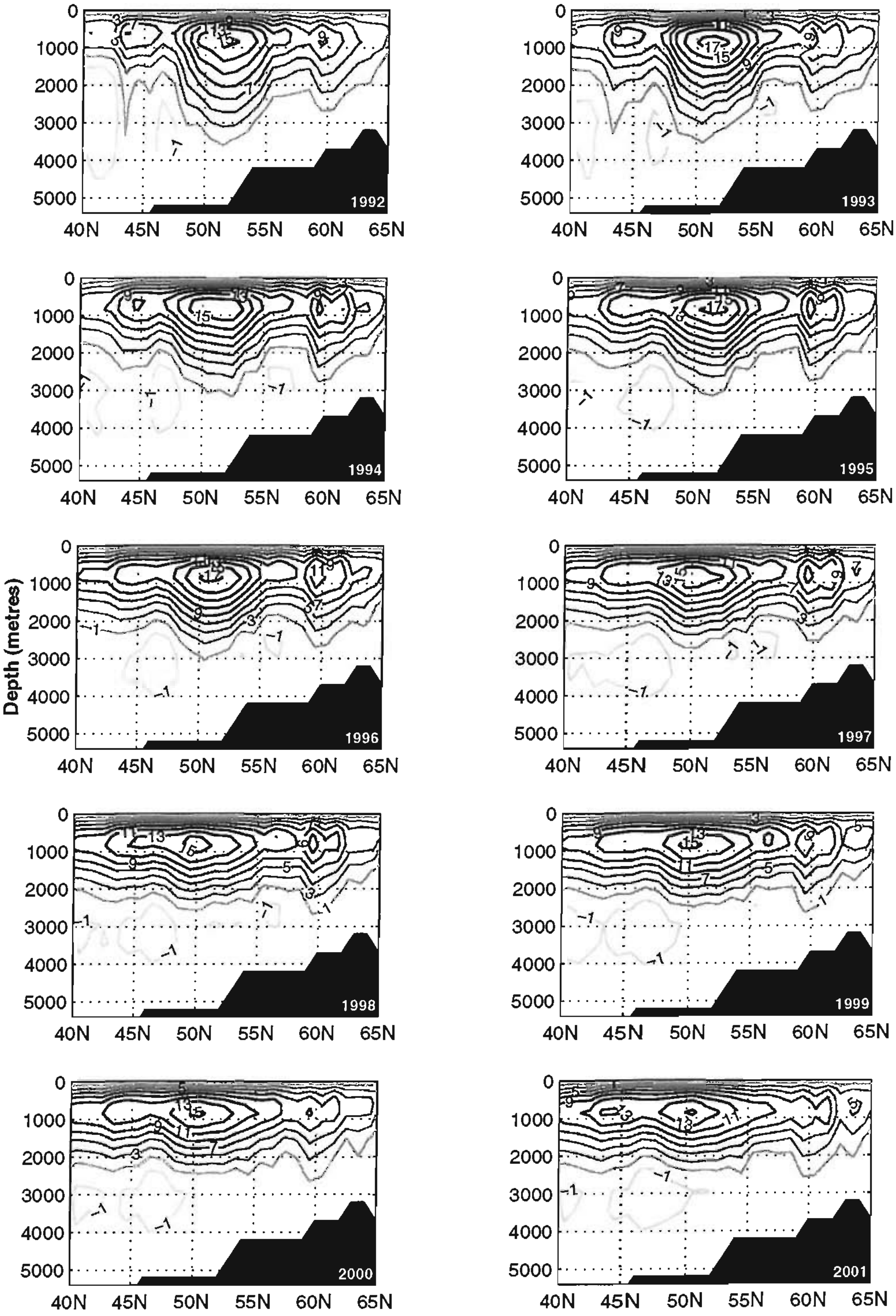

Figure 6.5: The annual mean baroclinic component of the overturning streamfunction. *Contour intervals are every 2 Sv. Positive contours signify a clockwise overturning as viewed and negative contours an anti-clockwise overturning.*

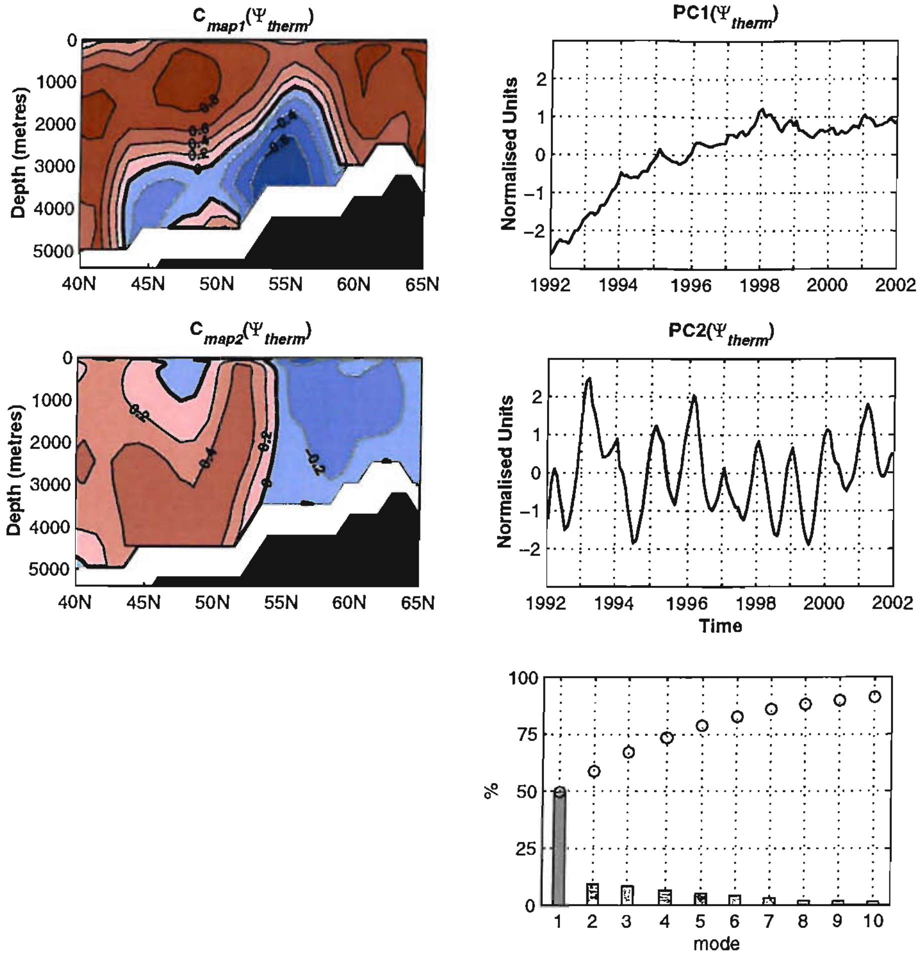

Figure 6.6: Spatial maps and Principal Components (PC) for the first two modes of the EOF analysis of the baroclinic component of the MOC. The spatial patterns are presented as correlation maps, contoured with an interval of 0.2. The percentage of variance explained is also shown for the first ten modes.

structure, are on greater than annual time scales. The first mode represents a shallowing of the overturning cell and the southward movement of the location of the maximum over the period of the model run. This is also apparent in the series of annual mean plots of the baroclinic component in Figure 6.5. Additionally, there is a small seasonal signal present in the second mode, though only explaining around 10% of the variability. The spatial pattern of this mode represents an anomalous downwelling/upwelling centred on 54°N and may be linked to water mass transformation through seasonal heat flux forcing in the Subpolar Gyre and in particular the Labrador Sea.

[16] The final contribution to the overturning circulation comes from the Ekman transport

and is expressed by:

$$V_{ek}(x,y) = -\int_{0(y)}^{L(y)} \frac{\tau_x(x,y)}{\rho f(y)} dx \tag{6.4}$$

where τ_x is the zonal wind stress. An example of the Ekman contribution to the overturning is shown in Figure 6.7.The Ekman contribution to the overturning streamfunction is, by definition, confined to the surface layer. This requires, through the conservation of mass, the assumption of a depth independent return flow to ensure the net meridional transport is zero. However, this is not strictly true as there is also a contribution from the wind stress to the baroclinic transport (Hirschi *et al.*, 2003). While the divergence in the wind field, heat and fresh water fluxes set the long term circulation of the ocean one would expect the Ekman response to be reflected in the short term response of the overturning strength.

[17] An alternative approach to examining the MOC is to calculate the northward transport in density classes, therefore eliminating the barotropic mode. The overturning streamfunction becomes:

$$\Psi_\sigma(y,\sigma) = \int_{\sigma(min)}^{\sigma(max)} \int_{0(y)}^{L(y)} v(x,y,\sigma)\, d\sigma dx \tag{6.5}$$

The overturning streamfunction in both *z-level* and density space are similar (cf. Figure 6.8). There is a diapycnal transport of $O(2Sv)$ into the upper ocean between 40°N and 50°N, qualitatively similar to the *z-level* case (Figure 6.1a). The maximum overturning in the *z-level* is greater than that calculated using the σ method by a average of 2 Sv. However, on examination of the overturning strengths at 55°N in the Subpolar Gyre the reverse appears to be true, with the σ method greater by an average 3 Sv. Mauritzen and

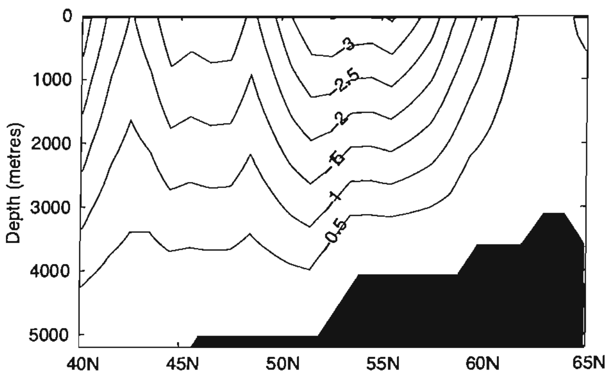

Figure 6.7: Ekman component to the overturning in the Subpolar North Atlantic calculated from the mean zonal wind stress over the entire model run. *Contour intervals are every 0.5 Sv.*

Häkkinen (1999) suggests that this may indicate that in the Subpolar Gyre water mass transformations are more likely to occur within a certain depth interval rather than as a shallow to deep overturning. In general using density classes to determine the overturning streamfunction we find that the strength of this overturning north of the Subpolar Front is on the whole stronger than to the south. This feature points towards strong diapycnal transport between depth levels in the intergyre zone.

6.4 Maximum Covariance Analysis of the MOC

[18] Using the method of *Maximum Covariance Analysis* (MCA) monthly fields of the curl in the wind stress and the meridional overturning circulation are analysed. The method of MCA identifies the closely coupled modes between two data fields (Björnsson and Venegas, 1997). This will allow us to explore the relative importance of the wind forcing on the variability of the MOC. A brief summary of this technique is outlined in Appendix B. The four leading spatial modes account for 95% of the total monthly variance of the ***combined*** signal. To assess the relative importance of each combined mode, the data are reconstructed (Equation B.5) and compared to the original data set. In Figure 6.9 the

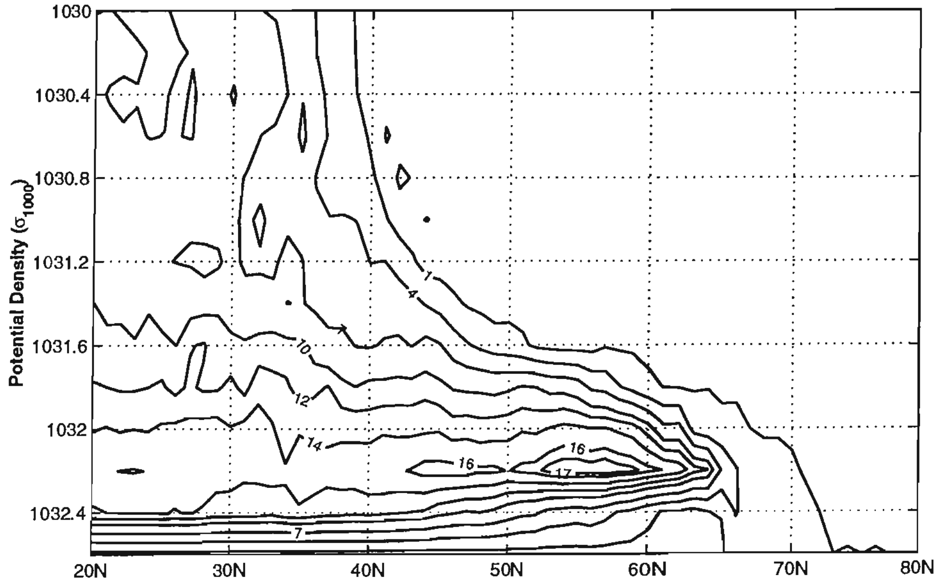

Figure 6.8: Meridional overturning streamfunction displayed in potential denisty space relative to 1000 ***m.*** ***Contour intervals are irregularly spaced.***

spatial maps of each field are shown for each mode as a homogeneous correlation map[1]. Also depicted in Figure 6.9 are the temporal signals, and the associated correlation, r, giving a measure of the strength of the coupling.

[19] As the two data fields used in this analysis are of different magnitudes, i.e. the MOC is of $O(10\ Sv)$ and the wind stress curl $O(10^{-7}Nm^{-3})$, it is necessary to normalise each data set prior to the analysis. This prevents one of the data sets, in this case the MOC, adding a bias to the covariance matrix used in the MCA.

[20] The first coupled mode explains a substantial proportion of the variance and is dominated primarily by the annual cycle. Upon removing the annual cycle prior to the analysis, the first two spatial maps remain relatively unchanged. The percentage of variance explained is still dominated by the first two modes, although now more evenly (50% and 35% respectively). We interpret this mode to describe the strengthening and weakening of the overturning circulation in the Subpolar North Atlantic in response to fluctuations in the north-south dipole structure in the curl of the wind stress. That is to say when the curl in the wind stress is anomalously negative over the Subpolar Gyre and anomalously positive over the intergyre zone, there is a strengthening of the overturning circulation. Projecting the first mode of the wind stress curl back on to the mean field allows one to gain an understanding of this dimensionless quantity. This mode represents an increase (decrease) in the pressure gradient between Iceland and the Azores. For example, in the winter of 1995/6 and to a lesser extent in the winter of 2000/1 the pressure gradient is reduced such that the associated overturning remains relatively robust, whereas during the other winter periods the strength of the overturning the Subpolar North Atlantic is reduced. Fluctuations in the pressure gradient are also clear on seasonal time scales. Just as there is a increase in the pressure gradient, and reduction in the overturning circulation, from an NAO$^-$ year to an NAO$^+$ year there is also an increase in the pressure gradient and decrease in the overturning circulation from the summer to the winter. There is a significant correlation of -0.75 between the winter-time NAO-index and intra-winter variations of $PC1(\Psi_{moc})$.

[21] The spatial pattern of $C_{map1}(\Phi_{moc})$ in Figure 6.9 is similar in structure to that of the Ekman contribution to the overturning circulation (see Section 6.3). The Centre of Action

---

[1] A spatial map of the correlation between the i^{th} principal component and the original data time-series at each grid point.

(CoA) of this mode is located to the north of the maximum in the overturning circulation (Figure 6.1a). Upon reconstructing the first mode of the overturning we find that 96% of the variance of the original time-series is explained at the CoA. This is equivalent to a variance in the overturning of up to 6 *Sv*. Furthermore, 95% of this variance can be attributed to the Ekman transport at this latitude with no significant lead or lag between the annual cycle of the two time-series (PC1 Figure 6.9 cf. Figure 6.11c).

[22] The second coupled mode is characterised by a dipole in the overturning circulation centred around 55°N. This is associated with an anomalous upwelling (downwelling) in response to a positive (negative) anomaly in the curl of the wind stress over the eastern Subpolar North Atlantic. The second mode essentially represents the change in overturning due to variations in the Ekman divergence. The spatial pattern in the wind field is similar to that described by Barnston and Livezey (1987) of the Eastern Atlantic Oscillation (EAO) and has a CoA over the southern Iceland Basin (55°N, 20°-to-35°W). Extending the latitude of the analysis southward to 20°N confirms this pattern (not shown here). The correlation between the PCs of the second mode and the EAO-index[2] is 0.50, significant at the 99^{th} percentile. The monopole-like feature in $C_{map2}(\nabla \times \tau)$, Figure 6.9, is manifested as a latitudinal shift in the zero of the wind stress curl when projected onto the mean field. For example, during the winters of 1997/8 and again in 2000/1 there was a southward shift in the zero of the wind stress curl associated with a positive anomaly in $C_{map2}(\nabla \times \tau)$, thus resulting in an anomalous upwelling in the Subpolar Gyre. Although only accounting for 29% of the total variance, this mode explains 57% of the variance in overturning at its CoA in the Subpolar Gyre region.

[23] The third and fourth modes in Figure 6.9, although describing only a small percentage of the explained variance, are still significantly correlated in time. The third mode exhibits seasonal fluctuations with a phase lag in the annual harmonic of around 1.5 months to that of the first mode. We note, however, that the third mode is unlikely to be an Ekman process as the centre of action is at around 3000 *m* in the central Subpolar Gyre. This mode may be characterised by the seasonal upwelling or downwelling along to topographic slopes of Greenland and to the south off the Newfoundland coastline.

---

[2] The EAO-index is taken from the NCEP-NCAR on-line teleconnection database. The correlation analysis was performed using only months where the EAO was found to be one of the leading modes of variability (September-April).

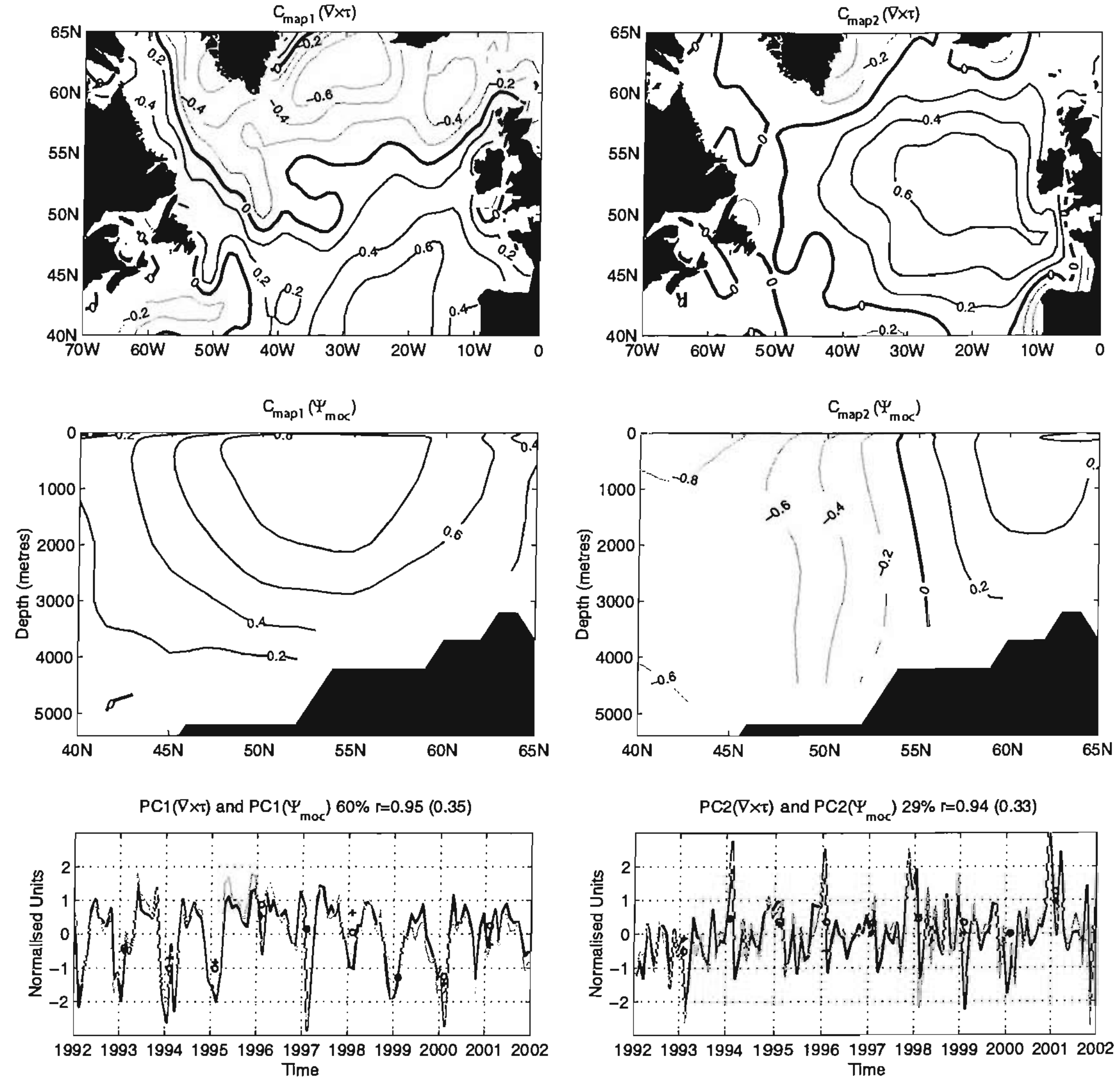

Figure 6.9: Spatial maps and Principal Components (PC) for the four leading modes of a MCA between the curl in the wind stress and overturning streamfunction. *The spatial patterns are presented as homogeneous correlation maps, contoured with an interval of 0.2. The % indicates the fraction of the variance explained by each combined mode, r is the correlation between the two PCs ($PC(\nabla \times \tau)$ is black and $PC(\Psi_{moc})$ is grey) and the values in the parentheses are the 99% significance levels for the correlations (determined by the autocorrelation of each PC, see Björnsson and Venegas (1997) for details).*

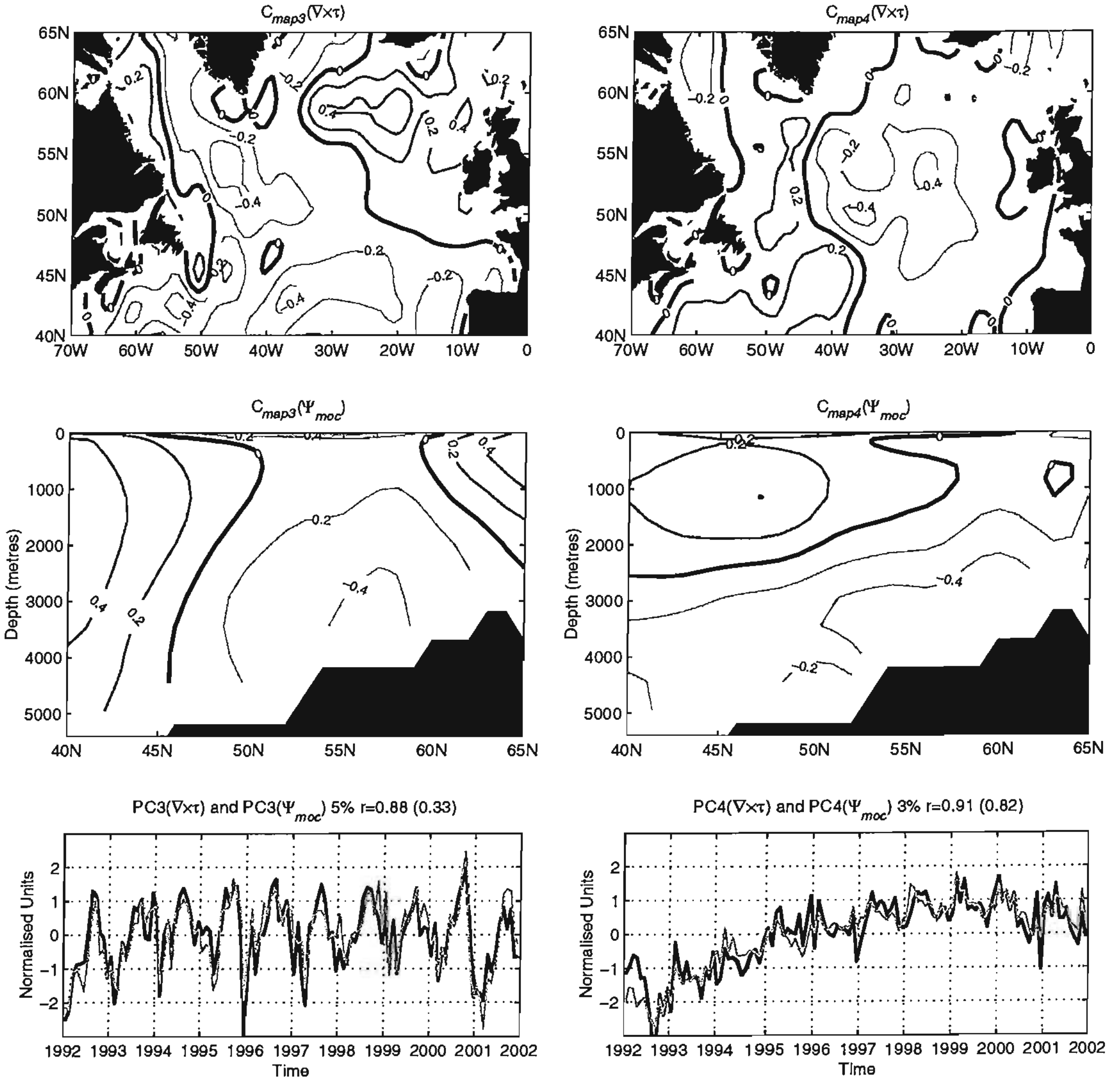

Figure 6.9: *contd.*

[24] The fourth mode of variability illustrates a trend in both the wind field and overturning circulation over the model run period. Taken literally this mode could be seen to characterise the gradual strengthening of a negative anomaly in the wind stress curl over much of the Subpolar North Atlantic and an anomalous downwelling. Coupled to this would be an increase in strength of the main overturning cell depicted in Figure 6.1a. It is unclear whether this statistical mode has any significant physical interpretation. No linear trend was removed prior to analysis. The spatial map of the wind stress curl shows very little correlation and the explained variance at the CoA is less than 40%. The map of the overturning, however, exhibits a more coherent pattern with up to 66% of the variance explained at the CoAs. This mode of variability is also present in the baroclinic contribution to the overturning with similar spatial patterns and PCs (cf. PC4 Figure 6.9 and PC1 Figure 6.6).

[25] Using hydrographic measurements along the WOCE AR2 line Lorbacher and Koltermann (2000) estimated volume and heat transports across 48°N. Over the period 1996 to 1998, they found that the MOC exhibited high short term variability reflecting the *extreme* interannual behavior of the NAO-index. They suggested that there was a positive correlation between the NAO-index and both the volume and heat transport at a one year lag. In our study the converse appears to be true. The interannual variability in the volume and heat (not shown here) transport is negatively correlated to the NAO-index and is predominantly influenced by the immediate response to changes in the wind driven Ekman transport as illustrated by the first mode of the MCA. This idea is in agreement with a previous study by Eden and Willebrand (2001).

6.5 Vertical Advection

[26] In the previous sections the MOC has been presented in 2 dimensions. To gain an insight into the full 3 dimensional overturning circulation we will examine the vertical advection at the base of the thermocline. To achieve this we must first convert the model coordinates into density space. The vertical velocity at the thermocline is determined by linearly interpolating w, one of the prognostic variables saved from the model run to the depth the thermocline as described by $\sigma_1 = 32.3$ kgm^{-3} (Mauritzen and Häkkinen, 1999, where σ_1 is the potential density at 1000 m). Firstly the upper and lower *z-levels* that

contain the $\sigma_1 = 32.3$ kgm^{-3} surface are identified:

$$z_{upper} = z_{max}(\sigma_1 < 32.3) \qquad\qquad z_{lower} = z_{min}(\sigma_1 > 32.3). \tag{6.6}$$

then the vertical velocity at the thermocline is calculated by interpolating across these two points:

$$w(x,y,\sigma_1 = 32.3) = \frac{w(x,y,z_{upper}) - w(x,y,z_{lower})}{\sigma_1(z_{upper}) - \sigma_1(z_{lower})}(32.3 - \sigma_1(z_{lower})) + w(x,y,z_{lower}) \tag{6.7}$$

To further calculate the advection located at the base of the thermocline we simply use:

$$W_{therm}(x,y) = w(x,y,\sigma_1 = 32.3)A(y) \tag{6.8}$$

making the assumption that A, the surface area of the thermocline, can be approximated by the surface area of a grid box. Figure 6.10 displays the mean vertical velocities. In general we observed regions of downwelling adjacent to the continental boundaries in the Irminger and Labrador Basins (e.g. Spall and Pickart, 2001). In the remainder of the Subpolar Gyre there is a relatively weak upwelling, reflecting somewhat the large scale pattern of the curl in the wind stress associated with this region. There is also a notable region of cross thermocline diapycnal transport into the upper ocean to the west of the

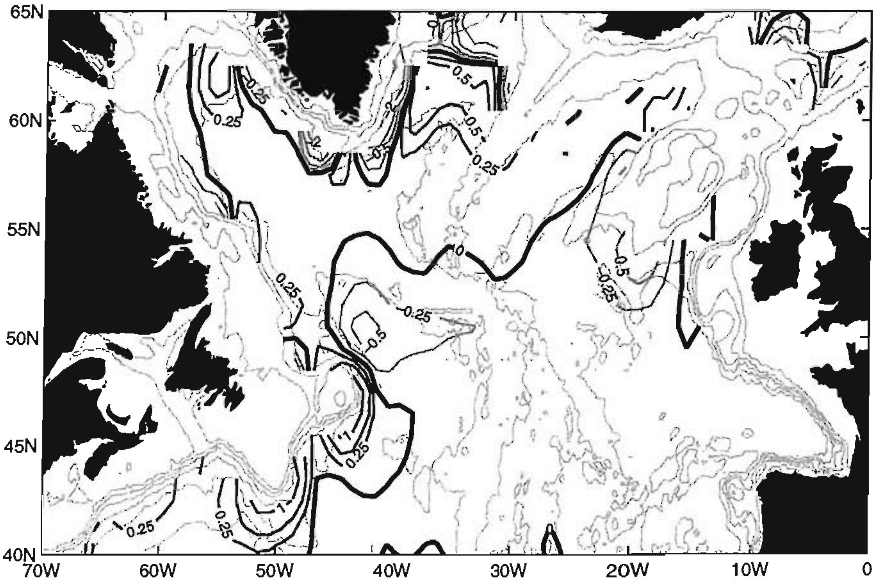

Figure 6.10: Advection at the base of the thermocline (as described by $\sigma_1 = 32.3kgm^{-3}$). *Black contours (positive values) indicate upward advection and grey contours (negative values) downwards advection. The zero line is given by the thicker black line. Values are of the order* $10^{-5}ms^{-1}$.

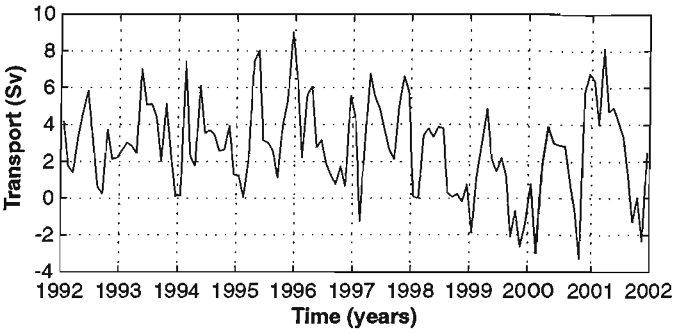

Figure 6.11: Time series of the net transport across the thermocline as described by $\sigma_1 = 32.3$ kgm^{-3} (Mauritzen and Häkkinen, 1999, where σ_1 is the potential density at 1000 m) in the intergyre zone (70°W to 0°W, 40°N to 50°N.

Grand Banks of Newfoundland and the Flemish Cap. Just to the north of this region of upwelling there is a region of enhanced localised downwelling. This downwelling maybe as a result of the collision/subduction of waters from the Labrador Sea meeting waters from the NAC and those to the south of the Subpolar Front. An enhanced downwelling also occurs to the southwest of the Rockall Plateau.

[27] As we have seen from Figure 6.10 a significant proportion of the vertical advection occurring in the intergyre zone is located off the Grand Banks of Newfoundland. The time mean upwelling at the base of the thermocline in this region (55°W to 40°W, 40°N to 50°N) is approximately 4.2 Sv, with a net transport of 2.8 Sv. The total upward transport in this region accounts for approximately 60% of the total upwelled over the whole intergyre zone (70°W to 0°W). The time evolution of the transport across the thermocline is illustrated in Figure 6.11.

[28] One of the principal mechanisms for this diapycnal transport may be the curl in the wind stress. Ekman pumping in this region could actively upwell waters into the upper ocean. This idea is supported by the fact that the seasonal harmonic of the cross thermocline transport is of $O(1Sv)$, peaking in late spring. To examine the influence of the divergence in the wind stress on the observed vertical transport W we can calculate w_E the Ekman pumping velocity which can be approximated by the following:

[29] By assuming constant ρ the continuity equation simplifies to:

$$\frac{\partial u}{\partial x} + \frac{\partial v}{\partial y} - \frac{\partial w}{\partial z} = 0 \qquad (6.9)$$

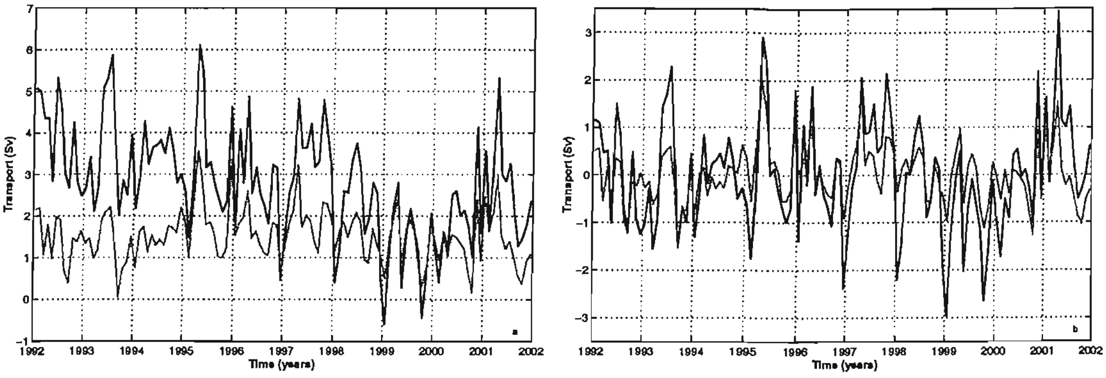

Figure 6.12: Vertical advection across the thermocline (black line) and equivalent transport due to Ekman pumping (grey line) off the Grand Banks of Newfoundland (55°W to 40°W, 40°N to 50°N). *a) for the original time series and b) for the demeaned and detrended time series.*

Integrating Equation 6.9 with respect to z across the Ekman boundary layer, assuming $w \rightarrow 0$ from the bottom of the Ekman boundary to the surface we arrive at an expression for w_E in terms of the zonal and meridional transport in the Ekman layer.

$$w_E = \frac{\partial U_E}{\partial x} + \frac{\partial V_E}{\partial y} \tag{6.10}$$

Combining this with linearised horizontal momentum equations vertically integrated over the Ekman layer:

$$\rho(\frac{\partial U_E}{\partial t} - fV_E) = \tau_x \qquad \rho(\frac{\partial V_E}{\partial t} + fU_E) = \tau_y \tag{6.11}$$

gives an expression for Ekman pumping velocity:

$$w_E = (f\rho)^{-1}(\frac{\partial \tau_y}{\partial x} - \frac{\partial \tau_x}{\partial y}) = \frac{\nabla \times \tau}{f\rho} \tag{6.12}$$

[30] Figures 6.12a and 6.12b show the relationship between the transport across the thermocline and the Ekman pumping velocity. There is a clear difference in magnitude during the early 1990s between the two time series (Figure 6.12a). After removing the mean and the trend from both time series we find that much of the short temporal variability is explained by changes in the wind forcing (Figure 6.12b). The upwelling is not significantly correlated to W_E at the 99^{th} percentile, however, there is a significant correlation after the upwelling signal has been high-pass filtered removing low frequency variations. It appears therefore that on greater than annual timescales there are other mechanisms controlling the diapycnal transport in this region. These longer term changes appear to

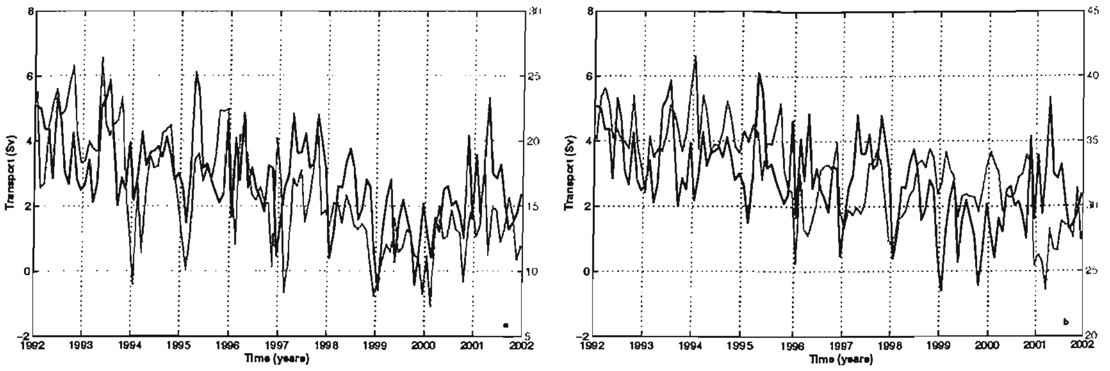

Figure 6.13: Veritcle advection across the thermocline (black line) and transport in the *a)* Deep Western Boundary Current and *b)* North Atlantic Current (grey line) at 45°N.

be dynamically linked to the strength in the boundary currents. Over the period of the model run both the northward flowing NAC and the southward flowing Labrador and Deep Western Boundary Currents have decreased in strength, as discussed in Chapter 5. This may explain the magnitude of the diapycnal transfer. Willebrand *et al.* (2001) suggest that, in level-coordinate OGCMs, spurious diapycnal mixing occurs in the region of the western boundary current. If this were the case in ECCO then the magnitude of the western boundary currents may well modulate this amount of spurious mixing.

6.6 Discussion of results

[31] The seasonal-to-interannual variability of the overturning in the Subpolar North Atlantic Ocean appears to be described primarily in terms of a linear response to the wind forcing. There is little or no contribution from variations in either the thermohaline structure or the external mode on sub-annual time scales. A strengthening of the overturning in this region over the winters of 1995/6 and 2000/1 coincides with a negative phase in the NAO and thus reduced zonal wind stress and southward Ekman transport.

[32] The interannual changes in the strength of the overturning associated with fluctuations in the NAO-index are also reflected on the seasonal time scale. The general weakening (strengthening) of the overturning during the winter (summer) months is largely due to the increase (decrease) in southward Ekman transport. These variations in the Ekman transport are directly associated with the (de) intensification of the dipole structure in

the first spatial mode of the wind stress curl (Figure 6.9, $C_{map1}(\nabla \times \tau)$).

[33] Significant cross thermocline advection in the Newfoundland Basin accounts for up to 3 Sv of upwelling. However, the upwelling observed in this region is not a prominent feature in the MCA although there are localised centres of action in the third and, to a lesser degree, the first spatial modes along the western extent of the Newfoundland Basin (Figure 6.9, $C_{map1,3}(\nabla \times \tau)$). The upwelling may be, in part, due to the collision of opposing boundary currents, although this requires further investigation. One disadvantage of the MCA performed in Section 6.4 is that the comparison of the zonally integrated MOC prevents any strong connection with local variability in the wind field.

[34] If localised upwelling does occur in the real world there may well be a signature found in the sea surface elevation. Häkkinen (2001) argues that these type of variations in the overturning circulation, if they exist, may be monitored through the use of satellite altimeter measurements. It remains to be seen whether or not variations in sea surface elevation, due to Ekman convergence or divergence, can be adequately separated from the steric changes induced through seasonal heat fluxes. The magnitude of the upwelling observed in this region may also be attributed to unrealistic biharmonic horizontal diffusion in regions of strong isopycnal slopes in the model (Willebrand *et al.*, 2001).

[35] The seasonal variations observed in the MOC are likely to be a robust feature as any anomalous overturning will be primarily dictated by the external forcing and will be independent of model setup (Böning *et al.*, 2001). The forcing frequency employed will, however, influence the amplitude of the anomalous overturning. In a model intercomparison Beismann *et al.* (2002) present the differences between the annual mean overturning for 1994 and 1993. The models were forced with daily to monthly wind fields and produced maximum overturning anomalies of 1 Sv. The external forcings employed in ECCO are 6 hourly; the magnitude of the anomalous overturning for the same period is approximately 2.5 Sv in the Subpolar region.

[36] Beismann *et al.* (2002) suggest that the difference in the spatial pattern of the overturning is characteristic of that attributed to Ekman fluctuations. The overturning anomaly in the Subpolar region is similar in nature to that of the first mode in our MCA between the MOC and wind stress curl ($C_{map1}(\Phi_{moc})$, Figure 6.9) . It is worth noting, however, that the Subtropical anomaly does not have this Ekman-like characteristic

as the centre of action is at a depth of 2500 m. This is more likely to be a function of the external mode i.e. variability in the barotropic transport of the Gulf Stream close to the western boundary. This spatial pattern is also very similar to that of the 1^{st} EOF of the overturning streamfunction presented by Gulev *et al.* (2003). They suggest this mode characterizes an immediate response to differences in the position of major currents.

[37] Marshall *et al.* (2001) suggest an anomalous overturning between 20°N and 60°N as a result of changes in the phase of the NAO, primarily acting through surface heat fluxes in the Labrador Sea region. This is also illustrated by Gulev *et al.* (2003) in their second spatial EOF of the overturning circulation. This mode reveals a deep baroclinic-like cell centred on the intergyre zone that appears characteristically similar to the winter-summer difference presented by Böning *et al.* (2001) . In a model intercomparison Willebrand *et al.* (2001) suggest that the convection in the Labrador Sea is of secondary importance to the overall strength of the MOC. Beismann *et al.* (2002) too, do not suggest any strong interannual variability in the buoyancy forcing in this region.

[38] Our time series is too short to examine the longer term trends but we make a note here for completeness. Gulev *et al.* (2003) propose that the baroclinic response, lagged by around 3 years, is related to the adjustment of the circulation to buoyancy forcing, namely the production of Labrador Sea Water. A 3 year lagged baroclinic response is also suggested by Eden and Willebrand (2001), but to the wind forcing and subsequent adjustment of the Subpolar Gyre. Gulev *et al.* (2003) cite this difference to be a function of the model setup.

[39] Dong and Sutton (2001) found a clear distinction between the high frequency variability forced by Ekman processes and the low frequency characteristics of the density driven overturning. Using a coupled model they confirmed results from Eden and Willebrand (2001) of an NAO related lagged response in the overturning. The simultaneous spin up (spin down) of the Subtropical and Subpolar Gyres enhances (weakens) the overturning on a time scale of 10 years (whereas Eden and Willebrand (2001) found the adjustment to be of the order of 3 years), but they found no evidence to support NAO related buoyancy forcing of the overturning.

[40] After the winter of 1995/6 we find that there is a decrease in the total overturning in ECCO. One plausible mechanism for this, suggested by Tsujino and Suginohara (1999), is

through heat transfer from the surface layers to depth through a raised thermocline from Ekman suction. During the winter of 1995/6 there was weaker cyclonic wind stress curl over the northern Subpolar Gyre leading to a reduced Ekman suction in the region, which in theory would prevent a buoyancy gain by the sub thermocline waters. This coupled with a reduced heat flux during the winter months will add stability to the water column thus inhibiting the convective activity in subsequent years.

[41] From a series of model studies Spall and Pickart (2001) found that the majority of the downwelling occurs where convective mixing is found near steep topography and hence is sensitive to the boundary currents. In coarse resolution models, such as ECCO, the boundary currents are not fully resolved and therefore not realistic. Higher resolution runs would be required to determine the sensitivity of the overturning to the definition of boundary currents.

6.7 Summary

[42] We have described the evolution of the overturning circulation by analysing an ocean state estimation of the period 1992-2002. In addition we have shown the strong statistical coupling of the overturning circulation with the curl in the wind stress and have argued the physical interpretation of each mode.

[43] Ocean General Circulation Models have been previously used to examine the instantaneous and delayed response of horizontal and meridional circulation to variable external forcing. In this study we have been primarily interested in the instantaneous response of the ocean to variable wind forcing. The temporal length of the model run is insufficient to investigate any lagged response to the atmospheric forcing. However, trends seen in the MCA and in the time evolution of the overturning can be interpreted essentially as variations in the density driven component of the overturning.

[44] The seasonal variability observed in the overturning strength is almost solely attributed to fluctuations in the Ekman transport in the central Subpolar Gyre. This mechanism remains a significant contributor to MOC variability on interannual time scales. The approach of using an MCA between the wind stress curl and MOC not only allows one to gain an idea of the degree of coupling, it also allows one to view the associated

spatial patterns of each field. This is illustrated in the first two modes of the MCA; NAO and EAO-like patterns are found to be associated with an Ekman overturning cell and anomalous Ekman pumping respectively.

[45] In addition to the downwelling in the Labrador and Irminger Seas cited in many previous studies, we find that there is a region of relatively strong diapycnal transfer along the Grand Banks of Newfoundland. This seasonally varying vertical transport accounts for a significant proportion of the upwelling at this latitude and has been shown to have possible links with the Ekman pumping and boundary currents in this region.

[46] There is still uncertainty over the ability of OGCMs to represent the true extent of the Meridional Overturning Circulation, with significant differences in the mean state and low-frequency fluctuations remaining a function of model numerics and parametrisations (Willebrand *et al.*, 2001). However, our results show that there are significant variations in the strength of the MOC as a result of high-frequency seasonal fluctuations in the Ekman transport in the Subpolar North Atlantic Ocean and must therefore be considered when interpreting meridional transport estimates from shipboard measurements.

Chapter 7

Summary and Conclusions

[1] Through the use of data from the Topex/Poseidon satellite altimeter and the ECCO *constrained* ocean General Circulation Model (GCM) we have examined the variability of the large-scale circulation of the Subpolar North Atlantic Ocean. In particular we have focussed on the position of the Subpolar Front as an indicator of changes on the basin scale. Principal mechanisms that influence the evolution of the circulation on seasonal-to-interannual time scales have also been documented.

[2] As an inherent part of this study the realism of two GCMs was established through a series of validations. Initially the only GCM available for this study was OCCAM, which subsequently formed an interesting comparative model to ECCO. Even though this model had a greater resolution than that of ECCO, it clearly was not reproducing the observed ocean as well and appeared to have not quite reached equilibrium. It had also only been run for a relatively short period of time. The *constrained* GCM, on the other hand, provided a more realistic ocean state estimation to work from and thus became the chosen tool for this study.

[3] Using a combination of observations and model data we identify changes in the circulation in response to atmospheric forcing and forcing internally within the ocean. Although the broad context on which this thesis was based remained relatively unchanged during the course of the study, certain sections of the thesis were developed on a more impromptu basis, e.g. *eastward propagating features along the Subpolar Front.* The time scales that we were concerned with, were primarily dictated by length of observational data and du-

ration of the model run available. However, it is still important to examine these time scales and document previous changes during this period. As previous studies have revealed, there have been significant *interannual* variations of certain characteristics of the Subpolar North Atlantic Ocean over the last decade, e.g. Bersch *et al.* (1999), Reverdin *et al.* (1999) *etc.*

[4] Analysis of the altimeter data provided a summary of the surface variability of the Subpolar North Atlantic Ocean over the last decade. It was found that eddy variability was primarily driven by seasonally vary winds in the Subpolar Gyre region and by the relatively seasonally invariant flow of the NAC to the south (Figure 3.11; *previously documented by Heywood* et al., *1994*). Overall it is shown that the eddy variability observed in the Subpolar region is closely linked to that of the winter-time NAO-index, with the Iceland Basin exhibiting the highest correlation.

[5] In addition to providing a quantitative measure of the surface variability in the Subpolar North Atlantic Ocean, we are also able to infer changes in the major circulation pathways from non wind-driven eddy activity, generally of values greater than $\sim$ 0.02 m^2s^{-2}. Over the period 1992 to 2001, data from the altimeter appear to suggest that there was a decrease in the strength of the NAC by $\sim$ 16%. It is suggested that this may be reflected in the changing nature of the NAO, e.g. Curry and McCartney (2001), although we find no correlation with either the NAO or the local wind field. The tendency for the strength of the NAC and more generally the Subpolar Gyre to vary on longer than annual time scales is reflected in ECCO and also in a recent study by Häkkinen and Rhines (2004). We find that the weakening of the NAC ($\sim$ 20%) and more generally the Subpolar Gyre in ECCO is as a result of the changes in the baroclinic structure in the Labrador Basin; Slumping of the isopycnals in the Labrador Basin leads to a spin down of the circulation in the region.

[6] Non wind-driven eddy activity is also observed in the Labrador Sea, in the region where the West Greenland Current separates from the coastal shelf of Greenland. Lagged correlations between eddy kinetic energy values in this region and those in the Irminger Basin suggest a dynamical link via the boundary currents. Although Prater (2002) suggests a possible similarity between the level of eddy activity associated with the separation region and the winter-time NAO-index, we find no correlation between the two with our

extended time series.

[7] Interannual variations in the position of the NAC and hence Subpolar Front (SPF) can also be inferred from the altimeter data. We confirm the significant shift in the SPF westward in the Iceland Basin in the mid 1990s observed by Bersch *et al.* (1999), which coincided with a switch in the phase of the NAO. We find that the front remained in a more westward position through to 1999, before returning to the position prior to the change in phase of the NAO. In ECCO we also find a westward shift of the SPF in the Iceland basin. However, the front does not remain in a westerly position for as long as observed in the satellite data, returning eastward when the NAO reverted back to a positive phase in 1999. Shifts along other parts of the SPF are less clear. Significant variations in the position of the frontal system in the Newfoundland Basin are not apparent in the altimeter observations, but in ECCO there are small deviations in the position of the thermal front in the opposite direction to those observed in the Iceland Basin. On the other hand, when examining the evolution of the NAC we find relatively larger shifts in the Newfoundland Basin. The *core* of the current shifts southeastward over the period of the model run, but also becomes broader and more diffuse, a process with a time-scale similar to that of the changes in the Labrador Sea previously mentioned.

[8] The principal mechanism for the observed changes in the position of the SPF is a Sverdrup-like response of the ocean to the wind forcing. This mechanism has a centre of action over the intergyre zone between the Subpolar and Subtropical Gyres, which produces an anomalous heat transport in opposite directions either side of the MAR. The anomalous heat transport to the west of the MAR is also thought to be responsible for generating upper ocean temperature anomalies that propagate eastward along pathway of the NAC.

[9] With dominant modes of variability such as those outlined above we have also been able to identify different circulation regimes and export pathways from the Subpolar Gyre in ECCO (*cf.* Figures 5.13a and 5.13b). Through the use of lagrangian diagnostics, we have shown that there is a significant difference in the fraction of intermediate and deep waters being exported from the Labrador Sea via the Deep Western Boundary Current under these regimes. There is also evidence of a possible export pathway southward to the east of the MAR, which appears to exhibit some dependence on the atmospheric forcing

and phase of the NAO.

[10] We find that variations in the Meridional Overturning Circulation (MOC) are anti-correlated to those of the horizontal circulation on seasonal-to-interannual time-scales. Although both are coupled to the atmosphere through similar spatial patterns in the wind field, the nature of the response differs. The high frequency fluctuations in overturning strength are dominated by changes in the Ekman transport, whereas the changes in the horizontal circulation are Sverdrup-like in nature, as previously mentioned. The variability in the overturning, hence Ekman transport, is strongly linked to the strength of the zonal winds, most notably along 55°N and exhibits a significant correlation to the NAO. For example, in both the winters of 1995/6 and 2000/1, NAO^- years, we find that there has been a strengthening of the overturning circulation. Two principal modes of variability are identified in the MOCs response to fluctuations in the wind forcing: An NAO and an East Atlantic Oscillation-like pattern are found to be associated with an Ekman overturning cell and anomalous Ekman pumping respectively. There is also evidence of longer-term variations in the strength of the overturning, but the length of the model run is insufficient to quantify these characteristics. The slow down of the horizontal circulation, in response to a possible reduction in winter time convection in the Labrador Sea, does not appear to be reflected in the overturning signal. This would suggest that changes in convective activity and the baroclinic structure in the Subpolar Gyre do not significantly affect the MOC on the time-scales considered.

[11] Over the study period there have been two reversals in phase of the NAO from a positive to a negative phase (1995 to 1996 and 2000 to 2001). We find that these two reversals are characteristically different. The shift of the Subpolar Front in the Iceland Basin that accompanied the phase reversal in 1995/6 was much larger than in 2000/1. This was in part reflected in the larger northward heat transport anomaly east of the MAR in 1996. The westward shift in the Subpolar Front in 1996 may have also been enhanced by the propagation of a temperature anomaly into the Iceland Basin coinciding with a switch in the phase of the NAO. In addition we find that the pathway of the NAC followed a more southerly trajectory across the MAR in 2001, consistent with a more southerly position in the zero of the wind stress curl during this period.

Further Work

[12] With the continuing improvement of altimeter products, there may be justification in repeating the study of surface variability in the Subpolar North Atlantic. There are products in existence that combine Topex/Poseidon and European Research Satellite measurements to a spatial resolution of 1/3° and temporal sampling of 7 days. In addition, the introduction of the Jason and ENVISAT altimeter missions will add to the global coverage and quality of data in the the coming years. With only two significant reversals in the phase of the NAO during the winters of 1995/6 and to a lesser extent 2000/1, it would be interesting to examine changes in the location of the Subpolar Front in an extended study through a series of phase reversals. Another possible extension of this study would be to assess the performance of a series of high resolution modelling studies to see whether or not they are capturing the true variability observed by the altimeter measurements.

[13] One of the more intriguing features of this work has been the identification of eastward propagating features along the boundary between the Subpolar and Subtropical Gyre. It would be interesting to examine these anomalies with respect to:

- further quantifying the nature of these anomalies,
- interactions with the flow field,
- quantifying any delayed feedback to the atmosphere.

To achieve this a model run of considerably longer length than that of ECCO would be required. It would also be beneficial to use a model that has been run both in ocean only and in a coupled format, allowing the identification of any ocean-atmosphere interaction/feedback associated with these anomalies. Employing the technique of Complex Empirical Orthogonal Analysis to an extended time series would allow one to better quantify these features.

It may also be possible to extend our brief study into different export pathways from the Subpolar North Atlantic Ocean in response to fluctuations in Subpolar Gyre circulation. Sustained periods of forcing under different atmospheric modes may result in significant changes in the distribution of water masses in the intermediate and deep ocean in both the Subpolar and Subtropical North Atlantic Ocean. This type of analysis may also be used to study the influence of the topography on the circulation e.g. flow through the Charlie Gibbs Fracture Zone.

APPENDICES

Appendix A

On the use of splines

[1] We require a function, $f(x)$, to be fitted to data while filtering out noise on scales greater than a frequency h_{cut}. For example if we take a series of satellite data, a, we can produce an approximation of $f(x)$ using a terminated Taylor series.

$$\sum_{i=0}^{n}(x - x_0)^i D^i f(x_0)/i! \tag{A.1}$$

However, in this case of a data set spanning 10 years and the spatial domain of the Subpolar North Atlantic Ocean n becomes unacceptably large. The use of a spline can overcome this problem by a means of simplification. The data are subdivided into intervals that can be approximated sufficiently by a polynomial, p, of relatively low order.

$$s(x) = p_j(x) \qquad\qquad \text{for } x \in [\xi_j \ldots \xi_{j+1}] \tag{A.2}$$

The MATLAB Spline Toolbox proves a sufficeint tool for implimenting such a function. Using the *spap2* function, that implements the *B-spline*, a series of specified *knots* and *weightings* can be passed allowing greater control over the data that are being manipulated.

[2] The conditions chosen for the curve fitting in this instance are that the end points in a sequence have a 100 % weighting attached to them. This allows the curve to converge onto the actual sea surface height without tailing off to an extreme gradient at either end of the data series. With hindsight this still may give too much of an increased gradient as the 100 % weighting asigned to the two endpoints may result in an artifically high gradient going to an unweighted point to on weighted 100 %. It may have proven more

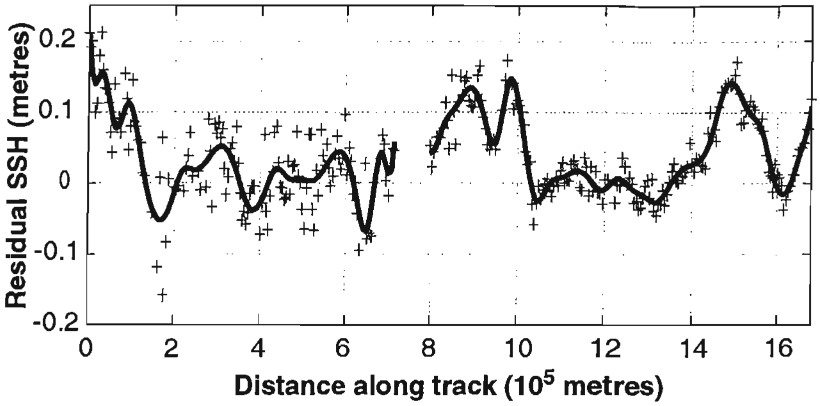

Figure A.1: Residual sea surface height of cycle 300, pass 146 (*crosses*), with a 30 *km* knotted spline fitted (*solid line*).

ralistic to apply a tapered weighting function towards the end of a data series, therefore reducing any artifically high gradients. The result of this type of curve fitting to data along a satellite pass, is illustrated in Figures A.1 and A.2.

[3] One of the important applications of the spline is its numerical differentiation and integration. To derive residual current measurements or values of eddy kinetic energy from the residual sea surface height we require the slope of the surface. As the data are now represented by a series of polynomial functions their derivatives can be simply calculated.

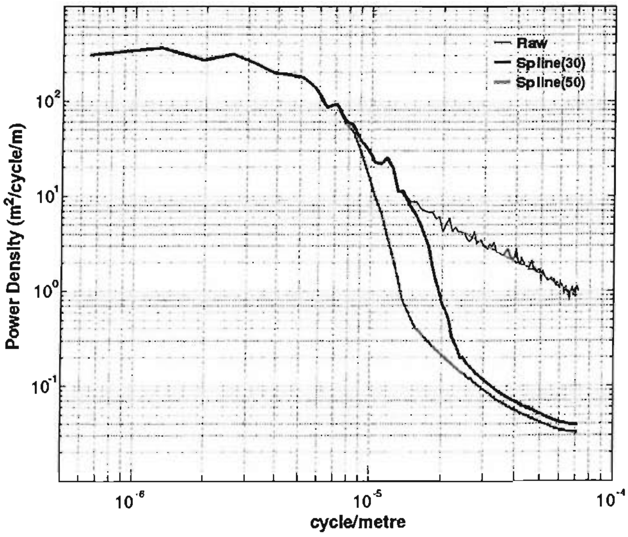

Figure A.2: Power spectral density plot of the raw and splined sea surface height data from cycle 300, pass 146.

Appendix B

Empirical Orthogonal Functions (EOFs)

B.1 EOF Analysis

[1] The following provides a summary of the more comprehensive descriptions of EOF analysis given by Björnsson and Venegas (1997), Emery and Thompson (2001), Wikle (2003). To perform an EOF analysis on a data matrix D we will use the method of Singular Value Decomposition (SVD). D can be expressed in the form:

$$D_{mn} = U_{mm} S_{mn} V_{nn}^T \tag{B.1}$$

where U and V are the left and right singular vectors comprising of m column vectors of length m and n column vectors of length n respectively. S, the singular matrix, has the form:

$$\mathrm{S} = \begin{bmatrix} \delta_1 & 0 & \dots & 0 & 0 & \dots & 0 \\ 0 & \delta_2 & \dots & 0 & 0 & \dots & 0 \\ \vdots & \vdots & \ddots & \vdots & \vdots & \ddots & \vdots \\ 0 & 0 & \dots & \delta_m & 0 & \dots & 0 \end{bmatrix} \quad \text{for m<n} \tag{B.2}$$

or

$$\mathrm{S} = \begin{bmatrix} \delta_1 & 0 & \ldots & 0 \\ 0 & \delta_2 & \ldots & 0 \\ \vdots & \vdots & \ddots & \vdots \\ 0 & 0 & \ldots & \delta_n \\ 0 & 0 & \ldots & 0 \\ 0 & \vdots & \ddots & \vdots \\ 0 & 0 & \ldots & 0 \end{bmatrix} \quad \text{for m>n} \tag{B.3}$$

where δ_n are the *singular values* [1] and are arranged such that $\delta_1 > \delta_2 > \ldots > \delta_n > 0$.

[2] As our data are typically represented in three dimensions, before the SVD method is applied the data must be transformed into a two dimensional matrix. This can be achieved using, for example, the Matlab function *reshape*. We have now collapsed the original matrix down from a $ndx \times ndy \times ndt$ matrix to the data matrix D now in the form $(ndx * ndy) \times ndt$.

[3] After removing the time mean from each spatial point, any missing values and performing any filtering or signal removal required the SVD method can be applied. The spatial modes of the EOF analysis are given by U, namely the *EOFs* or the *eigenvectors* assuming D is of dimension $ndz \times ndt$. U has dimension $ndz \times i$, where i is the number of modes, which in this form is of limited use in interpretation any spatial patterns in the data. The matrix U therefore has to be reconstructed with the dimensions of original data matrix i.e. $ndx \times ndy \times ndt$. This is achieved by first inserting the missing values removed from the original data prior to employing the SVD method. Then once this is done the resultant matrix, now with the correct number of elements present, can be reshaped with the correct dimension.

[4] V in the above example represents the *amplitude time series* or *Principal Components* (*PC*). This matrix, of the form $ndt \times i$, provides a understanding of the time evolution of the spatial patterns observed in U. The *PC*s can also be represented by V scaled by the singular matrix, S, such that

$$PC = VS. \tag{B.4}$$

---

[1] $\delta_{i,i} = \sqrt{\lambda_i}$, where λ_i are the *eigenvalues* of D

[5] The EOFs and *PC*s can be individually reconstructed into a new data series. In this sense they can also be used to compress a datasets by selecting only the first i modes as these explain the majority of the variance. Another reason for reconstructing the first n modes is that these modes are regarded to contain the dynamic signal and the lesser modes random noise. So the reconstruction for the first mode is simply:

$$R_i(x,t) = U_i(x)\delta_{i,i}V_i^T(t) \qquad\qquad i = 1. \tag{B.5}$$

The percentage of the variance explained by each mode is given by

$$\frac{\delta_{i,i}^2}{\sum_{j=1}^{N}\delta_{j,j}^2} \times 100 \tag{B.6}$$

Essentially the method of SVD is a computationally efficient, but equivalent method of calculating the EOFs, *PC*s and *eigenvalues* (Λ) using the covariance matrix of D.

$$C = DD^T, \qquad CU = U\Lambda \quad \text{and} \quad PC = D^TU \tag{B.7}$$

[6] When calculating a truncated SVD or *SVDs* equation B.6 becomes incorrect as we are normalising by only a fraction of the total variance. To overcome this we can redefine the percentage of the variance explained by the reduced number of modes by:

$$\frac{\sum var(USV^T)}{\sum var(D)}\frac{\delta_{i,i}^2}{\sum_{j=1}^{N}\delta_{j,j}^2} \times 100, \tag{B.8}$$

which uses the ratio of the variances between the SVDs and the original data as a scaling factor for the eigenvalues.

B.1.1 A Note of Caution

[7] The EOF analysis aims to decompose D into the modes of variability in a dataset. These modes are statistical modes and are not necessarily representant of actual physical modes. Björnsson and Venegas (1997) emphasizes the need to re-examine the original data to confirm any signals found in the advanced analysis techniques.

[8] The method outlined above is for *real* data fields and therefore represent standing oscillatory patterns only. It may be possible to gain an insight into propagating features using the above analysis when it is found that there are two similar modes with like EOFs

and percentage of explained variance, but with a phase difference in the *PC*. To further investigate propagating features one can use the method of *Complex EOF analysis.*

B.2 Complex EOF Analysis

[9] In short Complex EOF (CEOF) analysis using the SVDs method is computationally identical to that of the EOF analysis using SVDs, but differs slightly in the *pre* and *post* processing. Each point in D is combined with its *Hilbert* transform, prior to the SVDs analysis.

[10] It is difficult to interpret the results from the CEOF analysis purely as a combination of *real* and *imaginary* contributions. It is therefore somewhat more enlightening to examine the decomposition in terms of amplitude and phase. The spatial amplitudes are given by:

$$EOF_\alpha(x,y,i) = [EOF(x,y,i)EOF^*(x,y,i)]^{1/2} \tag{B.9}$$

and similarly for the amplitudes of the *Principal Components*:

$$PC_\alpha(t,i) = [PC(t,i)PC^*(t,i)]^{1/2}. \tag{B.10}$$

The phase of the spatial signal is derived by:

$$EOF_\omega(x,y,i) = \arcsin\left[\frac{Im(EOF(x,y,i))}{EOF_\alpha(x,y,i)}\right] \tag{B.11}$$

and again similarly for the phase of the temporal signal:

$$PC_\omega(t,i) = \arcsin\left[\frac{Im(PC(t,i))}{PC_\alpha(t,i)}\right]. \tag{B.12}$$

[11] As an illustration; a gaussian-like anomaly is propagated across an x-y domain from the bottom left (0,0) to the top right (20,20) corner a total of five times. The resulting principal mode of a CEOF analysis is shown in Figure B.1. In our analysis a cyclonic rotation of the phase arrows indicates a propagation in time. The magnitude of the signal, given by the length of the arrows, is emphasised by the coloured contours underlaid. The propagation speed of the anomaly can be calculated by using the phase-time diagram. One complete rotation takes approximately 20 time-units. As we find from our spatial map, the phase arrows complete one rotation between the lower left and upper right corners, thus

the anomaly takes approximately 20 time-units to cross the domain. One can also identify the time at which a propagating anomaly crosses a particular location. For example, at 15,15 on our spatial map the phase is approximately π, a phase of zero being due east, using the phase-time diagram one can see that the first time the anomaly passes this point is at time 15. For another example of CEOF analysis and its interpretation see Tourre and Kushnir (1999).

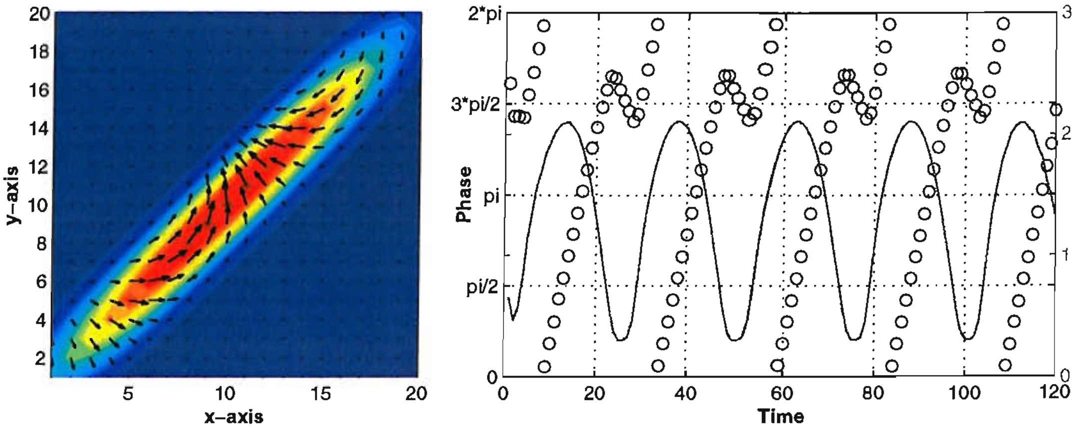

Figure B.1: The first mode of a CEOF analysis of a northeastward propagating anomaly; a synthetic example. ***Left,*** *a spatial representation and* ***right*** *a temporal representation of the phase and magnitude associated with the first mode.*

B.3 Maximum Covariance Analysis

[12] A further derivation of SVD analysis is to analyse two different datasets of same temporal length. The purpose of the analysis is to identify closely coupled modes of variability between the two fields. X and Y of lengths $ndx \times ndt$ and $ndy \times ndt$ are combined forming a covariance matrix C. As the two datasets under investigation are likely to have different amplitudes, each time series of X and Y can be normalised by their respective standard deviations to prevent one signal dominating over the other. In this case C becomes the cross-correlation matrix.

$$C = XY^T \tag{B.13}$$

[13] An SVD analysis is then performed on C as in Section B (where C is now D). The resulting matrices U and V are the respective spatial EOFs of X and Y. The corresponding

PCs are given by:

$$PC_X = XU \qquad \text{and} \qquad PC_Y = YU \tag{B.14}$$

The singular value matrix S is treated in the same way as before, giving a measure of the importance of each coupled mode.

Bibliography

Arakawa, A., & Lamb, V. R. 1977. Methods of Computational Physics. vol. 17. Academic Press.

Bacon, S. 1997. Circulation and fluxes in the North Atlantic between Greenland and Ireland. *J. Phys. Oceanogr.*, **27**(7), 1420–35.

Bacon, S. 1998. Decadal variability in the outflow from the Nordic seas to the deep Atlantic Ocean. *Nature*, **394**(6696), 871–4.

Barnston, A. G., & Livezey, R. E. 1987. Classification, Seasonality and Persistence of Low-Frequency Atmospheric Circulation Patterns. *Monthly Weather Review*, **115**(6), 1083–1126.

Beckmann, A., Böning, C. W., Brugge, B., & Stammer, D. 1994. On the generation and role of eddy variability in the central North Atlantic Ocean. *J. Geophys. Res.*, **99**(C10), 20381–91.

Beismann, J-O., Böning, C., & Stammer, D. 2002. Interannual to decadal variability of teh Meridional Overturning Circulation of the Atlantic: A comparison of the response to Atmospheric Fluctuations in three Ocean Models. *Clivar Exchanges*, **7**(3/4), 34–46.

Belkin, I. M., & Levitus, S. 1996. Temporal variability of the subarctic front near the Charlie-Gibbs Fracture Zone. *J. Geophys. Res.-Oceans*, **101**(C12), 28317–28324.

Bellucci, A. 2004. Free and forced variability in the North Atlantic Ocean. *University of Southampton Faculty of Science, School of Ocean and Earth Sciences, PhD Thesis*, 112pp.

Bersch, M. 2002. NAO-induced changes of the upper-layer circulation in the northern North Atlantic Ocean. *J. Geophys. Res.*

Bersch, M., Meincke, J., & Sy, A. 1999. Interannual thermohaline changes in the northern North Atlantic 1991-1996. *Deep Sea Res., Part II*, **46**(1-2), 55–75.

Björnsson, H., & Venegas, S. A. 1997. A Manual for EOF and SVD analyses of climate data. *http://www.dcess.ku.dk/ silvia/*, 52.

Blanke, B., & Raynaud, S. 1997. Kinematics of the Pacific Equatorial Undercurrent: An Eulerian and Lagrangian approach from GCM results. *J. Phys. Oceanogr.*, **27**, 1038–1053.

Böning, C., Dieterich, C., Barnier, B., & Jia, Y. 2001. Seasonal cycle of meridional heat transport in the subtropical North Atlantic: a model intercomparison in relation to observations near 25°N. *Prog. Oceanogr.*, **48**, 231–253.

Bower, A. S., Le Cann, B., Rossby, T., ZENK, W., Gould, J., Speer, K., Richardson, P.L., Prater, M.D., & Zhang, H-M. 2002. Directly measured mid-depth circulation in the northeastern North Atlantic Ocean. *Nature*, **419**(6907), 603–607.

Bryan, K. 1969. A numerical method for the study of the circulation of the world ocean. *J. Comput. Phys.*, 4(3), 347–376.

Cayan, D. 1992. Latent and sensible heat flux anomalies over the northern oceans: The connection to monthly atmospheric circulation. *J. Clim.*, **5**, 354–369.

Cooper, C., & Gordon, C. 2002. North Atlantic Oceanic Decadal Variability in the Hadley Centre Coupled Model. *J. Clim.*, **15**, 45–72.

Cox, M. D. 1984. *A primitive equation 3-dimensional model of the ocean.* GFDL Ocean Group Technical Report, vol. 1. Princeton University, Princeton, N.J. 08542, U.S.A: Geophysical Fluid Dynamics Laboratory/NOAA.

Cuny, J., Rhines, P., Niiler, P., & Bacon, S. 2002. Labrador Sea boundary currents and the fate of the Iminger Sea Water. *J. Phys. Oceanogr.*, **32**(2), 627–647.

Curry, R. G., & McCartney, M. S. 1996. Labrador Sea Water carries northern climate signal south. *Oceanus*, **Fall/Winter**, 24–28.

Curry, R. G., & McCartney, M. S. 2001. Ocean gyre circulation changes associated with the North Atlantic Oscillation. *J. Phys. Oceanogr.*, **31**(12), 3374–400.

Czaja, A., & Frankignoul, C. 1999. Influence of the North Atlantic SST on the atmospheric circulation. *Geophys. Res. Letters*, **26**(19), 2969–72.

Dickson, B., Yashayaev, I. M., Meincke, J., Turrell, W. R., Dye, S., & Holfort, J. 2002. Rapid freshening of the deep North Atlantic Ocean over the past four decades. *Nature*, **416**, 832–837.

Dietrich, G. 1969. Atlas of the hydrography of the North Atlantic Ocean. *Page 140 of: International Council for the Exploration of the Seas, Hydrographic service, Copenhagen.*

Dietrich, G., Kalle, K., Krauss, W., & Sielder, G. 1975. *General Oceanography.*

Dong, B. W., & Sutton, R.T. 2001. The dominant mechanisms of variability in the Atlantic ocean heat transport in a coupled ocean-atmosphere GCM. *Geophys. Res. Letters*, **28**(12), 2445–2448.

Ducet, N., Le Traon, P. Y., & Reverdin, G. 2000. Global high-resolution mapping of ocean circulation from TOPEX/Poseidon and ERS-1 and -2. *J. Geophys. Res.*, **105**(C8), 19477–98.

Dutkiewicz, S., Rothstein, L., & Rossby, T. 2001. Pathways of cross-frontal exchange in the North Atlantic Current. *J. Geophys. Res.-Oceans*, **106**(C11), 26917–26928.

Eden, C., & Böning, C. 2002. Sources of eddy kinetic energy in the Labrador Sea. *J. Phys. Oceanogr.*, **32**(12), 3346–3363.

Eden, C., & Willebrand, J. 2001. Mechanism of interannual to decadal variability of the North Atlantic circulation. *J. Clim.*, **14**(10), 2266–80.

Emery, W. J., & Thompson, R. E. 2001. *Data Analysis Methods in Physical Oceanography.* Elsevier.

Esselborn, S., & Eden, C. 2001. Sea surface height changes in the North Atlantic Ocean related to the North Atlantic Oscillation. *Geophys. Res. Letters*, **28**(18), 3473–6.

Flatau, M. K., Talley, L., & Niiler, P. P. 2003. The North Atlantic Oscillation, surface current velocities, and SST changes in the subpolar North Atlantic. *J. Clim.*, **16**(14), 2355–2369.

Foldvik, A., Aagaard, K., & Torresen, T. 1988. On the velocity field of the East Greenland Current. *Deep Sea Research*, **35**(8), 1335–1354.

Frankignoul, C., de Coetlogon, G., Joyce, T. M., & Dong, S. F. 2001. Gulf stream variability and ocean-atmosphere interactions. *J. Phys. Oceanogr.*, **31**(12), 3516–3529.

Fratantoni, D. M. 2002. North Atlantic surface circulation during the 1990s observed with satellite-tracked drifters. *J. Geophys. Res.*, **106**(C10), 22067–93.

Gill, A. E. 1982. *Atmosphere-Ocean Dynamics.* International Geophysics, vol. 30. Academic Press.

Gill, A. E., & Niiler, P. 1973. The theory of the seasonal variability in the ocean. *Deep Sea Research*, **20**, 141–177.

Gulev, S. K., Barnier, B., Knochel, H., Molines, J-M., & Cottet, M. 2003. Water Mass Transformation in the North Atlantic and Its Impact on the Meridional Circulation: Insights from an Ocean Forced by NCEP-NCAR Reanalysis Surface Fluxes. *J. Clim.*, **16**(19), 3085–3110.

Häkkinen, S. 2001. Variability in sea surface height: A qualitative measure for the meridional overturing in the North Atlantic. *J. Geophys. Res.*, **106**(C7), 13,837–13,848.

Häkkinen, S., & Rhines, P. 2004. Decline of the Subpolar North Atlantic Circulation during the 1990s. *Science*, **304**, 555–559.

Hall, M. M., & Bryden, H.L. 1982. Direct estimates and mechanisms of ocean heat transport. *Deep Sea Research*, **35**, 1441–1450.

Hansen, B., & Larsen, K.M.H. 1999. The Atlantic Inflow to the Nordic Seas. *Internat. WOCE Newsletter*, **35**, 33–35.

Heywood, K. J., McDonagh, E. L., & White, M. A. 1994. Eddy kinetic energy of the North Atlantic subpolar gyre from satellite altimetry. *J. Geophys. Res.*, **99**(C11), 22525–39.

Hirschi, J., Baehr, J., Marotzke, J., Stark, J., Cunningham, S. A., & Beismann, J-O. 2003. A monitoring design for the Atlantic meridional overturning circulation. *Geophys. Res. Letters*, **30**(7).

Hogg, N. G. 1992. On the Transport of the Gulf-Stream between Cape-Hatteras and the Grand-Banks. *Deep-Sea Research Part a-Oceanographic Research Papers*, **39**(7-8A), 1231–1246.

Holliday, N. P., Pollard, R. T., Read, J. F., & Leach, H. 2000. Water mass properties and fluxes in the Rockall Trough, 1975-1998. *Deep Sea Res., Part I*, **47**(7), 1303–32.

Hurrell, J. W. 1995. Decadal trends in the North Atlantic Oscillation: regional temperatures and precipitation. *Science*, **269**(5224), 676–9.

Hurrell, J. W. 1996. Influence of variations in extratropical wintertime teleconnections on Northern Hemisphere temperature. *Geophys. Res. Letters*, **23**(6), 665–8.

Hurrell, J. W. 2003. *North Atlantic Oscillation (NAO) Indices Information.* http://www.cgd.ucar.edu/ jhurrell/nao.html.

Jones, P.D. 2003. *NAO index.* http://www.cru.uea.ac.uk/cru/data/nao.htm.

Jones, P.D., Jonnson, T., & Wheeler, D. 1997. Extension to the North Atlantic Oscillation using early instrumental pressure observations from Gibraltar and south-west Iceland. *Internat. J. Clim.*, **17**, 1433–1450.

JVT-Topex. 1992. Topex/Poseidon Joint Verification Plan. *JPL Publication*, **92-9**.

Kara, A.B., Rochford, P.A., & Hurlburt, H. E. 2000. An optimal definition for ocean mixed layer depth. *J. Geophys. Res.*, **105**(C7), 16,803–16,821.

Kearns, E. J., & Paldor, N. 2000. Why are the meanders of the North Atlantic Current stable and stationary? *Geophys. Res. Letters*, **27**(7), 1029–1032.

Kearns, E. J., & Rossby, H. T. 1998. Historical position of the North Atlantic Current. *J. Geophys. Res.*, **103**(C8), 15509–24.

Kelly, K. A., Singh, S., & Hang, R. X. 1999. Seasonal Variations of Sea Surface Height in the Gulf Stream Region. *J. Phys. Oceanogr.*, **29**(3), 313–327.

Köhl, A., Stammer, D., Cornuelle, B. D., Remy, E., Lu, Y., Heimbach, P., & Wunsch, C. 2003. The Global 1°WOCE Synthesis: 1992-2001. *ECCO Report Series*, **20**, 33.

Krahmann, G., Visbeck, M., & Reverdin, G. 2001. Formation and propagation of temperature anomalies along the North Atlantic Current. *J. Phys. Oceanogr.*, **31**(5), 1287–303.

Krauss, W. 1986. The North Atlantic Current. *J. Geophys. Res.*, **91**(C4), 5061–74.

Krauss, W. 1995. Currents and mixing in the Irminger Sea and in the Iceland Basin. *J. Geophys. Res.*, **100**(C6), 10851–71.

Krauss, W. 1996. A note on overflow eddies. *Deep Sea Res., Part I*, **43**(10), 1661–7.

Krauss, W., Fahrbach, E., Aitsam, A., Elken, J., & Koske, P. 1987. The North Atlantic Current and its associated eddy field southeast of Flemish Cap. *Deep Sea Res., Part A*, **34**(7A), 1163–85.

Large, W.G., McWilliams, J., & Doney, S. C. 1994. Oceanic vertical mixing: a review and a model with a nonlocal boundary layer parameterization. *Rev. Geophys.*, **32**(4), 363–403.

Lavender, K. L., Davis, H. E., & Owens, W. B. 2000. Mid-depth recirculation observed in the interior Labrador and Irminger seas by direct velocity measurements. *Nature*, **407**(6800), 66–9.

Lazier, J. R. N. 1994. Observations in the northwest corner of the North Atlantic Current. *J. Phys. Oceanogr.*, **24**(7), 1449–63.

Levitus, S. 1982. *Climatological Atlas of the World Oceans.* NOAA professional paper. Washington, D.C.: U.S. Govournment Printing Office.

Levitus, S., & Boyer, T.P. 1994. World Ocean Atlas 1994, Temperature. *NOAA Atlas*, **NESDIS 4**, 117pp.

Levitus, S., Burgett, R., & Boyer, T.P. 1994. World Ocean Atlas 1994, Salinity. *NOAA Atlas*, **NESDIS 3**, 99pp.

Lilly, J. M., & Rhines, P. B. 2002. Coherent eddies in the Labrador Sea observed from a mooring. *J. Phys. Oceanogr.*, **32**(2), 585–598.

Lilly, J. M., Rhines, P. B., Visbeck, M., Davis, P., Lazier, J. R. N., Schott, F., & Farmer, D. 1999. Observing deep convection in the Labrador Sea during winter 1994/95. *J. Phys. Oceanogr.*, **29**(8, pt.2), 2065–98.

Lilly, J.M., P.B., Rhines, Schott, F., K., Lavender, Lazier, J., Send, U., & d'Asaro, E. 2003. Observations of the Labrador Sea eddy field. *Prog. in Oceanogr.*, **59**(1), 75–176.

Lorbacher, K., & Koltermann, K. P. 2000. Subinertial variability of transport estimates across 48°N in the North Atlantic. *Internat. WOCE Newsletter*, **40**, 3–5.

Lozier, M. S. 1997. Evidence for large-scale eddy-driven gyres in the North Atlantic. *Science*, **277**(5324), 361–364.

Lu, Y., & Stammer, D. 2004. Vorticity balance in coarse-resolution global ocean simulations. *J. Phys. Oceanogr.*, **34**, 605–633.

Lu, Y., Ueyoshi, K., Kohl, A., Remy, E., Lorbacher, K., & Stammer, D. 2002. Input data sets for the ECCO global 1° WOCE synthesis. *ECCO Rep.*, **18**.

Macdonald, A. M., & Wunsch, C. 1996. An estimate of global ocean circulation and heat fluxes. *Nature*, **382**, 436–439.

Mann, C. R. 1967. The termination of the Gulf Stream and the beginning of the North Atlantic Current. *Deep Sea Research*, **14**, 337–359.

Marotzke, J., & Scott, J. R. 1999. Convective mixing and the thermohaline circulation. *J. Phys. Oceanogr.*, **29**(11), 2962–2970.

Marotzke, J., Cunningham, S. A., & Bryden, H.L. 2002. Monitoring the Atlantic Meridional Overturning Circulation at 26.5°N
. *http://www.nerc.ac.uk/funding/thematics/rcc/*.

Marshall, J., Adcroft, A., Hill, C., Perelman, L., & Heisey, C. 1997. A finite-volume, incompressible navier-stokes model for studies of the ocean on parallel computers. *J. Geophys. Res.*, **102**(C3), 5753–5766.

Marshall, J., Dobson, F., Moore, K., Rhines, P., Visbeck, M., d'Asaro, E., Bumke, K., Chang, S., Davis, R., Fischer, K., Garwood, R., Guest, P., Harcourt, R., Herbaut, C., Holt, T., Lazier, J., Legg, S., McWilliams, J., Pickart, R., Prater, M., Renfrew, I., Schott, F., Send, U., & Smethie, W. 1998. The Labrador Sea deep convection experiment. *Bull. Amer. Meteor. Soc.*, **79**(10), 2033–58.

Marshall, J., Johnson, H., & Goodman, J. 2001. A study of the interaction of the North Atlantic Oscillation with ocean circulation. *J. Clim.*, **14**, 1399–1421.

Mauritzen, C., & Häkkinen, S. 1999. On the relationship between dense water formation and the "Meridional Overturing Cell" in the North Atlantic Ocean. *Deep Sea Research, Part I*, **46**, 877–894.

Mehta, V. M., Suarez, M. J., Manganello, J. V., & Delworth, T. L. 2000. Oceanic influence on the North Atlantic Oscillation and associated Northern Hemisphere climate variations: 1959-1993. *Geophys. Res. Letters*, **27**(1), 121–4.

Meinen, C. S. 2001. Structure of the North Atlantic Current in stream-coordinates and the circulation in the Newfoundland Basin. *Deep Sea Res., Part I*, **48**(7), 1553–80.

Meinen, C. S., Watts, D. R., & Clarke, R. A. 2000. Absolutely referenced geostrophic velocity and transport on a section across the North Atlantic Current. *Deep Sea Res., Part I*, **47**(2), 309–22.

Morrow, R., Coleman, R., Church, J., & Chelton, D. 1994. Surface eddy momentum flux and velocity variances in the Southern Ocean from Geosat altimetry. *J. Phys. Oceanogr.*, **24**(10), 2050–71.

Müller, P., & Frankignoul, C. 1981. Direct atmospheric forcing of geostrophic eddies. *J. Phys. Oceanogr.*, **11**(3), 287–308.

Myers, R.A., Helbig, J., & Holland, D. 1989. Seasonal and interannual variability of the Labrador Current and West Greenland Current. *ICES CM*, **C:16**, 10.

Nonaka, M., & Xie, S-P. 2000. Propagation of North Pacific interdecadal subsurface temperature anomalies in an ocean GCM. *Geophys. Res. Letters*, **27**(22), 3747–3750.

Orvik, K.A., & Niiler, P. 2002. Major pathways of Atlantic water in the northern North Atlantic and Nordic Seas toward Arctic. *Geophys. Res. Letters*, **29**(19), 2–1:2–4.

Orvik, K.A., Skagseth, Ø., & Mork, M. 2001. Atlantic inflow to the Nordic Seas: current structure and volume fluxes from moored current meters, VM-ADCP and SeaSoar-CTD observations, 1995-1999. *Deep Sea Research*, **48**, 937–957.

Paillet, J., Arhan, M., & McCartney, M. S. 1998. Spreading of Labrador Sea Water in the eastern North Atlantic. *J. Geophys. Res.*, **103**(C5), 10223–39.

Pickart, R., Torres, D. J., & Clarke, R. A. 2002. Hydrography of the Labrador Sea during active convection. *J. Phys. Oceanogr.*, **32**(2), 428–457.

Pickart, R., Straneo, F., & Moore, G.W.K. 2003. Is Labrador Sea Water formed in the Irminger Basin? *Deep Sea Res.*, **50**(1), 23–52.

Pollard, R. T. 1996. Vivaldi 1991 - A study of the formation, circulation and ventillation of the Eastern North Atlantic Cental Water. *Prog. Oceanogr.*, **37**, 167–192.

Pollard, R. T., Read, J. F., & Holliday, N. P. 1999. Circulation and mode waters of the North Atlantic subpolar gyre in 1996. *Internat. WOCE Newsletter*, **37**, 21–27.

Pollard, R. T., Read, J. F., Holliday, N. P., & Leach, H. 2004. Water masses and circulation pathways through the Iceland Basin during Vivaldi 1996. *J. Geophys. Res.*, **109**(C4), doi:10.1029/2003JC002067.

Prater, M. 2002. Eddies in the Labrador Sea as observed by profiling RAFOS floats and remote sensing. *J. Phys. Oceanogr.*, **32**(2), 411–427.

Rago, T. A., & Rossby, H. T. 1987. Heat-Transport into the North-Atlantic Ocean North of 32- Degrees-N Latitude. *J. Phys. Oceanogr.*, **17**(7), 854–871.

Read, J. F., & Gould, W. J. 1992. Cooling and freshening of the subpolar North Atlantic Ocean since the 1960s. *Nature*, **360**(6399), 55–7.

Reverdin, G., Verbrugge, N., & Valdimarsson, H. 1999. Upper ocean variability between Iceland and Newfoundland, 1993-1998. *J. Geophys. Res.*, **104**(C12), 29599–611.

Reverdin, G., Niiler, P. P., & Valdimarsson, H. 2003. North Atlantic Ocean surface currents. *J. Geophys. Res.-Oceans*, **108**(C1).

Rodwell, M.J., Rowell, D.P., & Folland, C.K. 1999. Oceanic forcing of the wintertime North Atlantic Oscillation and European climate. *Nature*, **398**(6725), 320–323.

Rogers, J.C. 1984. The association between the North Atlantic Oscillation and the Southern Oscillation in the Northern Hemisphere. *Monthly Weather Review*, **112**, 1999–2015.

Rossby, H. T. 1996. The North Atlantic Current and surrounding waters: at the crossroads. *Rev. Geophys.*, **34**(4), 463–481.

Schmitz, W. J., Jr., & Holland, W. 1982. A preliminary comparison of selected numerical eddy-resolving general circulation experiments with observations. *J. Mar. Res.*, **40**, 75–117.

Schmitz, W. J., Jr., & McCartney, M. S. 1993. On the North Atlantic circulation. *Rev. Geophys.*, **31**(1), 29–49.

Schott, F., Stramma, L., & Fischer, J. 1999. Interaction of the North Atlantic Current with the deep Charlie Gibbs Fracture Zone throughflow. *Geophys. Res. Letters*, **26**(3), 369–72.

Seager, R., Battisti, D. S., Yin, J., Gordon, N., Naik, N., Clement, A. C., & Cane, M. A. 2002. Is the Gulf Stream responsible for Europe's mild winters? *Q. J. R. Meteorol. Soc.*, **128**(586), 2563–2586.

Semtner, A. 1974. A general circulation model for the World Ocean. *Department of Meteorology, University of California, Los Angeles, Technical Report*, **9**, 99pp.

Sinha, B., Topliss, B., & Harle, J. 2004. Eastward propagating surface anomalies at ocean gyre boundaries. *J. Geophys. Res.*, submitted.

Smith, W.H.F., & Sandwell, D.T. 1997. Global sea floor topography from satellite altimetry and ship depth soundings. *Science*, **277**(5334), 1956–1962.

Snaith, H. 2000. Global Altimeter Processing Scheme User Manual: v1. *Southampton Oceanography Centre Internal Document*, **53**.

Spall, M. A., & Pickart, R. S. 2001. Where does dense water sink? a subpolar gyre example. *J. Phys. Oceanogr.*, **31**(3), 810–26.

Stammer, D. 1997. Steric and wind-induced changes in TOPEX/POSEIDON large-scale sea surface topography observations. *J. Geophys. Res.*, **102**(C9), 20987–1009.

Stammer, D., & Wunsch, C. 1999. Temporal changes in eddy energy of the oceans. *Deep Sea Res., Part II*, **46**(1-2), 77–108.

Stammer, D., Tokmakian, R., Semtner, A., & Wunsch, C. 1996. How well does a 1/4 degree global circulation model simulate large-scale oceanic observations? *J. Geophys. Res.*, **101**(C11), 25779–811.

Stammer, D., Ueyoshi, K., Large, W.G., Josey, S. A., & Wunsch, C. 2001. Global sea surface flux estimates obtained through ocean data assimilation. *ECCO Rep.*, **13**.

Stammer, D., Wunsch, C., Giering, R., Eckert, C., Heimbach, P., Marotzke, J., Adcroft, A., Hill, C., & Marshall, J. 2002. Global ocean circulation during 1992-1997, estimated from ocean observations and a general circulation model. *J. Geophys. Res.*, **107**(C9), 1–27.

Straneo, F., Pickart, R., & Lavender, K. I. 2003. Spreading of Labrador sea water:an advective-diffusive study based on Lagrangian data. *Deep Sea Research*, **50**, 701–719.

Sutton, R.T., & Allen, M.R. 1997. Decadal predictability of the North Atlantic sea surface temperature and climate. *Nature*, **388**, 563–567.

Sy, A., Schauer, U., & Meincke, J. 1992. The North Atlantic Current and its associated hydrographic structure above and eastwards of the Mid-Atlantic Ridge. *Deep Sea Res., Part A*, **39**(5A), 825–53.

Taylor, A. H., & Stephens, J. A. 1998. The North Atlantic Oscillation and the latitude of the Gulf Stream. *Tellus*, 1.

Thompson, J. D., & Schmitz, W. J., Jr. 1989. A limited-area model of the Gulf Stream: design, initial experiments, and model-data intercomparison. *J. Phys. Oceanogr.*, **19**(6), 791–814.

Tourre, Y., & Kushnir, Y. 1999. Evolution of interdecadal variability in sea level pressure, sea surface temperature, and upper ocean temperature over the Pacific Ocean. *J. Phys. Oceanogr.*, **29**(7), 1528–1541.

Tracey, K. L., & Watts, D. R. 1986. On Gulf-Stream Meander Characteristics near Cape-Hatteras. *J. Geophys. Res.-Oceans*, **91**(C6), 7587–7602.

Tsujino, H., & Suginohara, N. 1999. Thermohaline Circulation Enhanced by Wind Forcing. *J. Phys. Oceanogr.*, **29**(7), 1506–1516.

Watson, A. J., Messias, M. J., Fogelqvist, E., Van Scoy, K. A., Johannessen, T., Oliver, K. I. C., Stevens, D. P., Rey, F., Tanhua, T., Olsson, K. A., Carse, F., Simonsen, K., Ledwell, J. R., Jansen, E., Cooper, D. J., Kruepke, J. A., & Guilyardi, E. 1999. Mixing and convection in the Greenland Sea from a tracer-release experiment. *Nature*, **401**(6756), 902–4.

Webb, D.J., de Cuevas, B. A., & Coward, A. C. 1998. The first main run of the OCCAM global ocean model. *Southampton Oceanography Centre Internal Document*, **34**.

White, M. A., & Heywood, K. J. 1995. Seasonal and interannual changes in the North Atlantic subpolar gyre from Geosat and TOPEX/POSEIDON altimetry. *J. Geophys. Res.*, **100**(C12), 24931–41.

Wikle, C. K. 2003. *Spatio-temporal methods in climatology.* Vol. Encyclopedia of Life Support Systems. EOLSS.

Willebrand, J., Barnier, B., Böning, C., Dieterich, C., Killworth, P. D., Le Provost, C., Jia, Y., Molines, J-M., & New, A. L. 2001. Circulation characteristics in three eddy-permitting models of the North Atlantic. *Prog. Oceanogr.*, **48**, 123–161.

Worthington, L.V. 1976. On the North Atlantic Circulation. *The Johns Hopkins Oceanogr. Stud.*, **6**, 110.

Yaremchuk, M. I., Nechaev, D. A., & Thompson, K. R. 2001. Seasonal variation of the North Atlantic Current. *J. Geophys. Res.-Oceans*, **106**(C4), 6835–6851.

Zenk, W. 2000. Labrador Sea Water in the Iceland Basin: An Overview of the Present Kiel RAFOS Float Programme. *Internat. WOCE Newsletter*, **39**, 3–6.